Alma Mater Studiorum – Università di Bologna

DOTTORATO DI RICERCA IN

Ingegneria Elettrotecnica

Ciclo XXVIII

Settore Concorsuale di afferenza:

09/E2

Settore Scientifico disciplinare:

ING-IND 33

Electrospun materials for energy applications: from Lithium-ion batteries to electrets

Presentata da
Marco Zaccaria

Coordinatore Dottorato
Prof. Domenico Casadei

Relatore
Prof. Davide Fabiani

Esame finale anno 2016

Γνωθι σεαυτόν

Index

Chapter 1
Introduction

1.1 Aim of this work

The aim of this work is focused on the application of electrospinning technology, an innovative manufacturing technique to design nanostructured polymers, for energy storage, energy harvesting and sensor applications. These nanostructures are suitable to increase specific performances of components: from the reduction of internal resistance of Lithium-ion batteries to the increase of specific electrical response of materials for energy harvesting. The increase of specific power of Lithium-ion batteries represents one of the key factors for the development of competitive storage systems for automotive and power grid. Indeed, electrochemical performances at high currents significantly decay, strongly limiting the competitiveness on the market beyond portable applications. Furthermore, recovery of dissipated energy will be one of the most promising challenges for the establishment of green technologies and for the reduction in power consumption. Finally, health monitoring and/or impact sensors could represent suitable technologies for the growth of smart materials.

Therefore, experimental campaign has been focused on the manufacturing and characterization of electrospun Lithium-ion battery separators for power-intensive applications, passing

through the development of a novel technique to disperse nanoadditives inside nanofibers, to a novel technique to increase electrolyte uptake. Moreover, the realization and characterization of electrospun electrets for energy scavenging has been carried out, focusing on the study of charge accumulation in fluoropolymers and the related triboelectric phenomena.

1.2 Perspectives and growth of energy storage and energy harvesting technologies

Energy Storage refers to the conversion of electrical energy into a form that can be stored and converted back to electrical energy when needed. The intrinsic variable and intermittent nature of renewable energy sources may affect negatively power system stability and regulation, causing unacceptable power fluctuations. In this framework, energy storage can represent a suitable option for power smoothing and voltage regulation in transmission grids as well as in distributed generation and smart grids [1].

Several energy storage technologies can be considered. Most of them are compared in Figure 1.1 in terms of energy and power and will be briefly described in the following [1]. Batteries can store energy through electrochemical reactions that lead to the formation of ions. When the battery is charged, a direct current is converted in chemical energy and when is discharged, the chemical energy is converted back into a flow of electrons. However, their relatively low durability for long-term cycling and high cost still limit their size scale-up.

Supercapacitors can give higher power and energy densities if compared with a traditional capacitor. They are characterized by extremely long cycle-life and by very short charge/discharge time. On the other hand, this technology shows much lower energy density than batteries.

Superconducting magnetic energy storage (SMES) is a technology through which it is possible to store energy in the magnetic field created by a direct current flowing in a superconducting coil when cryogenically cooled. Power can be available immediately and a high power output can be provided for a short period of time. Their high cost strongly limits any commercial application.

Another promising technology is represented by fuel cells. However, the storage of hydrogen represents a technical and economic challenge, due to its low density. Nevertheless, water electrolysis and the consequent hydrogen exploitation through fuel cells is an attractive alternative for energy storage and conversion.

Thermal energy storage uses materials that can be kept at high or low temperatures in insulated containments. Heat/cold recovered can then be applied for electricity generation using thermodynamic cycles.

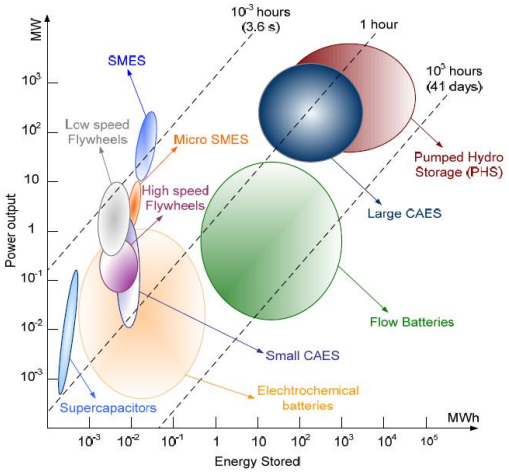

Figure 1.1 Energy and power performances of different storage techniques [1].

Nowadays, electric vehicles (EV) are considered as a key technology for sustainable transport. Full electric vehicles are

entering the market and have several advantages if compared with conventional vehicles, such as noise-free engines and zero emissions. However, typical specific energy of commercial battery packs are still insufficient to be competitive with driving distances guaranteed by conventional fuel vehicles, as highlighted in Figure 1.2. Moreover, pack weight and battery cost represent other strong issues. For these reasons, hybrid electric vehicles (HEV), which provide electric propulsion over an adequate distance, are currently more interesting for improving vehicle efficiency and performance than conventional vehicles, e.g. minimizing fuel consumption. HEV technology requires power-intensive discharge regime of the battery that can be improved by batteries having low internal resistance, having low-loss components at high currents. Even for energy-intensive applications, such as in batteries for EVs, high performance at high currents can guarantee high efficiency and less recharge time for plug-in vehicles, that can be charged on the grid. It is thus evident the importance of the new components development for energy storage devices.

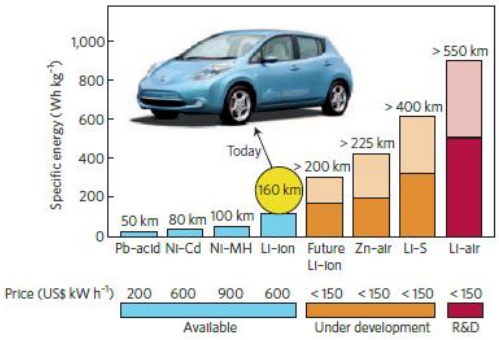

Figure 1.2 Practical specific energies for some rechargeable batteries, along with estimated driving distances and pack prices [2].

Furthermore, relatively frequent replacement of batteries represents a cost, e.g. for sensors located in inaccessible parts or at the end of battery life, but also introduces issues to the environment safety. In addition, batteries often limit the

miniaturization of micro or nano electromechanical systems, particularly nowadays when the size and power consumption of electronic devices have dramatically decreased [3]. Besides wasted energy recovery, these are some of the reasons behind the research on ambient energy harvesting to direct sustain low power consumption devices and sensors. Nevertheless, new type of energy harvesters are needed to achieve a performance breakthrough in this field, such as in terms of output power increase and shape versatility. This concept has been stressed during the second part of this work, through the study of novel electrospun electrets.

Chapter 2
Electrospinning

2.1 Premise

The first evidence of the electrospinning process dates back to 1934, thanks to a patent by Formhals, wherein an experimental setup was designed for the production of polymer filaments using electrostatic force. Therefore, the term electrospinning refers precisely to a process that produces fibers through an electrically charged jet of polymer solution or polymer melt [4].

Conventional fibers can be realized for instance, through the drawing of molten polymers. The stretched polymer dries to form an individual element, called fiber. In the same way, electrospinning comprises the drawing of a fluid, either in the form of molten polymer or polymer solution, but with different working principle. In particular, conventional technique applies an external mechanical force to the molten polymer, while electrospinning charges the polymeric fluid to provide a stretching force. This force attracts the polymeric solution to a grounded collector, due to the presence of a high voltage bias between the polymer and the collector. When an adequate high voltage is applied to a polymer solution drop, a jet will be formed. The polymer chain entanglements will prevent the electrospinning jet from breaking up, avoiding the so-called electrospraying [5], [6].

Electrospinning of melts provides cooling and solidification of the polymer into a yield fiber in the atmosphere; electrospinning of polymeric solutions is based on the evaporation of the solvent, in order to obtain a solid polymer fiber.

In general, the versatility of electrospinning permits the production of different polymers, blends, fibers containing precursors, suitable for different applications. A large number of materials can be directly produced by electrospinning, i.e. polymers and polymer composites, while other materials such as ceramics require post processing of the electrospun fibers.

Electrospinning is therefore a quite simple process to manufacture nanofibers, thanks to the requirement of common laboratory equipment. However, the science behind this technique is very complex. Indeed, electrospinning process involves the understanding of electrostatics, rheology and chemistry. These fundamental properties are constantly interacting and influencing each other during the process.

2.2 Working principles

Through the electrospinning technique, continuous polymeric or inorganic fibers, with dimensions which may range from tens of nanometers to a few microns, can be obtained by a jet of an electrostatically charged molten polymer or a polymeric solution. The process takes place thanks to a needle through which the polymer solution flows, connected to a high voltage DC generator (in the kV range) and a collecting grounded electrode, as shown in Figure 2.1.

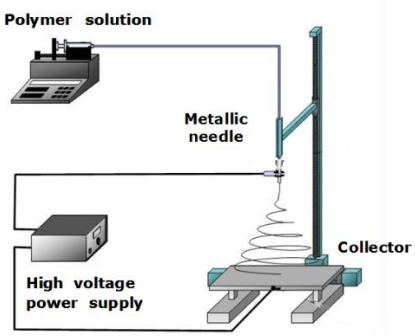

Figure 2.1 Electrospinning apparatus.

The polymeric solution, electrostatically charged by means of the high voltage power supply, comes out from the needle tip in the form of a hanging drop. The high electric field between the needle and a grounded electrode causes a distortion of the drop, until it takes a conical shape, called Taylor cone. When the electrostatic force acting on the charged drop exceeds solution surface tension, which occurs for a critical value of electric potential, a thin jet of fluid polymer is formed and attracted towards the metal collector. The charged jet is then stretched and accelerated by the electric field, undergoing to a process of instability, called *whipping instability*. The fibers run through a spiral path, which increases the stretching process, thus causing thinning of the fiber while the solvent evaporates, as summarized in Figure 2.2. This process of instability permits the formation of fibers with diameters in the order of a few hundred nanometers, favoring the evaporation of the solvent and the solidification of the fibers themselves. The chaotic movement of the jet produces the random deposition of the fibers on the collector, in the form of non-woven mat.

Figure 2.2 Taylor cone, linear path of polymeric jet and whipping instability during electrospinning [7].

Some important features of the technique should be pointed out:

- The choice of a suitable and good solvent for the polymer of interest plays a key role in process quality. Indeed, solvent must have a vapor pressure that allows the fiber to harden before it goes down to the nanometer range. The viscosity and surface tension of the solvent must avoid any free drain of polymer solution drops from the needle.
- The power supply must overcome both viscosity and surface tension to allow the jet from the needle to be formed and sustained during the process.
- The path between the needle tip and the grounded collector should not be too small to ensure complete solvent evaporation and to avoid any short-circuit between electrodes, but also not too large to ensure a stable voltage bias.

2.2.1 Cross-electrospinning

Beyond the typical electrospinning setup, the cross-electrospinning refers to a multi spinneret system fed by different polymeric solutions, in order to produce a fibrous mat composed by different polymers [8]. This process, summarized

in Figure 2.3, differs from the electrospinning of polymer blends, which deals with different polymers dissolved in the same solvent system.

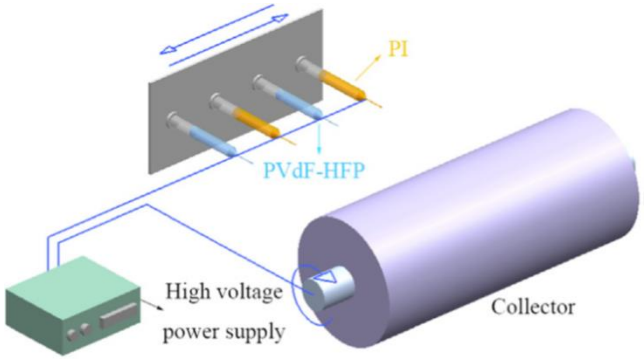

Figure 2.3 Schematic of a cross-electrospinning apparatus [8].

This peculiar technique will be further implemented for a specific application of a novel electrospun separator for lithium-ion batteries.

2.2.2 Mass production of electrospun fibers

Multiple spinnerets can easily enlarge the deposition rate of electrospun fibers, thus increasing the production rate of the process. However, possible clogging issue of the needles and setup optimization needs have raised the development of a parallel technique, which is needleless electrospinning [9], [10]. Industrial scale-up of electrospinning is commonly implemented through needless solutions and an example of this technology is reported in Figure 2.4.

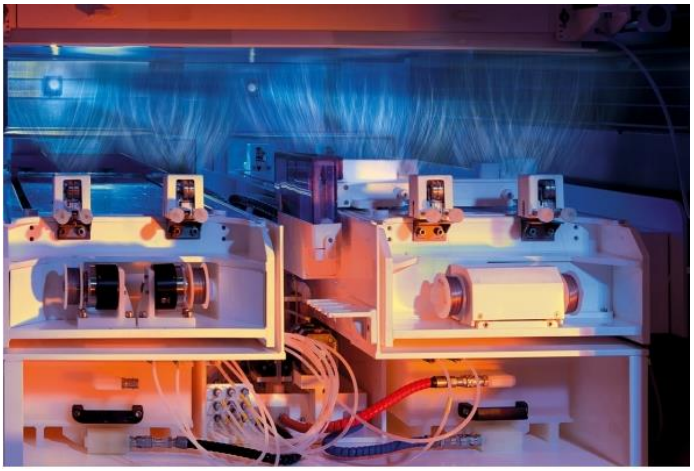

Figure 2.4 Mass production electrospinning equipment [www.elmarco.com].

2.3 Solution and process parameters

In this section, the most important parameters, both related to the polymeric solution and to the electrospinning process, will be described.

Surface tension: the charging process of the polymeric solution has to overcome the surface tension. Moreover, while the solution is being stretched during the process, a low surface tension of the solution may cause a jet breakup into droplets [11], [12], leading to a different process, called electrospraying. Under these circumstances, indeed, the shrinkage of solution surface causes surface area reduction and thus the formation of spherical shape droplets, that is the configuration of lowest energy.

Polymer solubility: Different solvents have different electrospinnability, due to their conductivity and their tendency to be polarized [13]. For this reason, high dielectric constant solvents should be used. Polymer solubility in each solvent also affect fiber morphology of the resultant mat [14].

Viscosity: Solution viscosity has a strong effect on the process and consequently on fiber morphology. The viscosity is directly linked to the amount of entanglements formed by polymer chains in the solution. If the viscosity is too low, electrospraying may occur and polymer particles are formed instead of fibers. At low viscosity values, beads are commonly observed along the fibers axis [15] instead of smooth fibers. This behavior is explained by the dominant role of surface tension, due to the higher amount of solvent molecules compared to polymer chain entanglements. A change in the shape of the beads, from spherical to spindle-like, occurs increasing solution viscosity, until a smooth fiber is formed [15], [16]. Charges are able to fully stretch the solution. Too high viscosity determines problems to pump the solution through the needle [17] or solution drying creates troubles on the needle tip. Finally, the higher the solution viscosity, the thicker the fiber diameter [13], [18]–[20]. This behavior is probably due to the resistance of the solution to be stretched by the charges [13].

Polymer molecular weight: Fiber formation occurs only if the molecular weight of the polymer is sufficiently high to give enough viscosity to the solution. This property represents the length of the polymer chains, which determine the amount of entanglements.

Solvent evaporation rate: Most of the solvent evaporates during the path towards the collector, leading to solid fiber formation. However, the rate of evaporation of the solvent could not be sufficient, resulting in fibers not formed at all or still wet. Needle-to-collector distance increase can partially solve this state.

Solution conductivity: Polymeric solution must gain enough charges to increase the repulsive forces inside the solution, thus overcoming the surface tension of the solution. Subsequent stretching of the jet is connected to the ability of the solution to

carry charges. The electric conductivity of solvents is commonly very low (typically between 10^{-3} to 10^{-9} S/m), due to the presence of very few free ions. A strategy to increase the electrical conductivity of the solution is the addition of a small quantity of a polar non-solvent of the polymer or proper salts. However, the interaction between solvent mixtures can affect polymer solubility, modifying fiber morphology [14].

Voltage bias: Voltage provides the stretching of the solution, thanks to the columbic force in the jet and the high electric field. In general, voltage increase reduces fiber diameter [19], [21], [22] and favors solvent evaporation [23]. Voltage bias also defines the flight time of the jet, governing the stretching force and consequently fiber diameter. Thinner fiber diameters have been observed increasing voltage bias [13]. Polymer morphology is affected by electrospinning, leading in general to higher crystallinity degree. In particular, crystallinity can be increased applying higher voltage bias, ensuring enough flight time to the jet [24].

Flow rate: This parameter controls the amount of solution available for the process and permits to obtain a stable Taylor cone, for a given voltage bias. The higher the flow rate, the larger the fiber diameter or the size of beads, due to a bigger volume of solution spun [25].

Grounded collector: Patterned collectors can be suitable to produce different fiber patterns; aligned fibers can be obtained, for instance, through a high-speed rotating collector that provides a further mechanical stretching force on the fibers. Since polymers are generally non-conductive, residual charge accumulation on the electrospun mat can occur at high deposition rate.

Needle diameter: the decrease of the inner diameter of the spinneret causes a reduction in fiber diameter; a drop of solution cannot flow through too small needles [26].

Needle-to-collector distance: The resultant fibers are affected both by the electric field strength and flight time, which vary with needle-to-collector distance. The latter parameter determines solvent evaporation rate. Possible spinning instability can occur when the distance is too low [25], [27].

Ambient temperature and humidity: temperature and humidity affects solvent evaporation rate and possible clogging problems on the needle can occur [18].

2.4 Main properties of electrospun materials

Versatility of electrospinning allows a wide variety of polymers to be spun, keeping the same experimental apparatus. Moreover, among fiber fabrication techniques, i.e. phase separation, drawing and template synthesis, electrospinning exhibits the ability to manufacture fibers in the submicron range, challenging feature otherwise achievable through conventional techniques [28].

Electrospun fibrous mats also offer peculiar features [29], [30], such as:

1. large porosity (meant as pore volume/mat volume)
2. small pores, below few microns
3. pore interconnectivity, which gives three-dimensional structure
4. high surface area
5. extremely high surface-to-volume ratio

Finally, lightness, flexibility and possibility of realizing tunable sizes and shapes represent other interesting properties of such fibrous materials. Nanofiber composition can be also designed to obtain peculiar properties and functionalities [31].

2.5 Main application fields of electrospun materials

One of the most fascinating feature of electrospinning is the extremely wide range of applications [29]. Indeed, the aforementioned peculiar properties of fibrous structures make electrospun mats suitable for several fields, even in very different areas.

The most important fields can be summarized as follows:

- Air and water filtration [29]
- Bio-medical, tissue engineering and drug delivery [29], [32]–[35]
- Composite reinforcement [29]
- Sensors and actuators [36]
- Energy storage and energy harvesting [36], [37]

For the purpose of this thesis, only the last two application fields will be further discussed.

Sensors and actuators: these devices are commonly based on piezoelectric materials and for instance can be implemented for the realization of impact sensors or smart filters.

Energy storage: energy storage typically refers to thermal energy, chemical energy, e.g. batteries, fuel cells and supercapacitors, or electrical energy, e.g. Superconducting Magnetic Energy Storage (SMES) systems, kinetic energy that can be converted and/or accumulated. These devices might play a key role both in the field of electric vehicles and in stationary applications, aiming at developing new solutions for improving power generation efficiency.

Energy harvesting: this quite novel and emerging topic is related to the possibility to recover small quantity of energy from sources that usually dissipate thermal or mechanical

energy, e.g. through vibrations. This harvested energy can directly sustain low-power electronic devices or can be stored.

Chapter 3
Lithium-ion batteries

3.1 Premise

So-called conventional battery technologies using water-based electrolytes provide open circuit voltages up to 2 V. On the other hand, Lithium metal used as negative electrode coupled with a non-aqueous electrolyte leads to much larger voltages, up to 4 V. Indeed, Lithium has the lightest weight, highest voltage, and greatest energy density among all metals [38]. For these reasons, Lithium probably represents the most attractive system for electrochemical purposes.

After a patent of 1949, the first remarkable papers on Lithium cells arose in the '60s and the first commercialized primary cells during the 1970s. Research on secondary Lithium batteries increased during the 1980s, due to the use of intercalation materials as positive electrode [39], [40]. This kind of material has the ability to reversibly store Lithium ions inside its structure. Typically, these materials are transition metals oxides. However, safety problems of secondary Lithium batteries have reduced the progress of this technology. Indeed, the use of Lithium metal coupled with an organic liquid electrolyte can lead to short-circuits, due to the dendritic growth of Lithium during cycling [41], [42]. Two technology solutions were developed to overcome safety issues:

1. Using a solid polymer electrolyte, less reactive in contact with Lithium and more resistant to dendritic puncture; this approach has led to the all-solid-state lithium metal rechargeable batteries [43] (not yet commercialized due to low ionic conductivity at room temperature)
2. Replacing Lithium anode with a material able to reversibly intercalate Lithium ions, leading to the so-called Lithium-ion batteries [39]

The latter cells, based on the principle of ions moving between two intercalation materials, represent the commercial solution of modern Lithium batteries. This working principle has given the name of "rocking-chair" to this technology [44].

Commercial Lithium-ion batteries have reached the market only in 1991, thanks to Sony, due to the breakthrough in negative electrode materials, i.e. carbonaceous intercalation materials for Lithium ions [44].

3.2 Working principles of Lithium-ion batteries

Lithium theoretically displays an extremely high specific capacity (3860 mAh/g) and the lowest negative electrochemical potential (-3.040 V) with respect to the standard hydrogen electrode. The typical Lithium-ion battery (LIB) is composed by:

- a graphite anode with a layered structure in which Lithium ions can intercalate, thus preventing dendritic growth
- a Lithium metal oxide cathode, in the typical $LiMO_2$ form with M a generic metal, e.g. $LiCoO_2$
- a polymeric separator
- a liquid electrolyte composed of a Lithium salt typically dissolved in a mixture of organic solvents

The aforementioned cell architecture is reported in Figure 3.1.

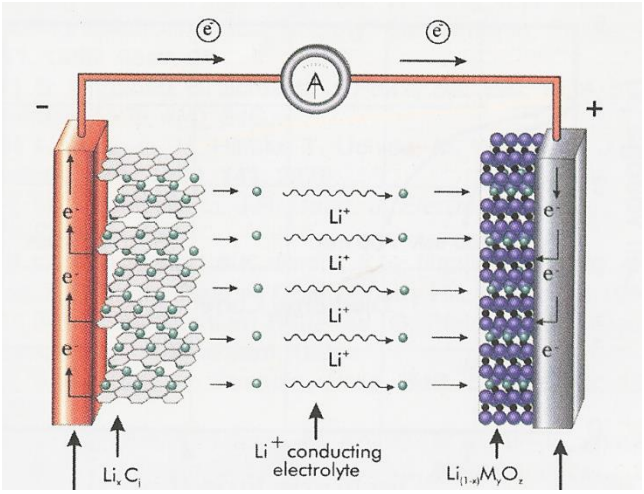

Figure 3.1 LIB scheme [45].

The working principle of a LIB cell is described below. For the sake of example, a graphite anode and a $LiCoO_2$ cathode are here considered, thus giving the reaction 3.1:

$$6C + LiCoO_2 \leftrightarrow Li_xC_6 + Li_{1-x}CoO_2 \quad (3.1)$$

Using $LiCoO_2$, reaction reversibility is obtained only with a value of x greater than 0.5, thus keeping the degree of Lithium insertion no lower than 0.5. If more than half of the Lithium is extracted from the cathode, a permanent structural modification occurs, blocking ion intercalation in the material. Indeed, the inter-layer distance in lamellar structure becomes too small and this behavior is followed by oxygen release, which can react with the electrolytic organic solvents with important risks of fire and explosion. Thus, the charge voltage in a $Li_{(1-x)}CoO_2$ cell has to be limited to 4.2 V in order to keep the threshold value of 0.5 [46].

On the other hand, theoretically the Li^+ intercalation process into graphite is fully reversible. However, during the first cycle, part of the charge is consumed and the following deintercalation

of Li^+ does not recover the full charge, but only about 80-95%. In further cycles, charge consumption due to Li^+ intercalation is much lower and charge recovery is close to 100%. The charge consumed in the first cycle is due to solid electrolyte interphase (SEI) formation and to reactions like Li_xC_6. The intercalation compounds are thermodynamically unstable in organic electrolytes. Therefore, passivation films like SEI protect their surfaces, which exposed to the electrolyte. This charge loss is irreversible and leads to a cell capacity reduction [39].

The cycleability of Lithium-ion systems mainly depends on the dimensional stability of the intercalation materials during insertion/de-insertion of Li^+ ion. Indeed, mechanical stress occurring during charge/discharge cycles can crack the electrodes, leading to contact losses between active material and possible oxidation/reduction phenomena on current collectors [39].

3.3 Materials

Before a detailed description of each battery component, it is important to highlight that both anodes and cathodes are composite electrodes. Carbon anodes are composed of the active material (about 90%) and a polymeric binder such as polyvinylidene fluoride (PVdF) (less than 10%). The cathodes are composed of the active material (about 85%), a polymeric binder (less than 10%) and a small quantity of a conductive carbonaceous additive. A proper solvent is used to mix the so-called slurry of these materials, which is then spread out on a suitable current collector [38].

Figure 3.2 shows the state of the art of LIB electrode materials and their future prospect [47]. It is worth noting that a huge breakthroug is still achievable in terms of electrode specific capacity and potential window. However, the setup of a proper electrolyte that can be electrochemical stable up to 5 V is required.

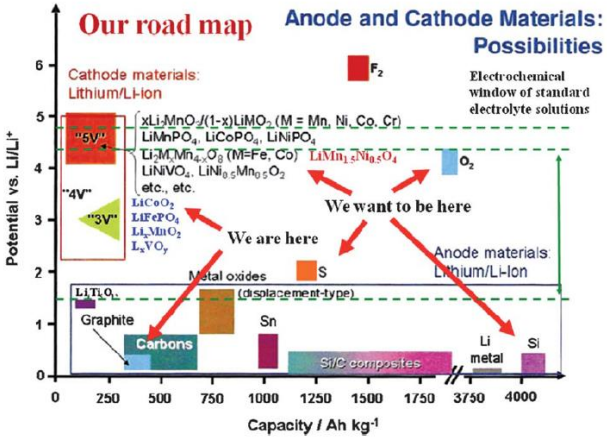

Figure 3.2 State of the art of LIB electrode materials and future prospect [47].

Anode: graphite is the most studied and implemented material. Its theoretical specific capacity is 372 mAh/g, much lower than Lithium metal, but graphite is much more stable for safety issue and its potential is lower than that of Lithium only of about 100 mV. Li^+ ions intercalate between graphene plates, slightly deforming the layer structure. Volume changes during cycles are about 10-15 % [38].

For Li-alloy anodes, the volume difference between the Lithium alloy and the corresponding Lithium-free matrix metal is typically about 100%. After few cycles, the alloy becomes fragile, strongly limiting cycle life. An exception is represented by $Li_4Ti_5O_{12}$ (LTO), which displays very small volume changes during cycles. Moreover, Lithium insertion potential is about 1.55 V (vs. Li/Li^+) and this feature prevents Li plating on the anode surface (leading to dendritic growth), even at high currents. Finally, LTO displays very fast charge acceptance and excellent cycle performances. However, it is an expensive material and displays low voltage when coupled with cathodes such as $LiMO_2$, i.e. 2.5 V, strongly limiting the energy density of the cell [48].

Cathode: Lithiated transition metal oxides, having a lamellar structure, $Li_{(1-x)}MO_2$ (where M is one or more metals such as Co, Ni, etc.) or $Li_{(1-x)}Mn_2O_4$ or lithiated iron phosphates $Li_{(1-x)}FePO_4$ are commonly used as positive materials. Lithium ions can be inserted/de-inserted in the host structure over a wide range of potentials (3-5 V) [46]. The latter compounds show lower specific capacity but lower cost compared to $LiCoO_2$ (LCO), as can be observed in Table 3.1. Furthermore, LCO still represents the most common cathode material, even if its market has progressively decreased due to cost, availability and toxicity issues. Thus, the use of lithium-Nickel-Manganese-Cobalt-oxide compounds (NMC), e.g. $LiNi_{1/3}Mn_{1/3}Co_{1/3}O_2$, has dramatically increased [46], [48], recently.

Table 3.1 Gravimetric capacity of common cathode materials [48].

Materials	**Theoretical gravimetric capacity [mAh/g]**	**Theoretical gravimetric capacity [mAh/g] taking into account the degree of insertion**	**Average pratical gravimetric capacity [mAh/g]**	**Cost**
$LiCoO_2$	274	137	120	High
$LiNiO_2$	275	275	220	Medium
$LiMn_2O_4$	148	148	120	Low
$LiCo_{0.2}Ni_{0.8}O_2$	274	247	180	Medium
$LiFePO_4$	170	170	150	Low

Current collector: the role of current collectors (usually about 10 μm thick) is to conduct electrons from the active materials to the electrode terminals and then to the external circuit. Aluminum foil is typically used for the cathode, while copper foil for the anode [48].

Electrolyte: conventional aqueous electrolytes cannot be used in contact with Lithium, due to spontaneous oxidation

reactions, that lead to hydrogen production. For this reason, aprotic organic solvents are commonly used to dissolve a Lithium salt, which is typically $LiPF_6$. This salt provides a high ionic conductivity, even if it is affected by thermal stability problems and by susceptibility to hydrolysis, with the consequent formation of hydrofluoric acid [49]. The electrolyte present in commercial batteries is typically a molar solution of $LiPF_6$ in ethylene carbonate (EC) and dimethyl carbonate (DMC), which are highly stable in contact with graphite [46]. Additives are typically included into the electrolyte solution to improve stability and electrochemical performances of the LIB. Moreover, flame-resistant or flame-retardant are used too, even if research on non-flammable electrolytes is currently under investigation due to safety issues [48].

Separator: this component is the only inactive material inside the cell, but it carries out two essential functions:

- Prevention of short-circuit between electrodes
- Ionic conduction throughout its porous structure

Separators are thus manufactured as porous membranes or multi-layered porous membranes. Usually, these membranes are constituted microporous films of polyethylene (PE) or polypropylene (PP) or a combination of these. A PE separator is typically preferred for safety reason and is called “shutdown” separator. Indeed, PE has a low melting point and in case of temperature increase, the separator begins to close its pores, at about 110°C. Indeed, polymer begins to melt, increasing significantly the electrical resistance and acting as a “fuse”. The cell can no longer deliver or receive any current. The PP, which has a higher melting temperature, can be used to ensure the physical separation between the electrodes, realizing a so-called tri-layer structure that greatly improves battery safety [46]. A typical scanning electron microscope (SEM) image of a commercial separator is reported in Figure 3.3.

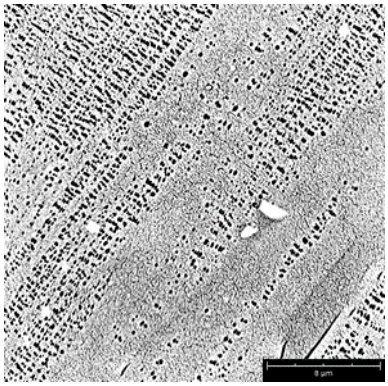

Figure 3.3 SEM image of a commercial Celgard 2400.

Moreover, separator must be an excellent electrical insulator and being a good ionic conductor at the same time. Its presence inside the battery introduces a resistance, which contributes to the internal cell resistance. The MacMullin number (N_M) is the typical parameter that takes into account separator contribution to the internal resistance, assuming equivalent dimensions between the electrodes. N_M is calculated as follows:

$$N_M = \frac{R_s}{R_0} \quad (3.2)$$

where R_s is the resistance of the separator sandwiched between the electrodes and soaked in electrolyte and R_0 is the resistance of the liquid electrolyte. This number should tend to one, but commercial separators have N_M between 5 and 15 [49].

A brief review of the most important properties of the separator will be discussed in the following sections, according to Zhang et al. [50].

Chemical stability: the separator has to be chemically stable in contact with the electrolyte, due to the presence of strongly reductive and oxidative environments at each electrode. At the same time, it should not degrade and lose its mechanical integrity.

Thickness: low thickness is desired in order to obtain high energy and power densities from the battery. However, mechanical stability and safety could be compromised. Moreover, a uniform thickness is necessary to ensure long cycle life: 25μm thick separators are currently implemented for consumer rechargeable batteries.

Porosity: a certain degree of porosity is necessary to ensure good ionic conductivity, holding a sufficient amount of electrolyte. Nevertheless, too high porosity will threaten the shutdown performance, due to problems of pore closing and membrane tendency to shrink, during melting or softening of the separator. Typically, LIB separators have a porosity of about 40%.

Pore size: pore size must be small enough to ensure that active and inactive particles that compose the electrodes do not pass through the separator. Sub-micrometric pore sizes can block particle penetration. A uniform distribution and a tortuous structure of the pores ensure a uniform current distribution, thus avoiding any dendritic growth of Lithium.

Wettability: the separator has to be easily soaked in the electrolyte and retain the permanently the liquid. A standard test for wettability measurements is still lacking.

Mechanical strength: battery assembly operations impose strong mechanical behavior of the separator, in order to sustain manufacturing process.

Dimensional stability: Separator dimensions must be stable in order to prevent short-circuit in any operating condition.

Thermal shrinkage: polymeric separators tend to shrink when the temperature inside the cell reaches the softening temperature, due to the density difference between the

crystalline and the amorphous phase. For this reason, thermal shrinkage must be minimized and is required to be lower than 5% after 60 min at 90°C.

Shutdown: before the beginning of thermal runaway, the separator must be able to shutdown, keeping its mechanical integrity. If not, chemical reactions cause thermal runaway after electrode short-circuit. A change in the resistance of the separator soaked in electrolyte, with temperature increase, can provide the shutdown characteristics. The typical LIB shutdown temperature is about 130°C, below that the separator must close its pores to inhibit ionic conduction.

Cost: the cost of the separator is about 20% of the total cost of a LIB, due to its manufacturing process. Nevertheless, cost has always to be compared to the desired performance and safety.

Finally, besides the aforementioned polyolefin, PVdF and its co-polymers have been deeply studied as LIB separator and are still the most interesting materials, due to good chemical resistance, high mechanical strength and excellent thermal stability [51], [52]. This work is thus focused on the performance study of electrospun PVdF-based separators.

3.3.1 Elecrospun separators

As previously mentioned, polyolefin microporous separators have been widely used for commercial LIBs. However, these materials exhibit some disadvantages, such as low porosity (about 40%), poor wettability and high cost [53], [54]. Moreover, polyolefin significantly contribute to internal resistance of the cell, as can for instance be observed by a high MacMullin number measured for a commercial Celgard 2400 [55]. On the contrary, nonwoven separators display huge porosity (60–90%) and wettability, high pore interconnectivity and high surface

area to volume ratio. These properties lead to a large electrolyte uptake and excellent Li^+ transport, which would increase the rate capability of the lithium ion battery [56]–[59]. Furthermore, nonwoven mats have been considered as an alternative separator also due to their relatively low cost [60], [61]. A typical SEM image of an electrospun separator is reported in Figure 3.4.

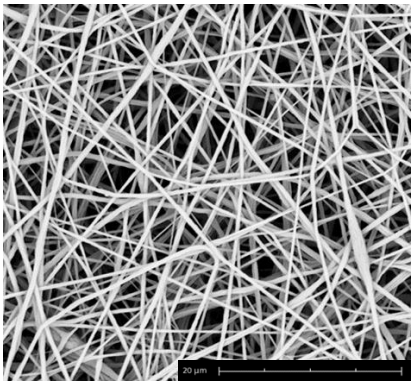

Figure 3.4 SEM image of a PVdF electrospun separator.

However, electrospun mats have some disadvantages, such as quite poor mechanical properties [62], [63]. The latter consideration is one of the key aspect for further development of these materials on the market. However, this issue is generally ignored in most of the published articles related to the application of electrospun separators for LIBs. Indeed, the possibility to scale-up the electrospinning technique is subjected to the mechanical resistance of electrospun mats during battery assembly operations, that require specific tensile strength [64]. A deep investigation of the mechanical property modification of electrospun separators will be reported in the experimental section.

3.3.2 Nanofilled separators

A quite novel topic not fully investigated in literature yet is the improvement of electrospun separator properties through

the dispersion of nanometric fillers inside nanofibers or between the fiber layers, through the combination of electrospinning and electrospray techniques. These works report the modification of mechanical properties [65]–[68] or the increase of electrolyte uptake, dimensional stability at high temperature, ionic conductivity and electrochemical stability [66], [69]–[74] of electrospun separators. Typical suitable additives are metal oxides, ceramics or particles containing Lithium.

Since these topics are very important for the development of high performance nanostructured separators for LIBs, an extensive part of the experimental section will be dedicated to the effect of additives on the performance of electrospun separators. Moreover, the possibility to improve some properties of the separator, e.g. mechanical properties, will be discussed taking into account that the use of nanoadditives can involve remarkable safety issues. For this reason, the aforementioned cross-electrospinning technique will be also presented to produce more eco-friendly separators with good mechanical properties.

3.3.3 Novel plasma assisted nanoparticle dispersion

An atmospheric pressure non-thermal plasma has been used for the first time to disperse nanoparticles inside the electrospun polymeric fibers, in order to modify separator properties [75]. In particular, fumed silica nanoparticles have been dispersed in poly(ethylene oxide) (PEO) nanofibers through different plasma treatments and nanoparticle dispersion has been evaluated. This study has led to a patent pending PCT application [76].

The term *plasma* generally refers to an ionized gas composed of electrically charged particles [77]. This state of matter can be obtained providing temperature to the gas, resulting in the

dissociation of molecular bonds and ionization of the medium. Therefore, charged particles can interact between each other in the plasma in a collective manner. Both thermal and non-thermal plasmas exist and a temperature below 100 eV conventionally defines a non-thermal plasma [77]. A non-thermal plasma is usually a plasma discharge that is not in thermodynamic equilibrium, due to the different temperature of ions and electrons [77]. An atmospheric pressure non-thermal plasma [78] is a highly reactive multi-component system that is composed of:

- Charged particles (electrons, negative and positive ions)
- Excited atoms and molecules
- Active atoms and radicals
- UV-photons

3.3.4 Plasma treatment of electrospun separators

Another interesting topic is the possibility to use the combination of a plasma treatment of the polymeric solution before the electrospinning process and a plasma treatment of the electrospun separator after manufacturing process. The positive effect of plasma pre-treatment of the solution permits to produce defect-free fibers, thus improving fiber morphology, as previously described by Shi et al. and Colombo et al. [79], [80]. Furthermore, plasma post-treatment induces a chemical modification of separator surface. The combination of these two treatments permits a dramatic increase in electrolyte uptake of electrospun mats, as will be shown in Chapter 5. This achievement is directly related to the ionic conductivity of an electrochemical cell and leads to high performance batteries for power applications.

Chapter 4
Electrets, piezoelectrics and triboelectric effect

4.1 Premise

In 1732, Gray described electret properties of a wide number of dielectrics, such as particular waxes, rosins, and Sulphur. In 1919, Eguchi realized an electret applying an electrical field to a cooling melt of the aforementioned dielectrics. More recently, long-lived electrets have increased attention after the description of the first microphone based on a polymeric electret in 1962. This application is still the most developed one for this type of materials [81].

Jaques and Pierre Curie discovered piezoelectricity in 1880 observing the behavior of a single crystal of quartz. Rochelle salt, tourmaline, and topaz are other natural materials exhibiting piezoelectric behavior. An increase of interest in research on this field was achieved during 1950s after the discovery of ferroelectric ceramics barium titanate and, particularly, lead zirconate titanate (PZT), which is one of the most sensitive piezoelectric materials. This latter material, indeed, allowed the realization of several sensors, transducers and actuators. After the discovery of PVdF in 1969, polymers showing piezoelectric characteristics have been widely studied and implemented in commercial devices. They show, in fact,

some advantages compared to ceramics such as flexibility and less brittle nature, properties that can be suitable in many different applications, even if the piezoelectric response of polymers is lower than that of ceramics [82].

4.2 Electrets

An electret is a dielectric that displays a quasi-permanent electrical charge and this charge decays after long periods. The electret charge consists of real charges, such as surface-charge or space charges trapped in the dielectric material. Electrets are commonly realized applying an electric field to a cooling melt [81] or by means of a dielectric barrier discharge (DBD) applied to the voids of a dielectric (e.g. cellular foams, fluorinated polymers, etc.) [83].

A typical model of an electret is reported in Figure 4.1.

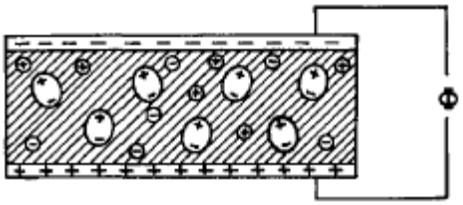

Figure 4.1 Model of an electret with space charge trapped and dipoles oriented by the voltage bias applied [81].

Piezoelectric polymers can be considered both morphologically and electrically related to conventional polymer electrets. Therefore, piezoelectrics can also be mentioned as electrets [81]. This concept will be very important throughout the discussion about the electrical response of an electrospun mat when subjected to a mechanical stress. Indeed, in the same electrospun electroactive polymer the overlapping of several charging and dipolar phenomena exists.

4.3 Piezoelectricity

Piezoelectric materials have the intrinsic property of being able to transduce mechanical energy into electrical energy. This behavior makes them useful as sensors of different mechanical stimuli, such as pressure, strain, vibration and sound. Furthermore, they can also convert electrical energy into mechanical energy, working as actuators.

All dielectric materials, if subjected to an electric field, change their dimensions. Indeed, this modification is caused by the displacements of positive and negative charges in the crystal lattice. Cations move in the direction of the electric field, while anions in the opposite direction, determining a deformation of the material. The amount of the deformation depends on the presence of a symmetric centre in the crystal. Indeed, when an external electric field is applied to a dielectric having a centre of symmetry the movements of cations and anions are cancelled by the presence of the chemical bonds. In this case, no deformation is observed. However, a small net deformation of the lattice can be observed due to the non-harmonic behavior of the bonds. This deformation is independent of the direction of the applied field and this effect is called electrostrictive effect. In order to observe piezoelectric behavior it is necessary that the dielectric material does not have a centre of symmetry, thus allowing a non-symmetrical moment of anions and cations. This deformation is directly proportional to the applied electric field and it is called indirect piezoelectric effect. The so-called direct piezoelectric effect is obtained when an external deformation is applied to the dielectric and the dipoles of the crystal get oriented, displaying positive and negative charges on the opposite sides of the crystal [82].

A particular class of piezoelectric materials called ferroelectric materials are composed of several small

microscopic regions named ferroelectric domains. In these regions, the electric dipoles are oriented in the same direction. These domains are usually randomly oriented in the material and no polarization is observed. Furthermore, a net polarization occurs applying an electric field to the material because the electric dipoles tend to be oriented in the field direction. Most of the piezoelectric materials commonly used are ferroelectrics, due their larger response. [82].

A brief description of the polarization of a ferroelectric material is reported in Figure 4.2.

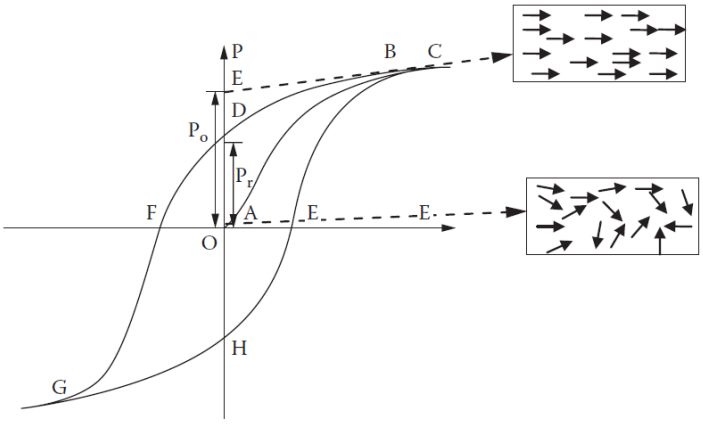

Figure 4.2 Polarization vs Electric field in a ferroelectric material [82].

It is very important to highlight that initially, when the applied field is zero, the ferroelectric domains are randomly oriented and the overall polarization is zero. Increasing the electric field, the domains get oriented and the polarization increases linearly (curve OA). Further increasing the field, more domains get oriented and the curve becomes nonlinear (curve OB) up to the maximum value (point B), where all the domains are oriented. Here the value is called saturation polarization. When the electric field is reduced, the polarization decreases but the curve does not reproduce the previous one. As the field reaches zero, a finite polarization called remnant polarization P_r (point D) is observed. An electric field in the

opposite direction has to be applied in order to remove the remnant polarization. The polarization becomes zero (at point F) when the so-called coercive field $-E_C$ is applied. If the field is increased in the reversed direction beyond $-E_C$, the domains get oriented in the opposite direction and the polarization increases. At G point, the polarization reaches the maximum value (saturation polarization). Another remnant polarization $-P_R$ (point H) is observed if the field is reduced again to zero. Finally, if the field is increased in the positive direction, the remnant polarization disappears. The closed loop described in this process is called the hysteresis cycle [82].

The spontaneous polarization of ferroelectric materials can be removed beyond a temperature called ferroelectric transition temperature or Curie Temperature. Furthermore, ferroelectric materials can be poled, in order to obtain a permanent polarization, applying an external electric field close to this temperature. The poling process can be carried out at room temperature, but higher electric fields and longer times are needed. Indeed, poling at high temperature facilitates dipole orientation. When the temperature is removed the electric field must be applied to the ferroelectric material until it reaches th room temperature [82]. Moreover, another type of polarization called corona poling can be carried out [84]. This poling procedure is based on a non-contact process that applies a high potential corona discharge to the sample. The discharge creates ions, which can charge the sample surface and can orientate molecular dipoles, due to the presence of a high electric field between the corona discharge source and a grounded electrode.

4.4 Piezoelectric polymers

Polymeric piezoelectric materials have several advantages compared to ceramics. In particular, they are flexible and mechanically more stable. Moreover, polymers can be manufactured at much lower temperatures, formed easily into

different shapes and in particular in the form of thin films. Unfortunately, polymers have much lower piezoelectric response compared to ceramic piezoelectrics [82]. The polymers exhibiting the highest response and commonly used in commercial applications are PVdF and its copolymers. This is usually associated to the strong electrical dipole moment of the PVdF monomer unit, which is related to the electronegativity of fluorine atoms compared to those of hydrogen and carbon atoms [85]. Other piezoelectric polymers are Nylon 11, poly(lactic-co-glycolic acid) (PLGA) and polylactic acid.

PVdF homopolymer: PVdF is a semi-crystalline polymer that has five different phases (α, ß, γ, δ and ε) related to different chain conformations. The most important are α, ß and γ and their representation is outlined inFigure 4.3. ß and γ phases are polar, thus being electroactive phases, while α is non-polar [85]. Each chain of PVdF has a dipole moment that is perpendicular to the polymer chain.

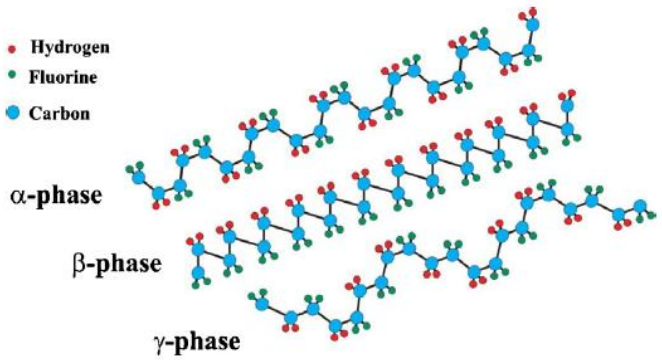

Figure 4.3 Scheme of the chain conformation of different PVdF crystal phases [85].

The ß phase is the one responsible of the piezoelectric behavior of the polymer [86] and is commonly obtained by mechanical stretching of the α phase [87], [88], from melt under specific conditions such as high pressure [89], external electric field applied [90] and ultra-fast cooling [91]. On the other hand,

it is possible to obtain the ß phase from solution crystallization at temperatures below 70°C [92] or by the addition of nucleating fillers such as $BaTiO_3$ [93]. It is thus evident that it is essential to obtain the highest amount of active ß phase through the manufacturing process, in order to enhance the piezoelectric response. PVdF in its polar form is supposed to be a ferroelectric material and this means that it is not only a polar crystal, but that its crystal polarization can be reoriented applying an electric field to the material [81].

PVdF copolymers: Poly(vinylidene fluoride-Trifluoroethylene) (PVdF-TrFE) is one of the most studied copolymer of the PVdF with the aim of increasing polymer performance. Its chain structure is reported in Figure 4.4. It differs from PVdF due to the fact that it shows always the ferroelectric ß crystalline phase when used in specific molar ratios. Indeed, the addition of the third fluoride in the TrFE monomer unit with a large steric hindrance favors the all-trans conformation and induces therefore the ferroelectric ß phase, independently of the used processing method [85]. This situation occurs when the VDF content is between 50 and 80% [94].

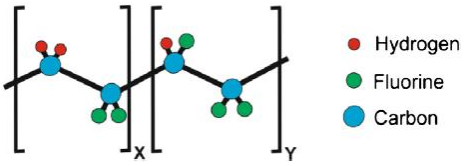

Figure 4.4 Scheme of chain conformation of PVdF-TrFE [85].

Another interesting property of this copolymer is that it shows the Curie temperature below its melting temperature, contrary to PVdF homopolymer [95]. The Curie temperature can vary from 55 to 128 °C for an amount of VDF between 55 and 88 mol%.

It is worth noting that it is not sufficient to obtain a high amount of ß phase in the polymer structure, but it is mandatory to pole the dipoles under an electric field.

Semi-crystalline polymer films are usually stretched in order to preferentially align polymer molecules in the parallel direction of the stretch, because unstretched film usually present isotropy. The deformation of polymer chains induces a higher ß-phase content in the crystals [96], [97]. Moreover, polymers are also poled to align the dipoles normal to the stretch direction [81].

4.4.1 Electrospun piezoelectrics

Recently, the study of energy sources or devices self-powered by harvesting or scavenging energy from ambient, such as solar, thermal and vibration energy has significantly increased interest. In particular, several works were published in literature dealing with the use of nanomaterials with piezoelectric behavior. For instance, PVdF nanofibers show a good set of properties, such as flexibility, lightweight and the possibility to be manufactured in different shapes and thicknesses. All of these features are important parameters for energy harvesting applications and wearable or implantable devices [37].

Since electrospinning has been already reported as a feasible, versatile and cost-effective technique to produce polymeric nanofibers, most of the literature has focused on this process to realize nanofibrous piezoelectric materials. Moreover, conventional fabricating techniques, such as solvent casting, melt blending, spin-coating, etc., require complex and energy-intensive procedures to enhance the piezoelectric behavior of the polymers [86], [87]. On the other hand, poling and stretching of the polymer during material manufacturing are peculiar features of the electrospinning technique. The high voltage applied to the polymeric solution during the

electrospinning process, in fact, is able to orientate the dipoles of polymer chains during material manufacturing [98]. Furthermore, the stretching of the electrostatically charged jet provides a further transformation from alpha to beta crystalline phase [90] and orientate dipolar domains at the nanoscale [99]. These features permit to avoid any post-processing treatment of the polymeric material to increase the ß phase of the electrospun membrane.

The possibility to realize electrospun PVdF-TrFE piezoelectrics has been showed by Persano et al. [100]. It is well known that the amount of active material in electrospun mats is significantly low, due to high mat porosity. Furthermore, fiber mobility is higher compared to film material, thus leading to high sensitivity [101]. For this reason, the use of electrospun piezoelectrics is more cost effective, due to higher specific energy [102].

Electro-mechanical characterization of electrospun piezoelectrics has not deep investigated in literature yet, since most of the studies have been focused mainly on the study of ß phase content in the spun mats or the application of these materials in the biomedical area [103]–[105]. For this reason, most of the experimental campaign will be focused on these characterizations.

4.4.2 Electrospun ferroelectrets

Electrospun PVdF or PVdF-TrFE mats cannot be considered just piezoelectrics, since electrospinning provides charges to the polymeric solution during material manufacturing. Moreover, polymers are usually insulating materials that retain this charge.

Polymer jet accumulates charge during electrospinning [106] due to:

- Charge injection from the metallic needle to the polymeric solution;
- Corona discharge occurring at the needle tip;
- Corona discharge occurring in the surroundings of the Taylor cone.

On the other hand, a fraction of the accumulated charge is dissipated during polymer solidification by solvent evaporation, humid enviroment and charge transfer to the grounded electrode [106]. These phenomena contribute to the presence of residual charge inside the electrospun mats.

Charge retention in electrospun materials is known in literature [106], [107], but not deeply investigated, neither associated to electroactive polymers yet. Therefore, the complex structure of electrospun materials leads to a new definition: ferroelectret instead of piezoelectric. This definition is more precise, due to the simultaneous presence of:

- Ferroelectric nature of dipoles associated to the ß-phase;
- Electret space charge injected during electrospinning and trapped in the dielectric.

4.5 Triboelectricity

Triboelectricity is a type of contact electrification that leads certain materials to become electrically charged after they come in contact with a different material and then are separated. This electrostatic process involves the accumulation of charge on material surfaces and each material retains charge of opposite polarity. These charges remain on the material until they are neutralized by recombination or through a discharge [108]. The reason behind this behavior is the tendency to gain or lose electrons of several materials when in contact with other materials [109]. These phenomena were deeply studied in the past and are reported in literature as triboelectric series [110].

The series allows distinguishing between the relative polarity of the charge acquired during contact and starts from those materials that get more positive charge with respect to those placed in the lower part of the series.

The triboelectric effect is known to be a highly irreproducible phenomenon [111]. This behavior is mainly related to the surface characteristics of the materials and the nature of the contact. It is very important to highlight that the charge transfer is an interfacial phenomenon that is thus affected by surface roughness. Furthermore, material treatments or the presence of contaminants are other important parameters. Moreover, the ambient conditions can affect the amount of charge mainly due to the humidity that can increase surface conductivity, thus reducing charge build-up. Multiple contacts can obviously increase the contact area and consequently the amount of charge transferred [110].

This effect can be positively exploited in order to realize the so-called triboelectric nanogenerators (TENGs) for energy harvesting [109]. According to the triboelectric series, these devices are composed by a multi-layer structure of at least two different materials that are put in repeated contact generating a voltage bias [112]. These devices can be used to supply low power-consuming devices and micro- or nano-systems, such as wearables sensors. Very recently, electrospun mats have been used to realize TENGs, due to their easy fabrication, low cost and high voltage output related to the nano-roughness of fibers [113], [114].

For the sake of our purposes, the triboelectric effect is another phenomenon that can overlap to the electret and piezoelectric response. This is due to the unavoidable contact between a dielectric, e.g. PVdF, and a metal electrode during the measurement of the electric signal associated to a mechanical stress applied to the electrospun samples.

Chapter 5
Experimental campaign on electrospun separators

5.1 Separator manufacturing

The experimental campaign has been mainly carried out using PVdF polymer, due to its aforementioned interesting properties. Regarding the cross-electrospinning technique, PVdF has been combined with Nylon 6,6 (Ny), in order to exploit its high mechanical properties in the final composite material. Furthermore, PEO separators have been studied in order to evaluate nanoparticle dispersion inside the polymeric fibers. PEO, indeed, can be dissolved in water, thus avoiding the use of toxic solvents during material manufacturing.

PVdF Solef 6008 (M_w = 255 kDa) was kindly provided by Solvay Specialty Polymers and was dissolved at a concentration of 15% w/v in Acetone (Ac):Dimethyl sulfoxide (DMSO) (70:30, v/v). Ny Zytel E53 NC010 was kindly provided by DuPont and was dissolved at a concentration of 20% w/v in Triflouroethanol (TFE):Formic acid (FA) (70:30, v/v). PEO (Sigma Aldrich, M_w = 1000 kDa) was dissolved at a concentration of 4% w/v in bidistilled water.

A study on the effect of nanofillers inside nanofibers on the properties of PVdF separators was carried out. Fumed Silica

nanoparticles (SiO_2, average diameter: 7 nm) and Tin oxide nanoparticles (SnO_2, average diameter < 100 nm) were purchased from Sigma-Aldrich and used as received. In this particular section, after polymer dissolution, nanoparticles were added to PVdF polymeric solutions in proper amounts in order to produce membranes containing either 1 wt% and 5 wt% of SiO_2 or 0.5 wt%, 1 wt% and 5 wt% of SnO_2. After 30 min of mechanical stirring homogeneous suspensions were achieved by sonicating the colloidal solutions for 10 minutes by using a UP200St "Hielscher" (Ultrasound Technology) working at 20 W. The sonication was performed in an ice bath to limit solvent evaporation. The plasma-assisted nanoparticle dispersion will be described in a further section.

For the fabrication of separators, a laboratory electrospinning machine was used (Spinbow Lab Unit, Spinbow S.r.l., Italy). The machine was equipped with a multi-jet linear sliding apparatus, equipped with 4 needles, a rotating collector and a syringe pumping system with adjustable flow rate. Solutions were electrospun by using the operating conditions reported in Table 5.1. It is important to notice that the cross-electrospun PVdF-Ny mat was realized using the same apparatus equipped with 6 needles, 2 fed by the PVdF solution and 4 fed by the Ny solution. In this way, a 50:50 w/w polymeric membrane was manufactured, due to the different optimized flow rate of the solutions. This membrane was electrospun using the same needle-to-collector distance and voltage bias of Ny also for PVdF.

Table 5.1 Electrospinning operating conditions for different polymers

	Polymer		
	PVdF	Ny	PEO
Flow rate [ml/h]	0.6	0.3	0.3
Needle-to-collector distance [cm]	15	17.5	20
Voltage bias [kV]	16.5	21	13
Temperature [°C]	22	25	24
Relative humidity [%]	33	40	31

Membranes 30×40 cm^2 were produced for each type of solution composition and used for further characterization.

5.2 Plasma treatments

An investigation of plasma treatments on the properties of PVdF electrospun separators was carried out, aiming at increasing electrolyte uptake. Plasma pre-treatment of the polymeric solution (before the electrospinning process) and plasma post-treatment of the electrospun separators will be described in the following sections. It will be more clear that a synergistic effect of both treatments exists on the increase of electrolyte uptake of electrospun separators.

For the sake of this work, control is referred to a PVdF electrospun separator that has been neither plasma treated, nor spun from a treated polymeric solution.

5.2.1 Plasma pre-treatment

Plasma treatment of electrospinning solutions was previously performed by Shi et al. [80] who demonstrated that treatment of PEO water solution could increase the

electrospinnability of the polymeric solution. Similar results were reported by Colombo et al. on the pre-treatment of a poly(L-lactic acid) PLLA solution, by using a nanosecond-pulsed atmospheric pressure plasma jet, in order to improve the electrospinnability in pure dichloromethane (DCM)[79], [115] avoiding the use of dimethylformamide (DMF), conventionally added to increase the dielectric constant of the solution [116], [117]. Plasma pre-treatment of the PLLA solution allowed obtaining bead-free fibers and mats with good mechanical properties. The typical aspect of an Ar plasma jet during the treatment of water is reported in Figure 5.1.

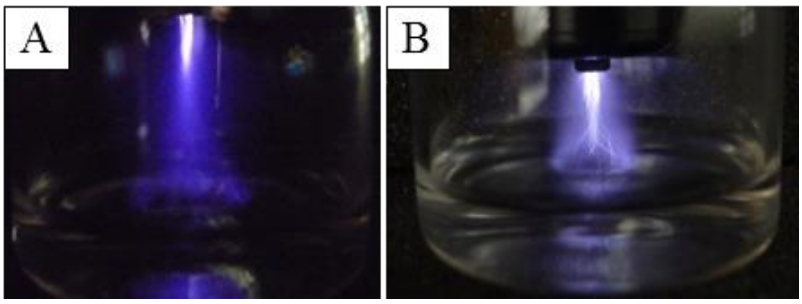

Figure 5.1 Plasma treatment on water: glow regime (A), streamer regime (B).

Plasma pre-treated mats were electrospun from a PVdF solution (12 ml) exposed to a nanosecond pulsed atmospheric pressure Ar plasma jet for 120s, using the following operating conditions: peak voltage (PV) of 22 kV, pulse repetition frequency (PRF) of 1 kHz and a stand-off of 5mm, as reported in [79].

Similarly, to what reported in literature for PLLA, the exposure of the PVdF electrospinning solution to an atmospheric pressure plasma jet permits the production of defect free fibers. Furthermore, good quality PVdF separators easy to handle also after imbibition in the electrolyte can be produced, as will be described in electrolyte uptake section.

5.2.2 Plasma post-treatment

Both control and pre-treated PVdF separators were plasma treated by means of an atmospheric pressure dielectric barrier discharge (DBD) for 5 minutes. The DBD was operated in ambient air and consisted of two aluminum electrodes. The high voltage (HV) upper electrode had a surface of 6x6 cm^2, while the grounded electrode had a surface of 15x9 cm^2. The HV electrode was covered by a 1 mm thick alumina layer and the gap between the dielectric and the grounded electrode was 1 mm. The HV electrode was driven by a nanosecond-pulsed generator, producing high voltage pulses with a slew rate of few kV/ns, a PV of 7–20 kV into a 100–200 Ω load impedance and a PRF of 1000 Hz. During the post-treatment of PVdF electrospun separators (Figure 5.2), PV and PRF were kept constant at 20 kV and 125 Hz, respectively.

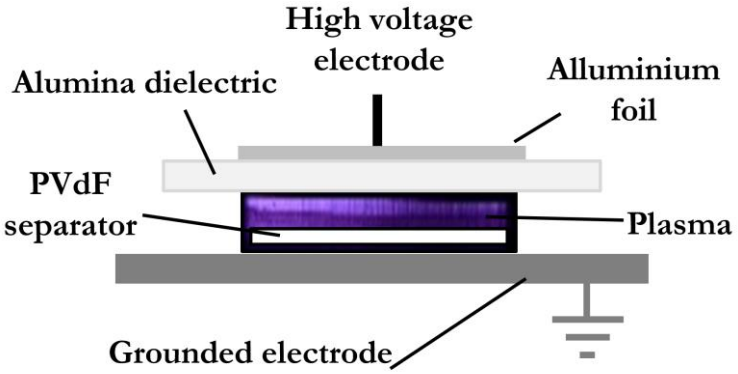

Figure 5.2 Schematic of the atmospheric pressure DBD during treatment.

5.3 Material Characterization

Several characterization techniques were carried out in order to study solution properties and morphological, thermal, mechanical, electrical and electrochemical properties of electrospun separators.

5.3.1 Polymeric solution rehometry

This study on the polymeric solution has been done in order to study the effect of plasma pre-treatment on the rheological properties of the solution.

Viscosity measurements were carried out using an Anton Paar Rheometer MCR 102 equipped with a cone-plate configuration (50 mm diameter, 1°). Experiments were performed at constant temperature of 23°C controlled by the integrated Peltier system and a Julabo AWC100 cooling system. A solvent trap (H-PTD200) was used to avoid solvent evaporation during the measure. The flow curves of both untreated and plasma-treated PVdF solution (15% w/v) were acquired at shear rate ranging from 0.01 s^{-1} to 10000 $s^{-}1$.

The 15% w/v PVdF solution was analyzed by means of a rheometer before and after the plasma treatment. The plasma treated solution was characterized by viscosity values higher than those showed by the untreated solution in the whole range of shear rate investigated (0.01 s^{-1} to 10000 s^{-1}). The comparison of the viscosity values at a fixed shear rate of 0.01 s^{-1} (approaching the zero-shear viscosity range), the viscosity values were 3.77 Pa*s and 0.85 Pa*s for the plasma treated solution and the untreated solution respectively. This particular behavior could be related to the development of intermolecular interactions between PVdF macromolecules due to the plasma treatment.

5.3.2 Scanning electron microscope and energy dissipation spectroscopy

A scanning electron microscope (SEM) (PHENOM PROX Desktop SEM) equipped with an energy dissipation spectroscopy probe was used applying an accelerating voltage of 15 kV on samples sputter-coated with gold, in order to evaluate fiber quality, fiber diameter distribution and to

analyze the presence of inorganic nanoparticles. Fibermetric software (Phenom) permitted to evaluate fiber diameter distribution through the measurement of about 200 fibers and the results were given as average diameter ± standard deviation.

Concerning the study of pristine PVdF (not filled with nanoparticles) and PVdF nanofilled separators, fiber morphology is showed in Figure 5.3. In particular, pristine PVdF fibers are shown in Figure 5.3a. Good quality fibers without defects have been spun. On the other hand, a commercial Celgard 2400 separator is shown in Figure 5.3b. Comparing the morphology, commercial separators are realized in thin films, having a porosity around 40%, while an electrospun membrane is not created in a form of a film but as a non-woven tissue made of several fibrous layers. As can be seen in the cross section (Figure 5.3a inset), the path from the surface to the bottom of the electrospun membrane is characterized by a significant tortuosity, due to the randomly oriented pattern of fibers. Interconnected pores, even if large, do not cross directly the material, thus preventing short circuit if the membrane thickness is optimized. On the contrary, Celgard porosity is characterized by through holes from one surface to the other. Battery nanofibrous separators containing 1% w/w and 5% w/w of either SiO_2 or SnO_2 were successfully electrospun. Indeed, SEM images in Figure 5.3c-f show that each electrospun membrane was made up of good quality fibers without bead-like defects. The distributions of fiber diameters (average values and standard deviations) are also reported (mean fiber diameters range between 480 nm and 670 nm).

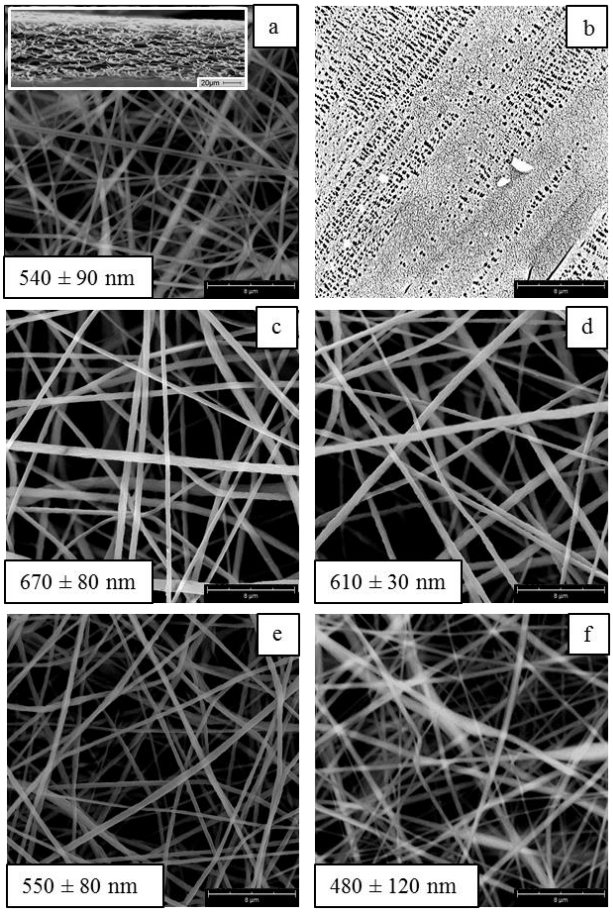

Figure 5.3 SEM images of PVdF pristine polymer (a transversal section is shown in the inset) (a), Celgard 2400 (b), and PVdF containing 1 wt% SiO_2 (c), 5 wt% SiO_2 (d), 1 wt% SnO_2 (e), 5 wt% SnO_2 (f); Scale bar = 8 µm.

EDS spectra of electrospun membranes were collected to verify the presence of nanoadditives in electrospun mats. EDS spectra are reported in Figure 5.4 in the range 0-8 keV, since at energies higher than 8 keV no peaks were detected. Samples filled with the nanoparticles showed the characteristic peaks of Si and Sn elements, whose intensities were proportional to the weight content of inorganic particle.

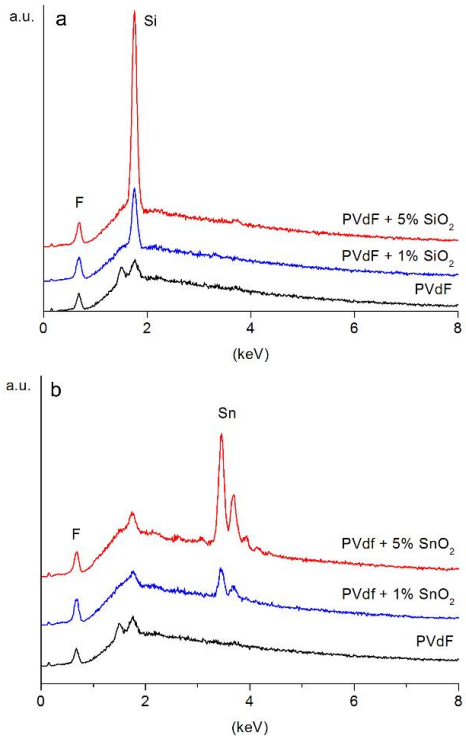

Figure 5.4 EDS spectra of PVdF samples loaded with SiO_2 (a) and PVdF samples loaded with SnO_2 (b).

Concerning plasma treated sampled, PVdF solutions, either untreated (control) or pre-treated via atmospheric pressure plasma, were successfully electrospun and the morphology of resulting fibers is shown in Figure 5.5. Control mats (Figure 5.5A) displayed beaded fibers, i.e. showed a large number of defects along the fiber axis which are known to worsen mat mechanical properties [118]. The plasma pre-treatment of the PVdF solution caused a remarkable decrease of beads number, and therefore an improvement of the electrospinnability, leading to randomly arranged fibers with a uniform mean diameter of about 336 ± 85 nm (Figure 5.5B). This finding is in agreement with previously reported results on plasma pre-treatment of different polymeric solutions [79], [80], [115]. The plasma post-treatment of the electrospun mats did not induce

any modification of the fiber morphology, since no evidence of mat damage was found, as shown in Figure 5.5C and Figure 5.5D.

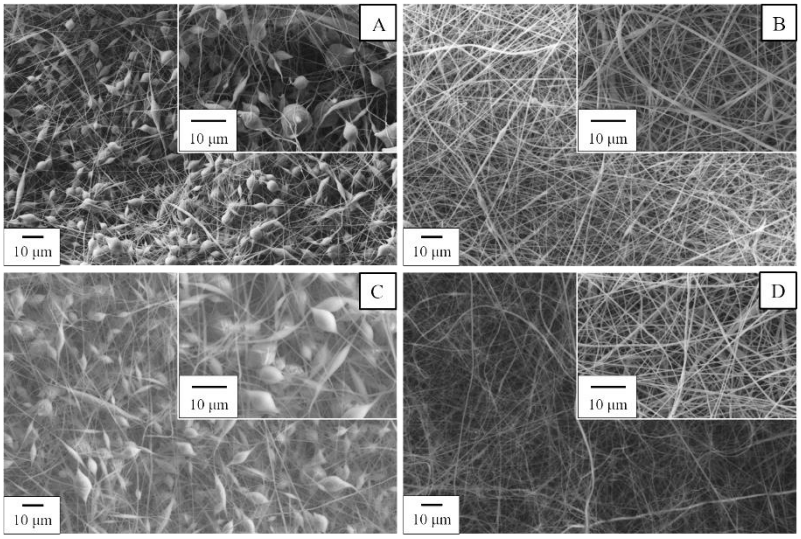

Figure 5.5 SEM images of electrospun samples: (A) control mat obtained without plasma treatment of the electrospinning solution (control), (B) fibers obtained from a pre-treated solution (pre-treatment), (C) control mat post-treated with nanopulsed DBD (post-treatment), (D) pre-treated mat post-treated with nanopulsed DBD (pre&post-treatment). Magnification: 2000X (main image) and 6000X (insert).

The swollen fibers of the separators soaked in the electrolyte are compared in Figure 5.6. It is possible to observe that all samples retained the porous fibrous structure. Control and post-treated specimens (Figure 5.6A and Figure 5.6C respectively) still showed the presence of beads along the fibers. All soaked separators displayed an increase in fiber diameter due to high fiber swelling in the electrolyte solution (in this case, it was not possible to evaluate fiber diameters). Furthermore, fibers became more entangled, having larger contact to each other, thus decreasing the overall pore dimension of the separator. This behavior is related to the absorption of a large amount of electrolyte, due to a strong

interaction between the polymer and the electrolyte solution [118].

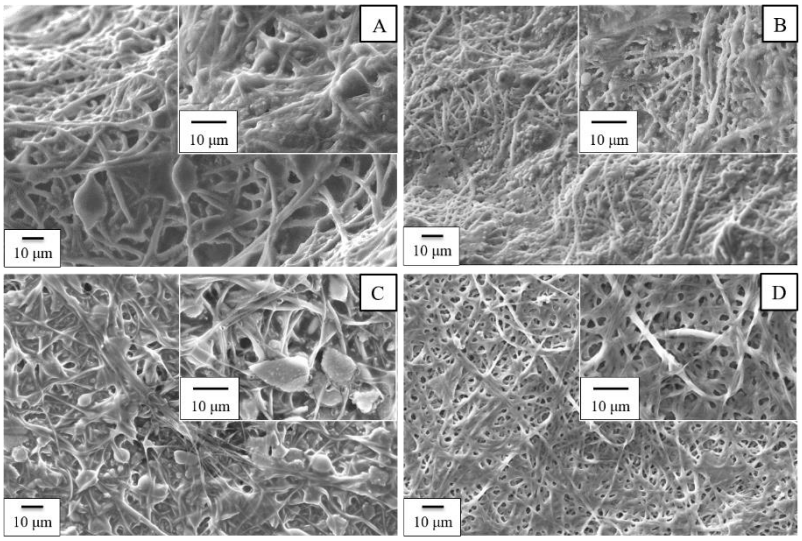

Figure 5.6 SEM images of electrospun samples soaked in electrolyte: (A) control, (B) pre-treatment, (C) post-treatment, (D) pre&post-treatment. Magnification: 2000X (main image) and 6000X (insert).

Concerning cross-electrospun Ny-PVdF separator, fiber morphology is reported in Figure 5.7. Good quality fibers without bead-like defects have been successfully electrospun.

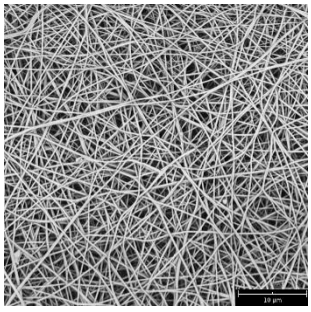

Figure 5.7 SEM image of cross-electrospun Ny-PVdF separator.

It is possible to observe that the diameter distribution of the fibers is not homogeneous. Fiber diameter is strongly affected by solvent system (e.g. solution viscosity) and by polymer

concentration in the solution [119]. It has been reported that Ny 6,6 fibers electrospun from FA solution, using the same polymer concentration of this work, have diameters below 200 nm [120]. Moreover, analyzing SEM image it is possible to distinguish between two populations: PVdF fibers, which have been previously measured about 500 nm (see Figure 5.3A), and Ny fibers. A deep investigation of fiber morphology of cross-electrospun mats has not reported in literature yet. Furthermore, it is possible to hypothesize that the partial overlap of the two different polymer jets during whipping instability can alter fiber diameter, but not enough to obtain one diameter population.

5.3.3 Thermo-gravimetric analysis

Thermogravimetric analysis (TGA) were performed to evaluate thermal stability and to quantify the inorganic fraction in the filled PVdF separators, using a thermo-gravimetric analyzer (TA Instruments TGA2950) from room temperature to 600°C in air, with a heating rate of 10°C/ min. Results are shown in Figure 5.8.

Nanoparticle addition did not change the thermal degradation mechanism of the polymer, neither the initial degradation temperature that is about 320°C for all tested membranes. Pristine polymer reached zero mass at the end of the test. Samples containing 1 wt% and 5 wt% of SnO_2 showed about 2% and 6% residue of the initial mass, respectively. Both samples containing silica showed a residue of only 1%. This low value can be explained by hypothesizing that during the degradation of the sample, some volatile silicon-based compounds were generated. In particular, it is expected that the presence of hydrogen and fluorine in polymer chain led to the formation of gases at the high temperatures here considered, i.e. silane (SiH_4) and tetrafluorosilane (SiF_4) [68]. However, the

aforementioned EDS results confirmed qualitatively the presence of SiO_2 in the fibers according to the expected amount.

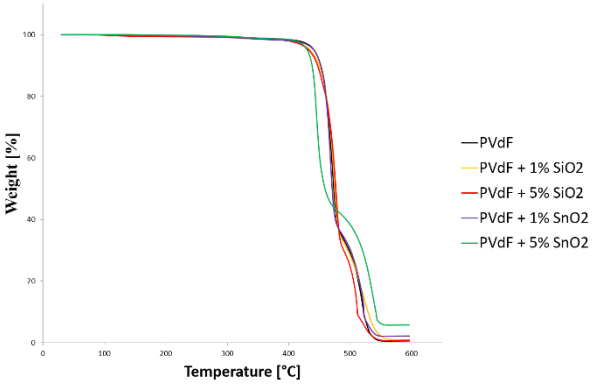

Figure 5.8 Thermogravimetric curves of PVdF electrospun samples.

5.3.4 Differential scanning calorimetry

Differential Scanning Calorimetry (DSC) measurements have been carried out on PVdF electrospun separators and in particular on pristine PVdF, plasma treated PVdF separators and on nanofilled PVdF separators.

DSC measurements were carried out using a TA Instruments Q100 DSC equipped with the Liquid Nitrogen Cooling System accessory. DSC scans of electrospun samples were performed from -50°C to 200°C at a heating scan rate of 20°C/min in helium atmosphere.

Calorimetric curves of PVdF electrospun separators, both treated and not treated by means of plasma, are reported in Figure 5.9. All samples were semicrystalline and the only appreciable thermal event in the DSC curve was melting, characterized by a temperature around 170°C and a melting enthalpy of about 55 J/g. Therefore, the plasma treatments here performed did not affect thermal properties of PVdF electrospun separators.

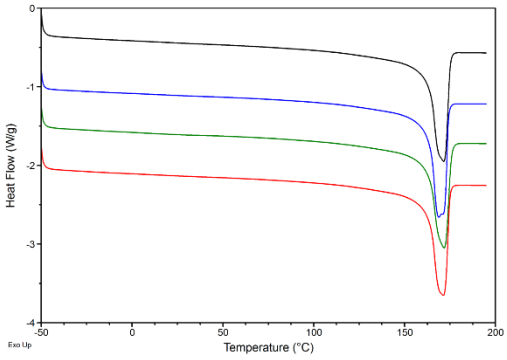

Figure 5.9 Calorimetric curves of control (black), pre-treated sample (red), post-treated sample (blue) and pre&post treated sample (green).

No differences among pristine and nanofilled samples have been found, highlighting that nanoadditives did not affect crystalline properties of the polymer. For the sake of brevity, curves have not been reported.

5.3.5 Mechanical properties

Tensile tests were carried out with a tensile testing machine (Instron 4465) on rectangular electrospun membranes (5 mm wide). The gauge length was 20 mm and the crosshead speed was 2 mm/min. Tests were performed on 10 specimens for each mat and results were processed through the Weibull probability distribution, providing the 63.2^{th} percentiles (α, scale parameter) with the relevant confidence intervals at 90% probability. The following mechanical data were provided: (i) elastic modulus, (ii) stress-at-break and (iii) elongation-at-break.

Figure 5.10 shows elastic modulus, stress-at-break and elongation-at-break of PVdF separators. PVdF loaded with both type of additives in each weight concentration showed higher Young's moduli with respect to pristine PVdF (Figure 5.10a). Furthermore, the addition of 1 wt% of SiO_2 led to a remarkable increase of elongation-at-break and a small increase of stress-

at-break, thus making the membrane tougher than the pristine PVdF. On the other hand, the addition of SnO_2 greatly increased stress-at-break, with a consequent decrease in elongation-at-break, thus making the membrane stiffer than the pristine PVdF. Results show that a small amount of nanoadditive (about 1 wt%) is highly effective in changing membrane mechanical properties, thus paving the way to the industrial use of this type of nanocomposite membranes. It is reported that, typical battery manufacturing procedures require separators able to sustain a stress of about 13 MPa without being damaged [64]. Among the investigated samples, PVdF loaded with SnO_2 exhibits the best mechanical properties, suitable for this application. Therefore, the effect of SnO_2 amount was further investigated in order to achieve the best performance in terms of mechanical property increase of the separator. In particular, it was possible to observe a remarkable increase of stress-at-break by adding only 0.5 wt% of SnO_2 to PVdF, with respect to pristine polymer (Figure 5.10b). The elongation-at-break decreased with respect to pure PVdF but to a less extent than with higher concentrations (Figure 5.10c). It has to be highlighted that the positive effect of SnO_2 on mechanical and electric properties of PVdF Lithium battery separators is here reported for the first time.

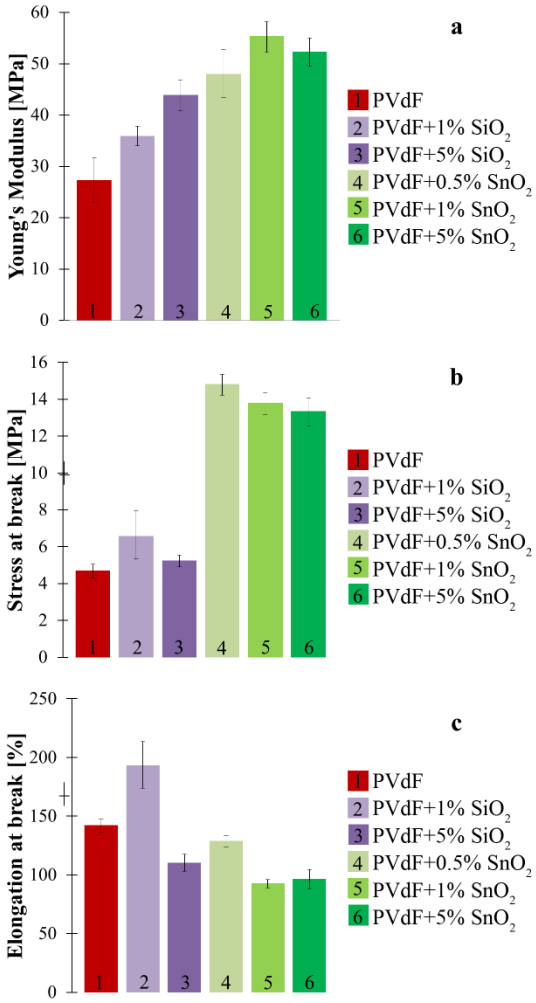

Figure 5.10 Mechanical characterization of PVdF separators: elastic modulus (a), stress-at-break (b) and elongation-at-break (c).

Figure 5.11 shows mechanical characterization of PVdF plasma treated separators, i.e. elastic modulus, stress-at-break and elongation-at break. Control sample shows a very low Young's modulus, as well as stress-at-break, that was attributed to the presence of bead defects along the fiber axis,

which is known to worsen mat mechanical stability, due to the reduction of the cohesive force between the fibers of the non-woven fiber mats, as previously reported by Huang et al. [118]. On the other hand, plasma pre-treatment leads to a massive improvement in separator mechanical properties, due to the achievement of better fiber morphology and a lower amount of defects. This behavior is directly related to the aforementioned enhanced stiffness of plasma pre-treated separators, compared to control mat. Plasma post-treatment induced a slight decrease of the mechanical properties, as already observed by Dolci et al. for post-treated electrospun mats [121].

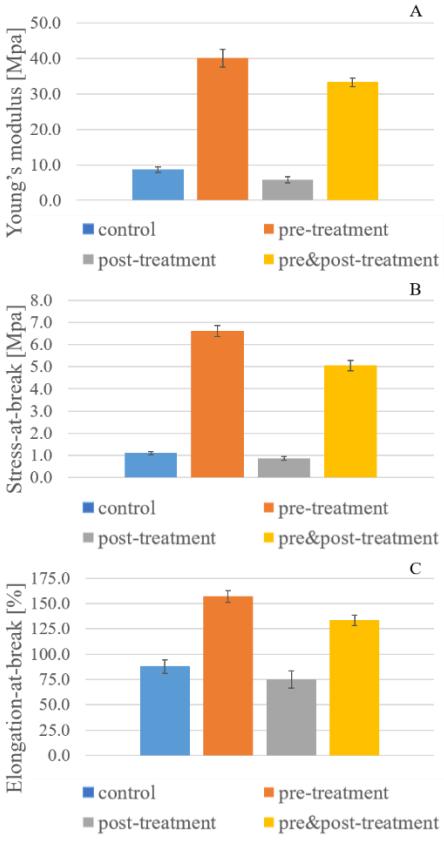

Figure 5.11 Mechanical characterization of electrospun PVdF separators: (A) elastic modulus, (B) stress at break and (C) elongation at break.

Concerning mechanical properties, the performance of the aforementioned separators and cross-electrospun separator are compared in Figure 5.12. This comparison highlights that pristine PVdF is not suitable for industrial applications, while cross-electrospun separator fulfills battery assembly requirements in terms of stress-at-break, displaying a value of about 13 MPa. This behavior is similar to that of PVdF filled with 0.5 wt% of SnO_2, but has been achieved without the use of any nanoadditive inside the fibers. The choice of the proper supporting polymer (e.g. nylon) can be tuned in order to

increase both mechanical and electrochemical properties of the separator.

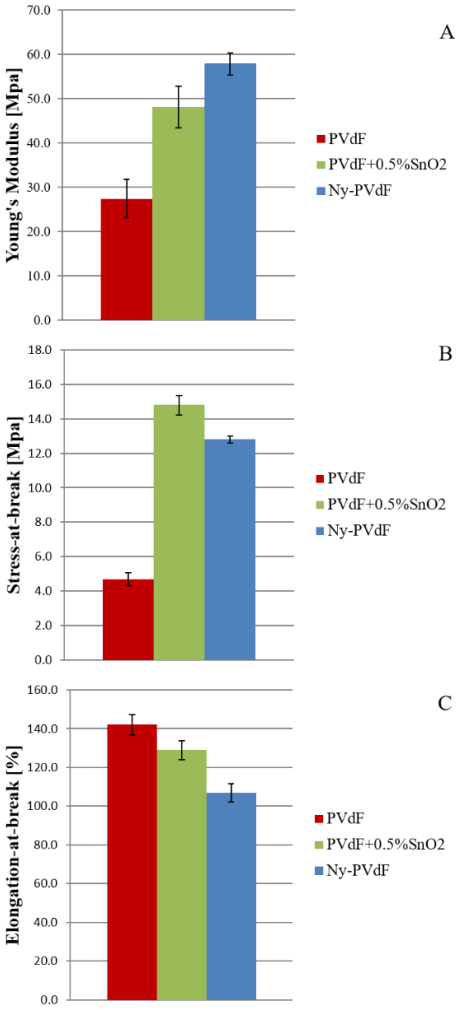

Figure 5.12 Mechanical property comparison between pristine PVdF, PVdF filled with 0.5 wt% of SnO_2 and cross-electrospun Ny-PVdF: (A) elastic modulus, (B) stress at break and (C) elongation at break.

5.3.6 Electronic conductivity

Since silica and tin oxide are made of conventionally active materials for LIB electrodes, i.e. Si and Sn, electronic

conductivity of the membranes non-soaked in the electrolyte was measured, in order to ensure electrical insulation. Samples placed between two electrodes have been subjected to DC 5 kV/mm electrical field. The charging current flowing through the separators was measured until the steady-state conduction current was reached. The high voltage electrode had a 27 mm diameter while the lower electrode was divided in a central electrode of around 15mm diameter surrounded by a 27 mm guard ring connected to ground. This configuration was chosen to prevent a possible contribution of surface currents to the measurement. Each sample was preliminarily sputter-coated with gold replicating electrode area on sample. A sketch of the experimental apparatus is reported in Figure 5.13a, while the gold sputtering of electrospun and Celgard 2400 separators are shown in Figure 5.13b and c, respectively. Thanks to this technique, the electronic conductivity can be determined by measuring the conduction current through an ammeter, as reported in the equations (5.1–5.4):

$$J = \frac{I}{S} \qquad (5.1)$$

$$J = \sigma * E \qquad (5.2)$$

$$E = \frac{V}{d} \qquad (5.3)$$

$$\sigma = \frac{(E * S)}{I} \qquad (5.4)$$

where J = electric current density, I = electric current, S = electrode area, σ = electronic conductivity, E = electric field, V = applied voltage, d = sample thickness.

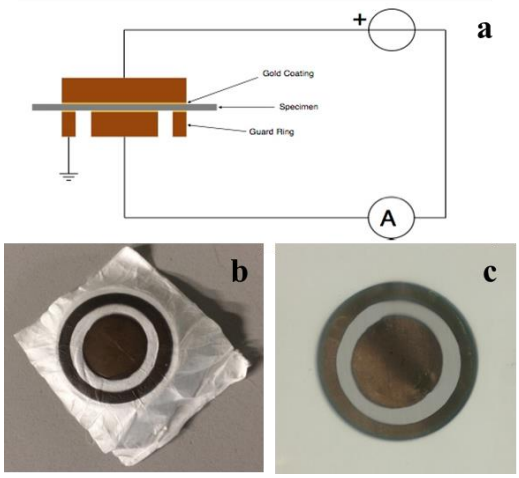

Figure 5.13 DC conductivity measurement system (a) and pictures of gold sputtered electrospun (b) and Celgard 2400 (c) separators.

Electronic conductivity results are reported in Table 5.2. At room temperature the values of conductivity of all electrospun mats are in the range of insulating materials. Indeed, electronic conductivity is well below 10^{-8} S/m, which is the limit value for a material to be considered insulating for electronic charge carriers. In order to investigate the change of electrical conductivity as a function of the temperature, the same analysis was carried out also at 40°C and 70°C. These measurements were performed only on the nanostructured separators filled with 1 wt% of inorganic additives since will be later demonstrated that such a low concentration is enough to positively affect electrolyte uptake. At the high temperatures investigated, the electrospun membranes are still insulating materials, being the electronic conductivity much lower than 10^{-8} S/m.

Table 5.2 Electronic conductivity of electrospun and Celgard 2400 separators at 25°C, 40°C and 70°C.

Sample	**Conductivity [S/m] at 25°C**	**Conductivity [S/m] at 40°C**	**Conductivity [S/m] at 70°C**
PVdF	$1.8 \cdot 10^{-14}$	$1.7 \cdot 10^{-13}$	$7.2 \cdot 10^{-12}$
PVdF+1% SiO_2	$7.9 \cdot 10^{-14}$	$2.9 \cdot 10^{-13}$	$3.9 \cdot 10^{-12}$
PVdF+5% SiO_2	$1.3 \cdot 10^{-13}$	n.d.	n.d.
PVdF+1% SnO_2	$8.4 \cdot 10^{-14}$	$5.0 \cdot 10^{-13}$	$6.5 \cdot 10^{-12}$
PVdF+5% SnO_2	$7.9 \cdot 10^{-13}$	n.d.	n.d.
Celgard 2400	$1.4 \cdot 10^{-15}$	$1.7 \cdot 10^{-15}$	$4.5 \cdot 10^{-15}$

The Arrhenius plot of conductivity reported in Figure 5.14 shows that the addition of nanoparticles to PVdF has the effect of decreasing the activation energy related to electronic conduction mechanism. Therefore, the increase of electronic conductivity at high temperature is smaller in the case of loaded membranes with respect to pristine polymer. In addition, by considering the value of activation energy, at very high temperatures, close to thermal runaway, the loaded membranes have lower electronic conductivity than pristine PVdF, thus ensuring higher safety against short circuit.

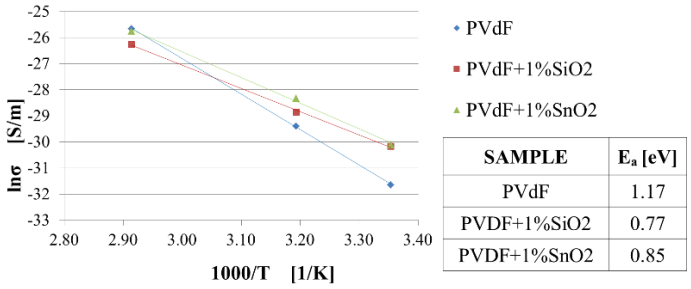

SAMPLE	E_a [eV]
PVdF	1.17
PVDF+1%SiO2	0.77
PVDF+1%SnO2	0.85

Figure 5.14 Arrhenius plot based on the temperature dependence of electronic conductivity of electrospun membranes and activation energy (E_a) values.

5.3.7 Contact angle measurements

Static contact angle measurements were performed on electrospun membranes by using a KSV CAM101 instrument under ambient conditions by recording the side profiles of electrolyte drops for image analysis. The shape of the drop was recorded in a time range of 0–2 s, by collecting an image every 66 ms. At least four drops for each sample were tested.

Contact angle measurements were carried out to evaluate the wettability of the different separators (i.e. pristine PVdF, PVdF filled with nanoparticles and Celgard) by the electrolyte solution. Electrolyte drop on Celgard (Figure 5.15b) displayed a contact angle of about 61° and it was not completely absorbed by the separator. On the contrary, all mats were able to completely absorb the electrolyte drop within 2 s after the beginning of the analysis. However, by comparing the very initial stage of the experiments, differences in the rate of drop absorption emerged. In Figure 5.15c-e the shape of the drops and the corresponding contact angles values at 66 ms are reported for pristine PVdF and for PVdF mats loaded with 5 wt% of nanoparticles. The presence of SiO_2 accelerated electrolyte drop absorption so that at 66 ms the drop was already completely absorbed by the mat. On the contrary, the electrolyte contact angle at 66 ms in the case of SnO_2 loading

was higher when compared with the pristine PVdF mat, thus confirming the results of capillarity measurements, as can be highlighted in the following section. It is pointed out that when only 1 wt% of nanoparticles were added to the polymer, no significant differences in contact angles were observed.

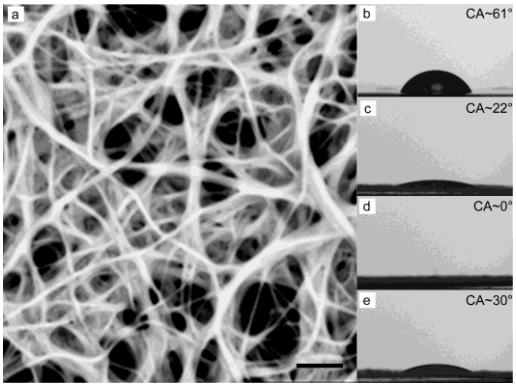

Figure 5.15 (a) SEM image of PVdF electrospun separator soaked in electrolyte; scale bar = 5 μm. Electrolyte drop in contact with Celgard (b), pristine PVdF (c) and PVdF containing 5 wt% SiO2 (d) and 5 wt%SnO2 (e).

5.3.8 Capillarity measurements

Electrolyte uptake was preliminary evaluated through capillarity measurements. Each membrane (1×5 cm^2) was fixed to a rectangular PTFE frame and was vertically immersed in the electrolyte solution for a couple of millimeters. The electrolyte solution instantaneously wet the membrane and its level rose under the capillary action. Electrolyte uptake of the different membranes was evaluated by comparing the time needed for the electrolyte to reach the height of 4 cm. The height of 4 cm was chosen to ensure the achievement of steady state condition in the rate of electrolyte uptake.

Results of capillarity measurements for PVdF electrospun separators (pristine and filled with nanoparticles) are reported in Table 5.3. The reported values were calculated by considering the time taken for the electrolyte to reach the height of 4 cm in the pristine PVdF as a reference (about 400 s). Analyzing the

data reported in Table 5.3, it is possible to observe that the presence of nanoparticles inside the nanofibers significantly affects electrolyte uptake. In particular, SiO_2 nanoparticles accelerate electrolyte uptake, while SnO_2 nanoparticles slow down the process with respect to pristine polymer. This behavior could be associated to the high polar nature of SiO_2 nanoparticles, which can locally increase membrane polarity, thus favoring electrolyte uptake. However, all the tested electrospun separators are able to uptake a higher amount of electrolyte than commercial Celgard 2400. Indeed, when the latter was immersed in electrolyte solution for capillary uptake measurements, the level of electrolyte after one hour rose a little bit and never reached the height of 4 cm.

Table 5.3 Relative time to reach 4 cm in capillarity measurements for electrospun samples, referred to pristine PVdF as reference.

Sample	**Relative time to reach 4 cm**
PVdF	1.0
PVdF + 1% SiO_2	1.0
PVdF + 5% SiO_2	0.6
PVdF + 1% SnO_2	1.3
PVdF + 5% SnO_2	1.5

5.3.9 Electrolyte uptake measurements

Separators were vacuum dried at 80°C for 2 hours before electrolyte uptake procedure using a static laboratory dryer (BUCHI B-585). Electrolyte uptake measurements were performed in dry box (MBraun Labmaster SP glove box - water and oxygen content < 0.1 ppm), soaking 10 round separators for each investigated case in 1.3 ml of LP30 electrolyte for 2 hours. The procedure is reported in Figure 5.16. Uptake was evaluated using the following equation:

$$Uptake\ [\%] = \frac{m_{wet} - m_{dry}}{m_{dry}} * 100 \quad (5.5)$$

where w_{wet} was the weight of the soaked membrane, while w_{dry} the weight of dried separator.

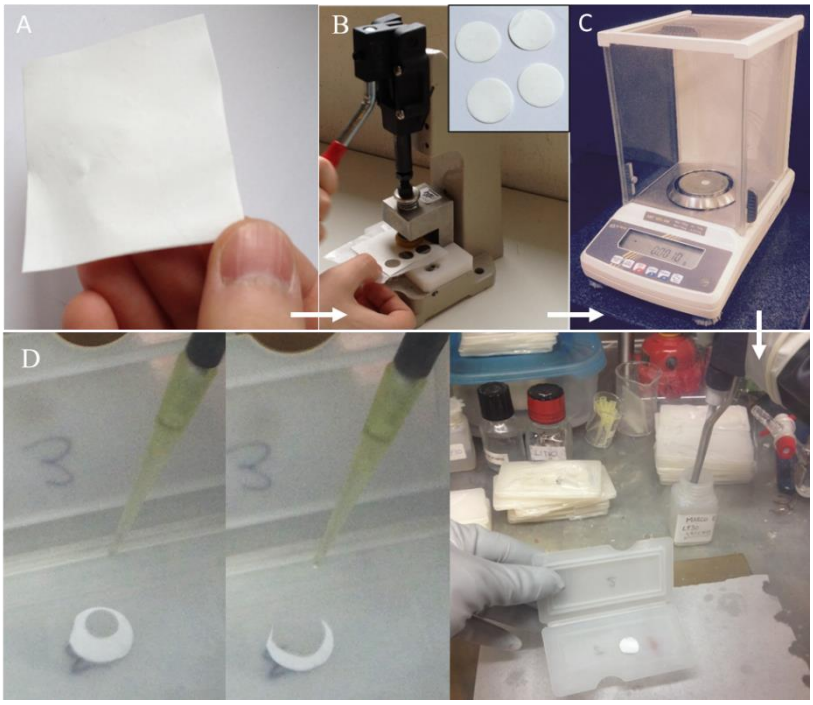

Figure 5.16 Representative pictures of the protocol implemented for electrolyte uptake evaluation: PVdF electrospun mat (A), cutting process of round separators (highlighted in the insert) from the mat (B), weight measurement of separator (C), electrospun separator being soaked in LP30 in dry box (D).

Considering plasma treated separators, the electrolyte uptakes of PVdF electrospun separators are reported in Figure 5.17. Control mat exhibited electrolyte uptake of about 500%. Fiber morphology improvement, due to plasma pre-treatment, led to larger uptake values, up to 800%. In addition, the post-treatment induced an increase of the electrolyte uptake, since post-treated mats showed an uptake of about 800%. Furthermore, it is possible to highlight a synergistic effect between plasma pre-treatment and plasma post-treatment, leading to a huge uptake improvement in the case of pre&post-

treated separator, where an electrolyte uptake larger than 1200% was achieved. Confidence interval associated to uptake measurements of pre&post-treated samples are quite larger compared to those associated to the other samples. It is important to highlight that electrospun mats are not homogeneous, due to the random fiber deposition on the collector and this could result in a not homogenous effect of the plasma post-treatment. Furthermore, the pre&post-treated sample uptake measurement is affected by the combination of the pre-treatment and post-treatment uncertainties.

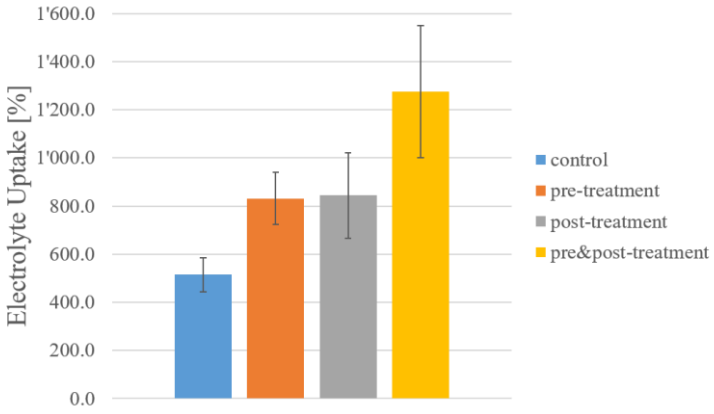

Figure 5.17 Electrolyte uptake of PVdF electrospun separators.

It is worth noting that control electrospun separators showed a worse behavior in terms of handability after being soaked in electrolyte with respect to pre-treated electrospun samples, as reported in Figure 5.18. Indeed, pre-treated separators were stiffer than control specimens and they kept the round shape also after swelling.

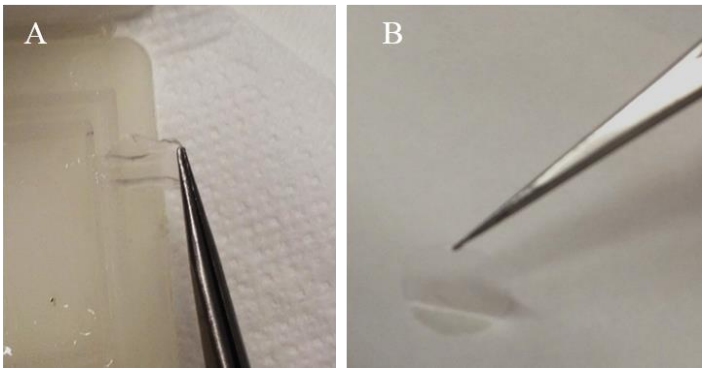

Figure 5.18 Comparison of control (A) and pre&post-treated (B) electrospun separators after being soaked in electrolyte.

It is important to highlight that the electrolyte uptake of Ny-PVdF separators is about two times larger than PVdF, as shown in Table 5.4. This result can be related to the lower MacMullin number of these separators, as described in the following section.

Table 5.4 Electrolyte uptake comparison between PVdF and Ny-PVdF electrospun separators

Sample	Electrolyte uptake [%]
PVdF	514±81
Ny-PVdF	1102±70

5.3.10 X-ray photoelectron spectroscopy

X-ray photoelectron spectroscopy (XPS) measurements were carried out on a SPECS Hemispherical analyzer using a Mg K_α X-ray source (1253.6 eV). The X-ray source in the standard conditions had been working at a 100 W, 10 kV, and 10 mA. The base pressure of the instrument was $9*10^{-10}$ Torr and an operating pressure of $2*10^{-8}$ Torr was adopted. A pass energy of 40 eV and 20 eV was used for widescans and narrowscans, respectively. For acquiring the spectra, a take-off angle of 45° was used. The semi-quantitative surface analyses were carried out by the determination of the photoelectron peak areas

obtained by multiplying the experimental values with the appropriate sensitivity factor. Calculation of the areas corresponding to the different photoelectron peaks and the curve fitting elaborations were done by means of PeakFit software (version 4, from SPSS Inc.).

This technique has been carried out in order to study the effect of plasma treatment on electrospun separators. The widescans of the four set of analyzed samples are shown in Figure 5.19. These spectra show that in the outermost layers of control and pre-treated samples, carbon (~285 eV) and fluorine (~688 eV) only are present, while the post-treated and pre&post-treated ones present oxygen too (~533 eV).

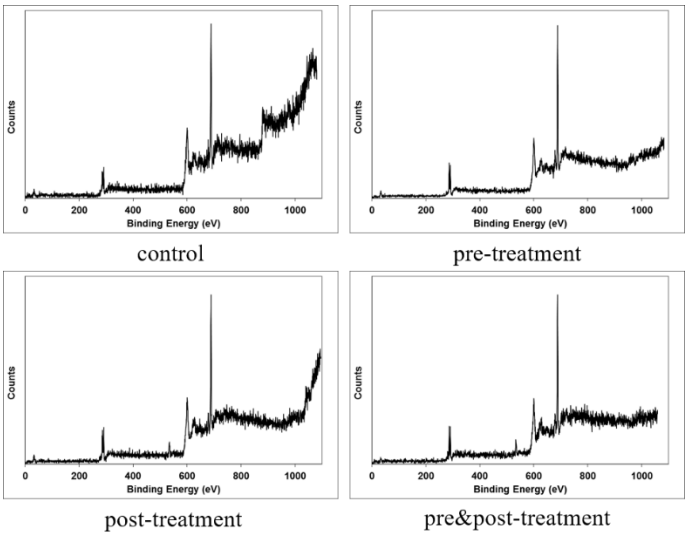

Figure 5.19 Widescans of the analyzed samples.

The atomic percentual composition of each sample has been calculated from the peak areas and the results are shown in Table 5.5. The values shown in the table have been corrected subtracting the contribution of the hydrocarbon contamination, usually found in samples analyzed by XPS, determined by peak fitting the C_{1s} envelope. From these data is evident that pre-treated sample surface composition doesn't differ significantly

from control sample one, although a slightly lower fluorine concentration is present, while the post treatment introduces on the surface a relatively low concentration of oxygen containing functionalities and determines a presence of a lower fluorine concentration on the surface.

Table 5.5 Surface composition (atomic percentage) as obtained from XPS analysis after correction from hydrocarbon contamination.

Sample	C	F	O
Control	52	48	-
Pre-treated	53	47	-
Post-treated	51	46	3
Pre&post-treated	52	45	3

More information can be obtained from the analysis of the single regions (i.e. F_{1s}, C_{1s} and O_{1s}). In all the samples F_{1s} peak has been curve fitted with a single component centered at 688.3±0.1 eV. Its position is in accordance with the PVdF chain structure and with what reported in literature [122].

The control sample C_{1s} curve fitting elaboration shows the presence of three contributions (Figure 5.20). The one centered at 285.0±0.1 eV is attributable to the hydrocarbon contamination, while the ones centered at 286.5±0.1 eV and 290.9±0.1 eV are due to CH_2-CF_2- and CH_2-CF_2-, respectively. The position of these last two components is in accordance with literature [122] and their area ratio is 49:51 close to what expected from the polymer structure (50:50).

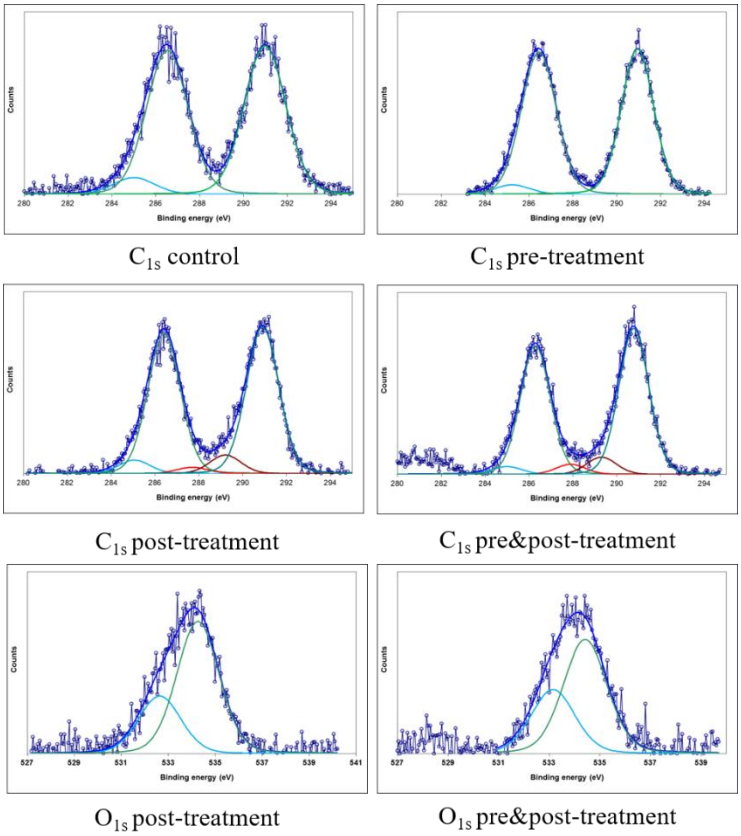

Figure 5.20 Results of C_{1s} and O_{1s} envelope curve fitting for the analyzed samples.

The pre-treated sample C_{1s} envelope has been curve fitted using the same three components present in the control sample C_{1s}, but this time their area ratio between CH_2-CF_2- and CH_2-CF_2-components is 51:49 indicating that during the pre-treatment some defluorination occurs.

The C_{1s} envelope of the post-treated and pre&post treated samples, besides to the three components present in the previous samples, shows the presence of two new contributions centered at 287.9±0.1 eV and 289.3±0.1 eV that could be assigned to -CF_2-$\underline{C}$H-(OH)- and CF_2-$\underline{C}$OOH(R) functionalities, respectively.

These assignments are in accordance with the presence of oxygen on the surface and with the O_{1s} curve fitting (Figure 5.20) resulting in the presence of two contributions: the first (less intense) centered at 532.9±0.1 eV due to O-C=O groups, the other centered at 534.4 ±0.1 eV due to O-C=O, and -CF_2-CH-(OH). The relative abundance of the four main components of the C_{1s} envelope are 45:2:6:47 in the post-treated sample, while are 43:3:6:48 in the pre&post-treated one.

These results suggest the hypothesis that, during the pretreatment, the presence of the solvent determines, as the main polymer modification reaction, a process through which radicals are formed mainly in the perfluorinated portion of the repeat unit and their recombination produces a light crosslinking (or increase of the average molecular weight) of the chains. This could contribute to explain the increase of treated solution viscosity and of the mechanical properties observed on pre and pre&post treated electrospun PVdF separators. From the other side, the post-treatment promotes a light oxidation interesting mainly the aliphatic portion of the repeating unit that contributes to determine the increasing of the electrolyte uptake [123], [124].

5.3.11 Electrochemical impedance spectroscopy and MacMullin number

Pristine electrospun PVdF resistance was measured at 30°C by means of a conductivity meter (MeterLab CDM210 – Radiometer analytical). The membrane (10 mm diameter) was soaked in LP30 electrolyte and interposed between two stainless steel blocking electrodes, in a Swagelok-like cell. MacMullin number was calculated as ratio between the resistivity of the separator soaked in electrolyte and the resistivity of the electrolyte ($7.53*10^3$ Ohm*cm).

Electrospinning of PVdF led to sub-micrometric bead-free fibers with smooth fiber surface, resulting in 40–50 µm thick membranes. It is worth noting that thickness of electrospun separators is significantly higher than that of commercial separators (i.e. 25 µm), due to the different nature of the two materials. Indeed, conventional separator is a laminate, which can be realized in thin film, while electrospun membrane is a non-woven tissue made of several fibrous layers and requires higher thickness to avoid short-circuit. Experimental campaign on electrospun separators, not reported here for the sake of brevity, was carried out with the aim to optimize the thickness needed to prevent short circuits, i.e. 40–50 µm. However, the higher porosity and pore interconnectivity of electrospun membranes compared to Celgard (Figure 5.3) are expected to increase ionic conductivity and consequently decrease internal resistance of the cell, thus to better perform at high currents and in power-intensive applications. Indeed, MacMullin number measured on pristine electrospun PVdF was about 3 (see Table 5.6), while that of Celgard 2400 is reported to be about 16 [55]. An example of a transversal section of PVdF non-woven membrane is reported in the inset of Figure 5.3a. As can be seen, the path from the surface to the bottom of the membrane is characterized by a significant tortuosity, due to the randomly oriented pattern of fibers. Interconnected pores, even if large, do not cross directly the material, thus preventing short circuit if the membrane thickness is optimized.

Table 5.6 Impedance spectroscopy measurements on PVdF; resistance at intercept evaluated at 1 kHz in Nyquist diagram.

50 µm thick electrospun PVdF	**Resistance at the intercept [Ω*cm²]**	**Conductivity [S/cm]**	**Resistivity [Ω*cm]**	**MacMullin number**
Just assembled cell	3	$1.7*10^{-3}$	$5.9*10^{2}$	8
15 h at 30°C	1.3	$3.8*10^{-3}$	$2.6*10^{2}$	3
23 h at 30°C	1.1	$4.5*10^{-3}$	$2.2*10^{2}$	3
39 h at 30°C	1.2	$4.2*10^{-3}$	$2.4*10^{2}$	3
41 h at 30°C	1.3	$3.8*10^{-3}$	$2.6*10^{2}$	3
46 h at 30°C	1.1	$4.5*10^{-3}$	$2.4*10^{2}$	3

Ny-PVdF separator showed very low values of MacMullin number, as can be observed in Table 5.7. This finding is related to a very low contribution of the separator to the internal resistance of the cell.

Table 5.7 Impedance spectroscopy measurements on Ny-PVdF; resistance at intercept evaluated at 1 kHz in Nyquist diagram.

70 µm thick electrospun Ny-PVdF	**Conductivity [S/cm]**	**Resistivity [Ω*cm]**	**MacMullin number**
Just assembled cell	$7.28*10^{-3}$	$1.4*10^{2}$	1.8
15 h at 30°C	$7.96*10^{-3}$	$1.3*10^{2}$	1.7
41 h at 30°C	$9.8*10^{-3}$	$1.03*10^{2}$	1.4

5.3.12 Electrochemical stability and charge/discharge cycles

Pristine PVdF and PVdF loaded with 0.5 wt% SnO_2 were used in half cells vs. Li. Cell assembly was performed in a MBraun Labmaster SP glove box (water and oxygen content < 0.1 ppm). The membrane thickness (about 40–50 µm) was measured by a digital micrometer (Borletti MDE1, resolution

0.001 mm) that applies a compressive force between 8 N and 10 N. The nanofibrous membrane, soaked with 500 µL of LP30 electrolyte, was put on $LiFePO_4$ electrode and both placed in "Swagelok-like" electrochemical cells vs. Li in excess and Li reference electrode. $LiFePO_4$ electrode composition (in wt%) was 90% $LiFePO_4$ (Advanced Lithium Electrochemistry Co.), 5% Super P (Erachem) conductive carbon and 5% PVdF Kynar HSV 900 (Arkema). The electrodes had a LiFePO4 loading in the range of 5–7 mg/cm. The electrochemical tests were carried out by a Biologic VMP multichannel potentiostat/galvanostat at 30°C.

Cyclic voltammetries (CVs) were performed in LP30 at 1 mV/s in three-electrode configuration on glassy carbon (0.636 cm^2) as working electrode and Li as reference and counter electrode, at 30°C. The results are shown in Figure 5.21 and compared with those obtained with Whatman GF/D separator. The cells with the three separators perform almost identically. During the cathodic scan, it is first observed the reduction of the ethylene carbonate between 1.5 and 1.0 V vs. Li^+/Li, responsible of the formation of a surface passivation layer important in the case of a graphite anode, and the deposition of the lithium at lower potentials. Therefore, the cathodic currents are only related to the electrolyte and no evidence of the electroactivity of PVdF+0.5 wt% SnO_2 separator is recognizable.

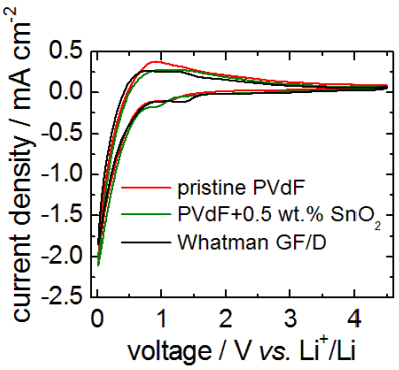

Figure 5.21 CVs at 1 mV/s in LP30 on glassy carbon electrodes between OCV (ca. 3.00 V vs. Li^+/Li) down to 0.02 V and, then, up to 4.50 V vs. Li^+/Li with pristine PVdF (red line), PVdF + 0.5 wt% SnO_2 (green line) and Whatman (black line) separators.

$LiFePO_4$ in half cells vs. Li with PVdF based separators were characterized by deep galvanostatic charge/discharge cycles.

Observing poor electrochemical performance of $LiFePO_4$ electrodes in half-cells vs Li., electrospun separators had been pressed, in order to increase adhesion and contact with the electrode. This procedure was carried out using a hydraulic press working at 400 psi for 15 min. Pressure value was chosen in order to preserve the fibrous nature of electrospun specimens. The aspect of a pressed separator is reported in Figure 5.22. For the sake of brevity, the comparison of the electrochemical characteristic of pressed and not pressed separators is reported only for cross-electrospun specimens, in Figure 5.23. It is worth noting that specific capacity at high C-rate, i.e. 1C, dramatically increased using pressed electrospun separators. Furthermore, this procedure permitted a significant increase in specimen handability. After these tests, pressed separators had been used for charge-discharge tests.

Figure 5.22 Electrospun separator after (left) and before (right) being pressed.

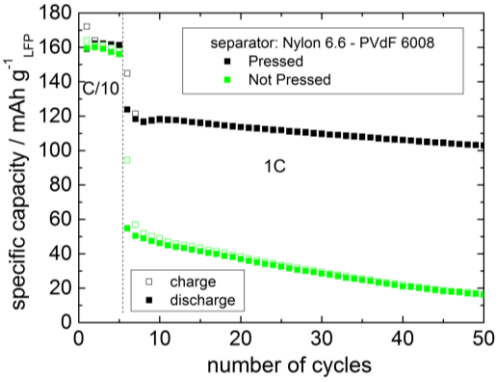

Figure 5.23 Comparison of the electrochemical performance of a $LiFePO_4$ electrode in half-cell vs. Li with not pressed cross-electrospun Ny-PVdF (green) and pressed cross-electrospun Ny-PVdF (black).

The voltage profile during the 1st charge/discharge cycle at C/10 between 2.5 and 4.2 V with PVdF+0.5 wt% SnO_2 separator, shown in Figure 5.24a, displays that the delivered capacity by LiFePO4 is very close to the theoretical value of 170 mAh/g. The discharge capacities at different C-rates (2 cycles for each discharge rate) of $LiFePO_4$ electrodes fully charged at C/10 in cells with PVdF (triangle) and with PVdF + 0.5 wt% SnO_2 (circle) separators are shown in Figure 5.24b and evince a good cycling performance for both cells.

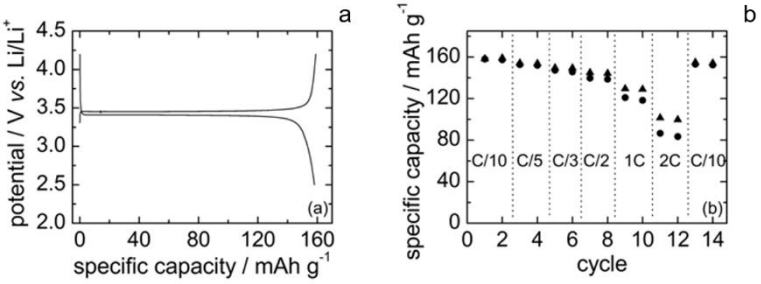

Figure 5.24 Charge/discharge voltage profile at C/10 of $LiFePO_4$ electrode in half cell vs. Li with PVdF + 0.5 wt% SnO_2 separator in LP30 (a); discharge capacities at different C-rates (2 cycles for each discharge rate) of $LiFePO_4$ electrodes fully charged at C/10 with PVdF (triangle) and PVdF + 0.5 wt% SnO_2 separators (circle) in LP30 (b).

A comparison between electrospun PVdF and commercial Whatman GF/D separators is reported in Figure 5.25. It is possible to highlight a better electrochemical performance of electrospun separator, due to higher specific capacity over all the tested C-rates. Specific capacity at high current (1 C) was about 15% higher than that of commercial separator.

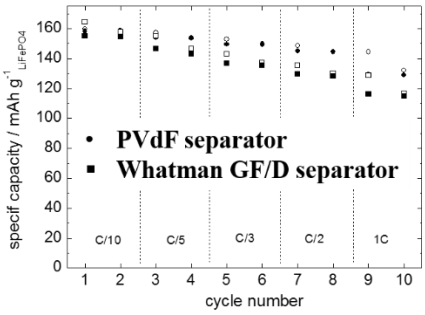

Figure 5.25 Charge (empty)-discharge (full) capacities at different C-rates (2 cycles for each discharge rate) of $LiFePO_4$ electrodes with electrospun PVdF (circle) and Whatman GF/D separators (square) in LP30.

5.3.13 Novel plasma assisted nanoparticle dispersion for LIB separators

Fumed silica nanoparticles (Sigma-Aldrich, average size = 7 nm) were added to the PEO solution in proper amount in order

to produce a final membrane containing 3% by weight of nanoadditive.

The plasma source used in this work was a single electrode plasma jet, described in [125]. Two separate gas inlets are used to control the production of reactive species; the primary gas is usually Ar, while O_2, N_2 or Air can be used as secondary gas. In this case, Ar was used as primary gas (flow rate = 2 slpm in all cases), while no secondary gas was used. The typical aspect of the plasma jet, working in the aforementioned conditions, is shown in Figure 5.26. The plasma source has been driven by a pulse generator producing high voltage pulses with a slew rate of few kV/ns, a peak voltage (PV) of 7-20 kV into a 100-200 Ω load impedance and a maximum pulse repetition rate (PRR) of 1000 Hz. The polymeric solution was exposed to the plasma source for different treatment times and under various operating conditions.

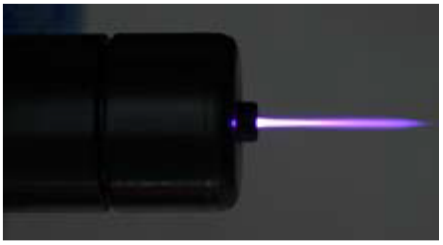

Figure 5.26 Picture of the plasma jet operated in Ar at flow rate 2 slpm, driven by the nanopulsed power generator, PRR 1000 Hz and PV 17 kV.

Different plasma treatments were applied to PEO solutions either before or after nanopaticle addition. A PEO solution not treated with plasma was loaded with fumed silica and electrospun to produce a control mat. All solutions were mechanically stirred after nanoparticle addition. If plasma treatment has been implemented after nanoparticle addition another stirring step has been done.

The effect of plasma treatment on particle aggregation in PEO solutions was evaluated by observing the distribution of

nanoadditive in the final electrospun fibers. Transmission electron microscope (TEM) analysis allows identifying the presence of particles inside and on the external surface of the fibers. Indeed, inorganic particles (black spots) in the organic matrix (grey background) may be recognized. Electrospun fibers, supported on conventional copper micro-grids, were observed by using a Philips CM 100 transmission electron microscope TEM operating at 60 kV in order to control the particle dispersion in the fibers.

Several steps reported in Table 5.8 composed every tested procedure. Mat electrospun starting from a solution prepared following protocol A was considered as a control for the comparison with all the other membranes. The other procedures consisted of different plasma treatments of polymeric solutions before or after nanoparticle addition. Plasma treatment #1 was carried out exposing the solution for 30 seconds to the plasma jet driven by a waveform with PRR = 500 Hz and PV = 22 kV. Plasma treatment #2 was performed exposing the solution for 3 minutes to the plasma jet driven by a waveform with PRR = 1000 Hz and PV = 27 kV.

Table 5.8 Experimental procedures. The letters A-E indicate different treatment protocols.

	Step 1	**Step2**	**Step 3**	**Step 4**
A	Nanoparticles addition	10 minutes stirring	-	-
B	Plasma treatment #1	Nanoparticles addition	10 minutes stirring	-
C	Plasma treatment #2	Nanoparticles addition	10 minutes stirring	-
D	Nanoparticles addition	10 minutes stirring	Plasma treatment #1	10 minutes stirring
E	Nanoparticles addition	10 minutes stirring	Plasma treatment #2	10 minutes stirring

Electrospun fibers produced from differently plasma treated PEO solutions containing nanosilica appeared morphologically similar in the SEM observations reported in Figure 5.27. Image analysis of the fibers electrospun starting from both the plasma-exposed and the control solutions did not show the presence of defects. Indeed, good quality fibers without beads have been collected with all the procedures.

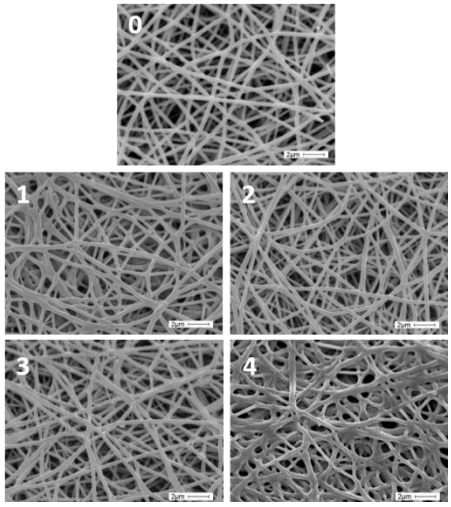

Figure 5.27 SEM images of the electrospun nanofibers loaded with 3% of fumed silica: protocol A (0); protocol B (1), protocol C (2), protocol D (3), protocol E (4). Scale bar = 2 μm.

TEM images highlighted the differences in silica distribution inside the fibers, as a consequence of the different procedures applied. Indeed, control fiber (i.e. obtained from a non-treated solution) contained silica aggregates, demonstrating that mechanical stirring is not sufficient for a homogeneous nanoadditive dispersion. Indeed, as shown in Figure 5.28, black aggregates are localized in a very narrow area, while the remaining part of the fiber does not present any additive.

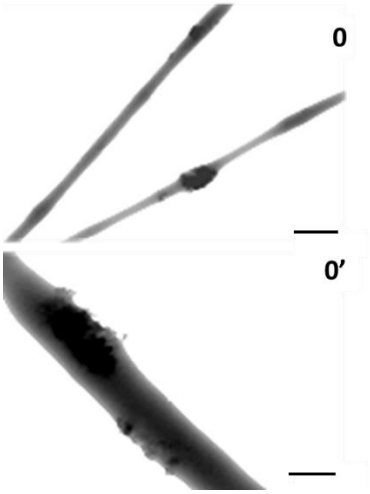

Figure 5.28 Fibers electrospun following protocol A. Fiber containing aggregates (0), scale bar = 500 nm; electrospun fiber containing aggregates (0'), scale bar = 200 nm.

The exposure of PEO solutions to plasma improved the homogeneity of particle distribution in the final fibers, as can be noted comparing Figure 5.28 with Figure 5.29, Figure 5.30, Figure 5.31 and Figure 5.32. The best result in terms of particle dispersion was obtained by exposing PEO solution to plasma before silica addition, using the following operating conditions: PRR = 1000 Hz, PV = 27 kV and treatment time = 3 minutes (Figure 5.30). Indeed, nanoparticles are disseminated homogeneously inside the fiber, as black spots distribution highlights.

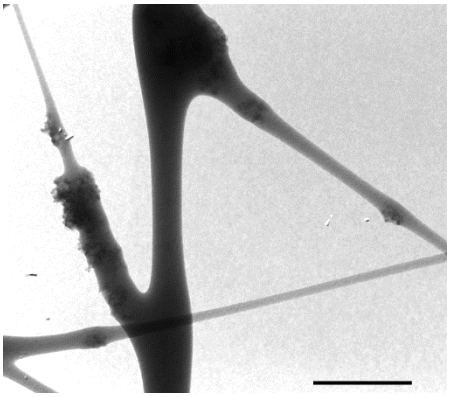

Figure 5.29 Fibers electrospun following protocol B: solution exposed to plasma (PRR = 500 Hz, PV = 22 kV, treatment time = 30 seconds) before nanoparticle addition. Scale bar = 500 nm.

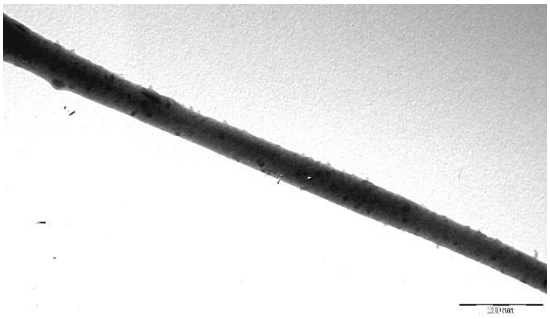

Figure 5.30 Fibers electrospun following protocol C: solution exposed to plasma (PRR = 1000 Hz, PV = 27 kV, treatment time = 3 minutes) before nanoparticle addition. Scale bar = 200 nm.

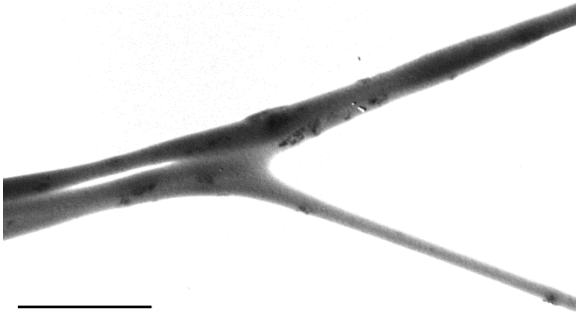

Figure 5.31 Fibers electrospun following protocol D: solution exposed to plasma (PRR = 500 Hz, PV = 22 kV, treatment time = 30 seconds) after nanoparticle addition. Scale bar = 1 µm.

Figure 5.32 Fibers electrospun following protocol E: solution exposed to plasma (PRR = 1000 Hz, PV = 27 kV, treatment time = 3 minutes) after nanoparticle addition. Scale bar = 1 µm.

Polymeric solutions have been exposed to different plasma driven by two combinations of operating conditions, i.e. plasma treatment #1 (for protocol B and D) and plasma treatment #2 (for protocol C and E): differences in particle distribution inside the electrospun fibers could be evaluated comparing Figure 5.29 with Figure 5.30 and Figure 5.31 with Figure 5.32.

Comparing mats obtained from plasma treated solutions, a better nanofiller distribution has been achieved increasing PV, PRR and the treatment time during the plasma treatment. Particle aggregates have been found in the fibers (Figure 5.29 and Figure 5.31) even if areas not presenting nanoadditives are smaller than in the control. In some aggregates can be detected even if a large amount of nanoparticles is dispersed along fibers length, unlike in the control mat. Comparing fibers obtained using the protocol C and E the first one, where there is no detection of aggregates, can be identified as the best procedure to improve nanoparticle dispersion.

Chapter 6
Experimental campaign on electrospun ferroelectret materials

6.1 Electrospun mats manufacturing

The experimental campaign has been mainly carried out using PVdF-TrFE copolymer, due to its aforementioned property of crystallize in the electroactive ß phase. PVdF 6008 was tested in order to highlight the difference between PVdF homopolymer and copolymer.

PVdF-TrFE Solvene (25% mol TrFE, 75% mol VDF, Mw = 410 kDa) was kindly provided by Solvay Specialty Polymers and was dissolved at a concentration of 15% w/v in Acetone (Ac):Dimethyl sulfoxide (DMSO) (70:30, v/v). PVdF 6008 was realized as mentioned in Separator manufacturing section.

The experimental apparatus used to manufacture electrospun ferroelectrets has been previously described in Separator manufacturing section (section 5.1) and it has not reported here for the sake of brevity. Electrospinning operating conditions are reported in Table 6.1.

Table 6.1 Electrospinning operating conditions for PVdF-TrFE

Flow rate [ml/h]	1
Needle-to-collector distance [cm]	17.5
Voltage bias [kV]	20
Temperature [°C]	25
Relative humidity [%]	21

Finally, a commercial piezoelectric film of PVdF (Goodfellow), about 500 μm thick, was tested after silver ink metallization. In addition, other films realized by solvent casting, about 60 μm thick, were poled after poly(3,4-ethylenedioxythiophene) (PEDOT) electrode deposition and were also tested.

6.2 Material characterization

After morphological analysis, different mechanical stimuli were applied to the material in order to study its electrical response. Therefore, several characterizations were carried out and the main results are summarized in the following sections.

It is important to highlight that only direct piezoelectric effect has been investigated, aiming at studying the electrical behavior of these materials. This led to the study of sensors or energy harvesters, rather than actuators.

Electrospun piezoelectric samples were sandwiched between aluminum-foil electrodes for each electromechanical test, as reported in Figure 6.1 .

Figure 6.1 Example of tested sample: Electrodes (1, 2), electrospun piezoelectric sample (3); the dotted line surrounds the active area of the specimen.

6.2.1 Scanning electron microscope

Fiber morphology was evaluated through the same apparatus used for separator characterization. Good quality fibers without defects were successfully electrospun. Both random and aligned fiber patterns were produced. Aligned fibers were created using a high-speed rotating drum collector. Random fibers (Figure 6.2) showed average diameters of about 820±100 nm, while aligned fibers (Figure 6.3) of about 720±100 nm.

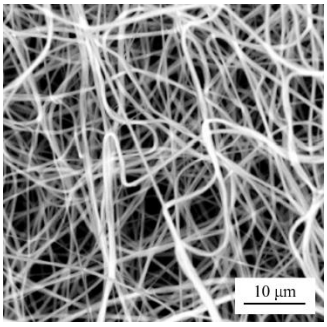

Figure 6.2 SEM image of electrospun PVdF-TrFE with random fibers.

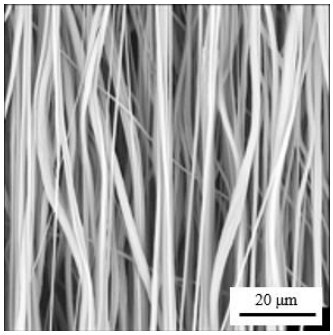

Figure 6.3 SEM image of electrospun PVdF-TrFE with aligned fibers.

6.2.2 X-ray spectroscopy

X-ray diffraction (XRD) spectroscopy was implemented to detect crystalline phases of the PVdF. X-ray diffraction patterns were obtained with CuK_{α} radiation in reflection mode by means of an X'Pert PANalytical diffractometer equipped with a fast X'Celerator detector, step 0.1°, 150s /step.

Figure 6.4 shows the XRD spectra of the nanofibrous PVdF-TrFe specimen and PVdF commercial film. As can be seen, both materials show evidences of ß-phase, which is indicated by the peak around 20°. The commercial PVdF film, however, exhibits also α-phase, which has not piezoelectric behavior, corresponding to the peaks at 17.5° and 26° [126]. It is worth noting that these peaks are absent in the electrospun nanofibrous specimen, indicating that ß-phase is much larger than that shown by the commercial film. This feature will positively affect also the piezoelectric behavior of the two materials, as will be shown in the following.

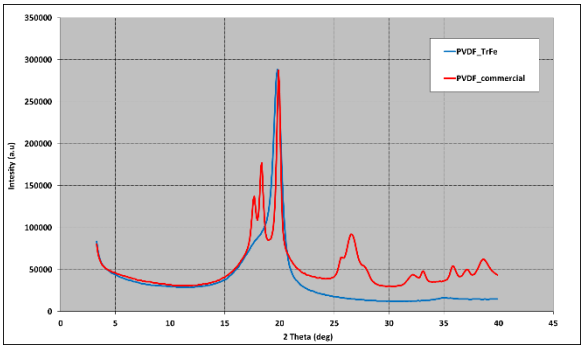

Figure 6.4 XRD spectra of electrospun PVdF-TrFe and commercial PVdF film.

Figure 6.5 shows the XRD spectra of the nanofibrous PVdF-TrFe samples. The polymer exhibits α-phase, which is claimed to show weak piezoelectric behavior, corresponding to the peak at 17.5°. Furthermore, the polymer shows evidences of β-phase, detected by the peak around 20°. In particular, PVdF-TrFe having aligned fibers shows a lower content of α-phase with respect to random fibers. Indeed, peak intensity associated to α-phase decreases in the sample having aligned fibers. This behavior is directly linked to the stretching force, provided by the high-speed rotating drum collector, on the polymer chains spun during the electrospinning process. Such force provided a partial transformation from α-phase to β-phase, thus leading to enhanced piezoelectric behavior.

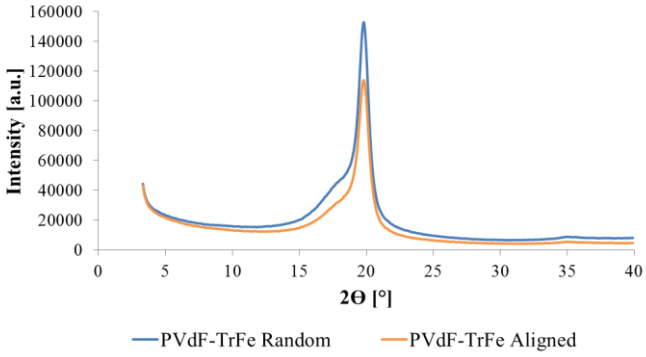

Figure 6.5 XRD spectra of electrospun PVdF-TrFE: comparison between random and aligned fiber pattern.

6.2.3 Repetitive impact electrical response

Piezoelectric samples of 30 x 40 mm^2 were subjected to repetitive mechanical impulses given at different frequencies, ranging from 0.5 Hz to 5 Hz, through an electromagnetic piston (10 mm diameter), controlled with National Instruments LabVIEW™. Two different masses were connected to the system thus the total weight of the piston was 350 g and 500 g, respectively. Every test was carried out acquiring at least ten signals at each frequency for any weight. Aluminum foils deposited on the electrospun specimen surfaces were used as electrodes and connected to a digital oscilloscope (Tektronix DPO 5034) in order to detect and record the electric signals generated by mechanical impulses. The experimental apparatus is sketched in Figure 6.6.

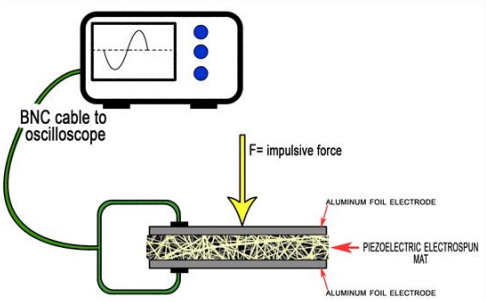

Figure 6.6 Experimental apparatus of the electro-mechanical tests carried out on electrospun samples.

Highly reproducible waveforms were detected from the impulsive mechanical tests, as can be observed in Figure 6.7, which displays the electrical response to 350 g stress at 4 Hz for PVdF 6008 and PVdF-TrFe. From waveform analysis, peak-to-peak voltage spectra can be also obtained as shown in Figure 6.8 and Figure 6.9 for PVdF-TrFe and PVdF 6008, respectively. Since all the samples tested in this work provided voltage signals having large amplitude, i.e. in the Volt range, the use of an amplifier to process the signal could be avoided. Looking at Figure 6.8 and Figure 6.9, it can be clearly observed that electrical signals related to PVdF-TrFe samples are significantly larger than those relevant to PVdF 6008. This behavior can be explained considering that PVdF 6008 is a homopolymer having almost linear chains while PVdF-TrFe is a co-polymer, specifically designed to enhance piezoelectric behavior, due to a higher content of polar ß-phase. The electric response with frequency of PVdF-TrFe shows that the higher the frequency, the larger the peak-to-peak voltage detected. On the contrary, PVdF 6008 shows that voltage signal increases, as the frequency rises, up to a given value, beyond which a sudden decrease is observed. This behavior could be explained considering that the co-polymer, having a structure characterized by highly polar branch chains, is able to provide good piezoelectric response at higher frequencies with respect to PVdF 6008. It is worth noting that for the 500 g mechanical

stress on PVdF 6008 the piezoelectric response saturates at frequencies larger than 2 Hz. For the 350 g mechanical stress an increasing trend is seen up to 4 Hz, beyond which the signal drops. It can be speculated that for 350 g mechanical stress, saturation phenomenon could likely occur at a higher frequency, exceeding the range here investigated [127].

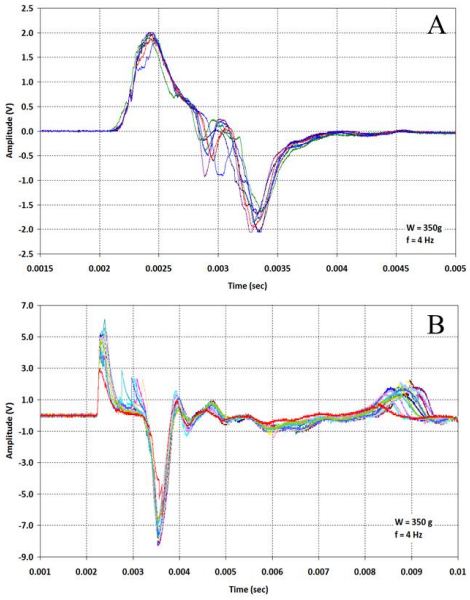

Figure 6.7 Plots reporting overlapped waveforms obtained from repetitive tests carried out under a stress of 350 g at 4 Hz on electrospun PVdF 6008 (A) and PVdF-TrFe (B).

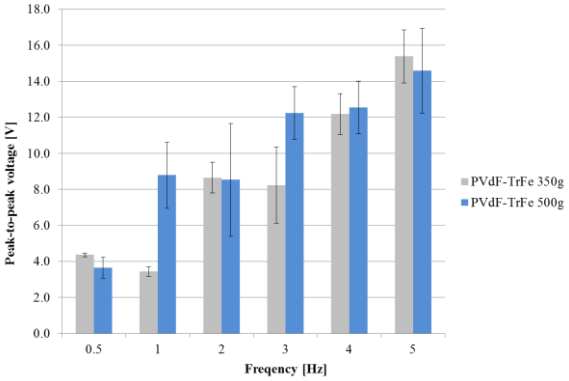

Figure 6.8 Voltage response (peak-to-peak value) of electrospun PVdF-TrFe as a function of frequency.

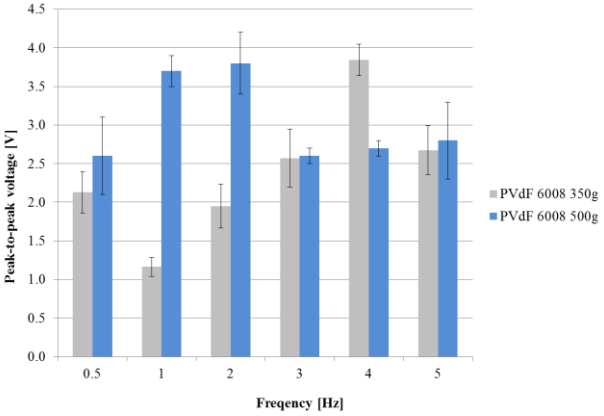

Figure 6.9 Voltage response (peak-to-peak value) of electrospun PVdF 6008 as a function of frequency.

In order to assess the effect of repetitive mechanical stress on material conditions, SEM images of PVdF-TrFe after several impacts given by the electromagnetic piston (500 g) are reported in Figure 6.10. In particular, Figure 6.10A displays a large specimen region showing two different zones, one clearly affected by mechanical stress and another one where the typical fibrous structure is still present. Zooming in the impact zone (Figure 6.10B), it is evident that the typical fibrous pattern of electrospun mats radically changes into a film-type structure. Indeed, repeated impacts applied to the fibrous material press

the mat, reducing the air gaps between fibers and, consequently, compacting the fibrous sample into a less porous material. In general, such phenomenon is not a symptom of material degradation, since electric response may remain quite large also for higher impact rate (see Figure 6.8), but affects permanently sample morphology, thus modifying piezoelectric signals obtained after several mechanical impulses. Nevertheless, sometimes a significant degradation of the material is observed after several impacts, particularly in thinner specimens, leading to electrode short-circuiting in short times. This can explain also the large confidence intervals shown in Figure 6.8 and Figure 6.9. It has to be pointed out, however, that particularly harsh mechanical stress conditions have been here used to investigate piezoelectric behavior. With the aim of using these nanofibrous specimens as impact sensors or in energy storage applications, permanent changes in the polymer morphology should be avoided, applying lower mechanical stresses to piezoelectric fibers.

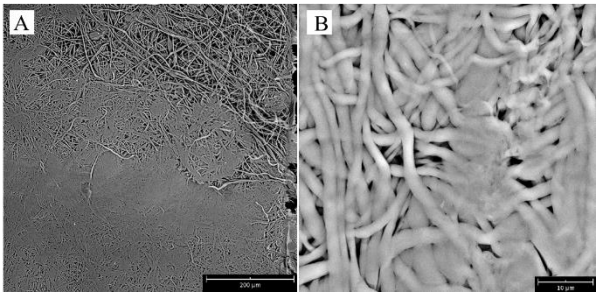

Figure 6.10 SEM image of electrospun PVdF-TrFe after several mechanical impulses generated by the piston: transition from fiber-like to film-like structure (A) and detail of impact zone (B); scale bar = 200 μm (A) and 10 μm (B).

A commercial PVdF film was tested with the aim of comparing voltage response to that of electrospun mats. Results are summarized in Table 6.2, which reports a selected frequency of testing, i.e. 2 Hz. It is possible to highlight that the response of commercial piezoelectric is larger than that of

electrospun PVdF 6008, in particular at 500 g stress. The contrary, electrospun PVdF-TrFe shows values of peak-to-peak voltage much higher than commercial PVdF, i.e. about four times greater. This behavior can be explained considering that the piezoelectric effect is associated also with the so-called "domain wall motion" [101]. In this case, nanofibrous nature of electrospun material allows larger mobility of domain walls, leading to higher piezoelectric responses with respect to film materials. Furthermore, the most interesting issue coming from the experimental results is that a so large piezoelectric effect is obtained from a fibrous sample constituted of about 80-90% vol. of air. Considering the measured average weight of an electrospun specimen and of a commercial PVdF film as about 30 mg and 1 g, respectively, the values of average specific piezoelectric response (in V/g) are reported in Table 6.3. It can be highlighted that specific response of electrospun PVdF is 1-2 orders of magnitude larger than commercial PVdF. These findings could allow sensors and/or harvesters having very low weight to be manufactured for high energy density applications.

Table 6.2 Voltage response of electrospun samples and commercial PVdF film stressed with 350 g and 500 g at 2 Hz.

Sample	**Piezoelectric response (peak-to-peak) [V]**	
	350 g	**500 g**
Commercial PVdF film	1.4 ± 0.4	2.3 ± 0.5
Electrospun PVdF 6008	2.0 ± 0.3	3.8 ± 0.4
Electrospun PVdF-TrFe	8.7 ± 0.9	8.5 ± 3.1

Table 6.3 Specific voltage response of electrospun samples and commercial PVdF film stressed with 350 g at 2 Hz.

Sample	**Specific piezoelectric response [V/g]**
Commercial PVdF film	1.4
Electrospun PVdF 6008	67
Electrospun PVdF-TrFe	290

6.2.4 Electric response under vibrations

The aforementioned samples were subjected to mechanical vibrations given by a metallic piston (15 mm diameter) connected to a vibration shaker (The Modal Shop, model K2110E-HT). Such vibration shaker was driven by a sinusoidal waveform at different frequencies, ranging from 30 Hz to 200 Hz. The magnitude of the shaker peak-to-peak displacement (d) is a function of frequency (f) and acceleration (G), according to the following equation provided by the supplier:

$$\mathrm{d} = 496.82 * \frac{G}{f^2} \qquad (6.1)$$

In order to avoid any material damage, a Poly(methyl methacrylate) (PMMA) plate (thickness = 2 mm), which allows good mechanical wave propagation, was placed between the sample and the piston. Every test was carried out acquiring five signals at each frequency and for different accelerations of the vibration shaker: from 1G to 8G, detected through an accelerometer. The specimens were connected through a BNC cable to a digital oscilloscope (Tektronix DPO 5034), in order to detect and record the electric signals generated by mechanical vibrations. A picture of the experimental apparatus is reported in Figure 6.11.

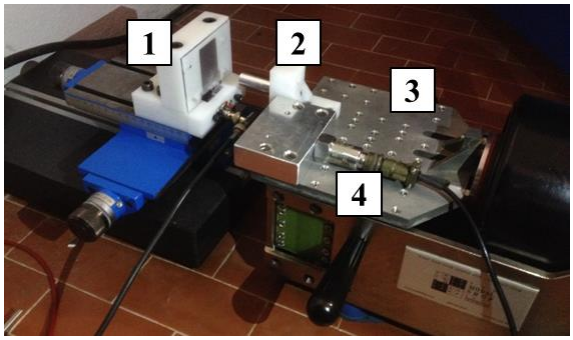

Figure 6.11 Experimental apparatus of the electro-mechanical tests carried out on electrospun samples composed of: sample holder (1), piston (2), vibration shaker (3), and accelerometer (4).

By way of example, waveforms at 50 Hz and 100 Hz at 5G of PVdF-TrFe film and electrospun PVdF-TrFe having random and aligned fibers are reported in Figure 6.12 and Figure 6.13, respectively. All samples displays signals having the same frequency of the mechanical stress. It is worth noting that the electrical response to mechanical stimulus of PVdF-TrFe having aligned fibers has very low rise and fall times, providing very fast impulses. Furthermore, there is no delay between the electric response and the mechanical stress, with respect to the random sample, which have a remarkable phase shift. PVdF-TrFe film shows no delay too, but at a frequency of 100 Hz a sequence of repetitive impulses having different amplitude is detectable, i.e. one peak having higher amplitude followed by a lower peak, both positive and negative. Moreover, such behavior can be observed also for PVdF-TrFe random. This phenomenon can be associated to a slow relaxation mechanism for both materials, as can be observed in Figure 6.13A and Figure 6.13B. Indeed, signal fall times are much longer than those of aligned PVdF-TrFe samples, thus providing a slower response. Therefore, at high frequency electrical response to a further mechanical impulse could be affected by a previous impact.

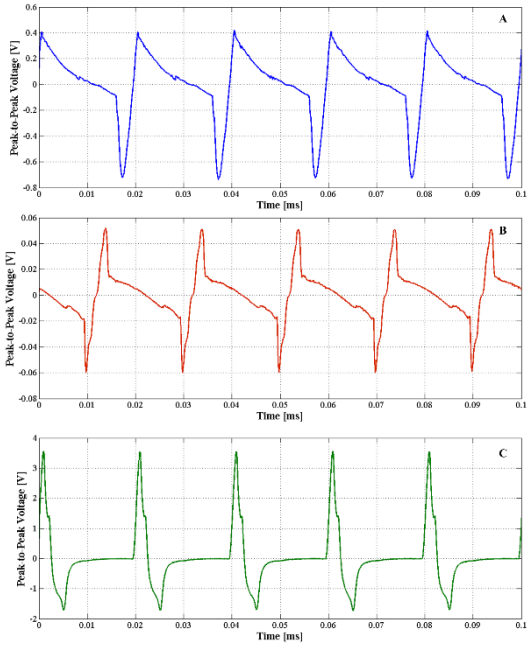

Figure 6.12 Waveform comparison between PVdF-TrFe film (A) and electrospun PVdF-TrFe having random (B) and aligned fibers (C) at 50 Hz and 5G.

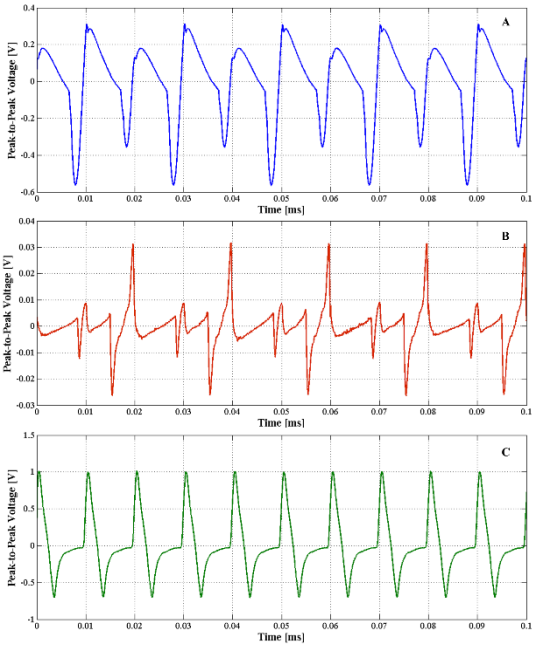

Figure 6.13 Waveform comparison between PVdF-TrFe film (A) and electrospun PVdF-TrFe having random (B) and aligned fibers (C) at 100 Hz and 5G.

Figure 6.14 shows the comparison between the electric signals generated by the three types of piezoelectric materials when subjected to several accelerations at 4 frequencies: 30 Hz, 50 Hz, 100 Hz and 200 Hz. Random fibers show signals much lower than those of PVdF-TrFe film, while aligned fibers exhibit a larger electric response with respect to the other materials. This behavior can be associated to the aforementioned XRD results, which confirmed the beneficial effect of the stretching of the polymer chains caused by the high-speed rotating drum. It is possible to observe that bulk material displays a lower rate of increase of V_{pp} with G, at a fixed frequency, with respect to electrospun mats. This can be explained by mat morphology which have higher fiber mobility due to its lower stiffness. Indeed, the high surface-to-volume ratio of nanofibrous materials is claimed to be the most important advantage of such electrospun structures, with respect to films. Furthermore, as

G increases, mechanical stress causes a reduction of sample thickness and porosity of the membrane. This temporary effect may increase electrical permittivity of the mat, leading to a higher piezoelectric coefficient. In the range of tested frequencies, no saturation effect is detected [128].

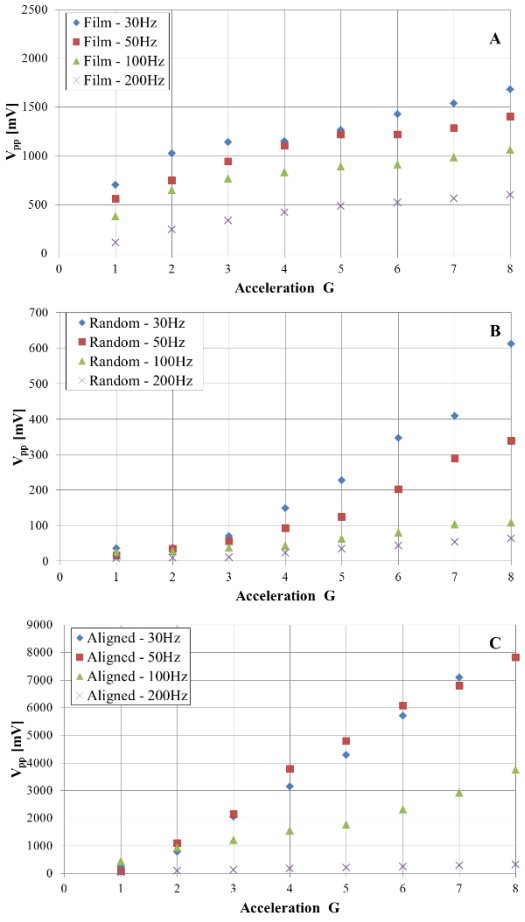

Figure 6.14 Acceleration dependence of peak-to-peak voltage response at different frequencies of PVdF-TrFe film (A), PVdF-TrFe having random fibers (B) and PVdF-TrFe having aligned fibers (C).

Finally, all the samples have been tested with air gap between the PMMA slab and the vibrating piston, in order to detect the acoustic waveform generated by the vibrating

system. The test was carried out with a gap of 1 mm and 1.5 mm. Results show that samples detected sinusoidal waveforms at the same frequency of the mechanical vibration. Magnitude of such signals decreases with the air gap increase, for all the three material type. By way of example, results at 100 Hz and 5G are summarized in Table 6.4. Hence, the feasibility to realize acoustic devices using electrospun mats has been proved.

Table 6.4 Acoustic response of PVdF-TrFE

Air gap [mm]	**V_{pp} [mV]**		
	Film	**Random fibers**	**Aligned fibers**
1	61±1	40±3	72±2
1.5	50±1	22±2	53±3

6.2.5 Electric response to drop weight tests

A drop weight apparatus was realized in order to test the electrical response of electrospun materials, when subjected to a mechanical impulse generated by a mass falling on the sample. A picture of the system is reported in Figure 6.15. The metallic mass of 12 mm diameter falls by 40 cm height. A polycarbonate (PC) tube of 15 mm diameter, through which the mass of 4 g falls on the sample, is vertically placed on the specimen that is sandwiched between two aluminum-covered polymethyl methacrylate (PMMA) electrodes. A BNC connector permits to plot and analyze voltage waveforms on an oscilloscope.

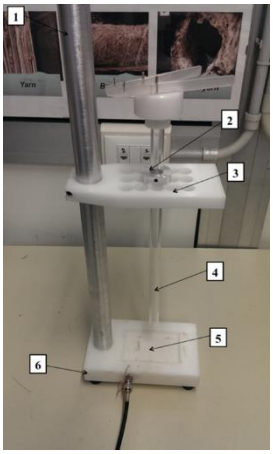

Figure 6.15 Drop weight apparatus: (1) support cylinder, (2) block system, (3) perforated plate, (4) PC tube, (5) sample compartment, (6) anti-shock base plate.

The aim of this experiment was to characterize the piezoelectric response of electrospun PVdF-TrFE membranes through a series of 15 impacts occurred in different regions of the samples. Specimen geometry is shown in Figure 6.16.

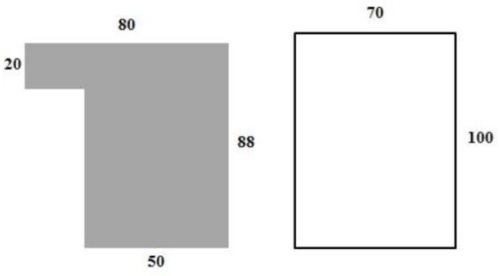

Figure 6.16 Electrode (left) and sample (right) geometry expressed in millimeters.

Typical piezoelectric waveform generated by a PVdF-TrFE film is reported in Figure 6.17. Analyzing several impacts on the same sample, triboelectric effect between the material and the aluminum electrode was detected (see Figure 6.18). Indeed, it is possible to observe a contribution to the electric signal preceding the piezoelectric response. The same behavior was

observed for electrospun samples, as reported in Figure 6.19 and Figure 6.20. Moreover, electrospun specimen waveforms show only one polarity. This polarity differs from random and aligned fibers. This behavior can be ascribed to electret effect and triboelectric effect and therefore to a different relative motion between sample and electrodes. In particular, signal polarity depends on which electrode moves towards the sample. Another evidence of a different phenomenon from a pure piezoelectric effect can be highlighted comparing waveforms relevant to film specimens (Figure 6.17) and electrospun materials (Figure 6.19 and Figure 6.20). Indeed, waveform fall time of a film is much smaller than that of electrospun samples.

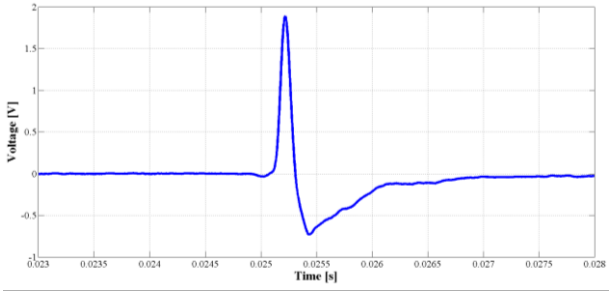

Figure 6.17 Example of waveform obtained on PVdF-TrFE film.

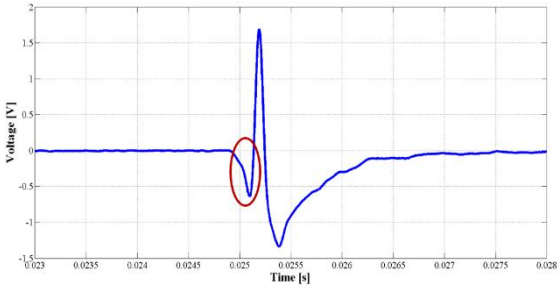

Figure 6.18 Influence of triboelectric effect on PVdF-TrFE film waveform, highlighted in red.

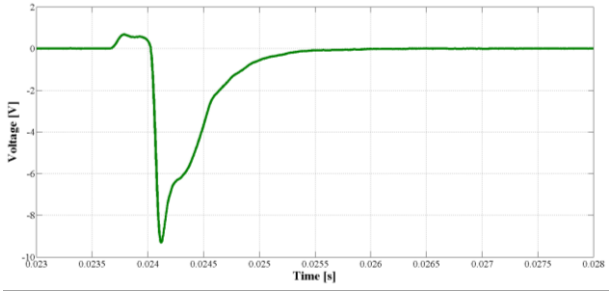

Figure 6.19 Example of waveform measured on PVdF-TrFE random.

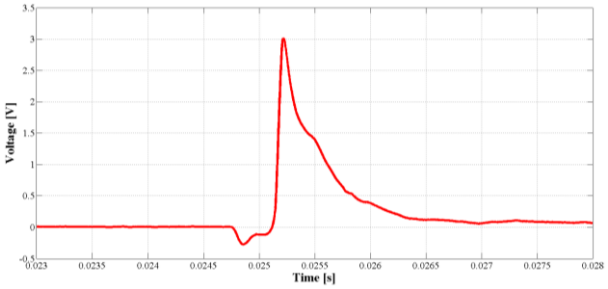

Figure 6.20 Example of waveform detected on PVdF-TrFE aligned specimen.

Three different samples (P1, P2 and P3) of random electrospun PVdF-TrFE were tested on both sides: side A (the side on which the last fibers were spun) and side B (the side on which the first fibers were spun). The analysis of voltage waveforms is reported in Figure 6.21. It is possible to observe that signal polarity does not change when sample is reversed. This behavior could suggest that electrospun membranes do not show any piezoelectric effect. Even supposing that the piezoelectric behavior exists due to electrical poling of ß-phase during the electrospinning process, the electrical signal detected could be ascribed also to electret behavior and triboelectric effect related to PVdF-electrode contact. Furthermore, the amplitude of the piezoelectric response could be smaller than that generated by the other contributes. Moreover, another evidence of these phenomena can be found in the low measurement repeatability of electric signals, which

showed large amplitude of confidence intervals. If a significant contribution to the electric signal was due to electret effect, this effect could be intrinsically not homogeneous. Indeed, the charge trapped during electrospinning process can be non-homogeneously distributed in the sample [81], particularly in the case of randomly spun fibers. In the same way, triboelectric effect strongly depends on surface roughness, contact extension, ambient condition, etc., which are typically factors difficult to keep under control [110].

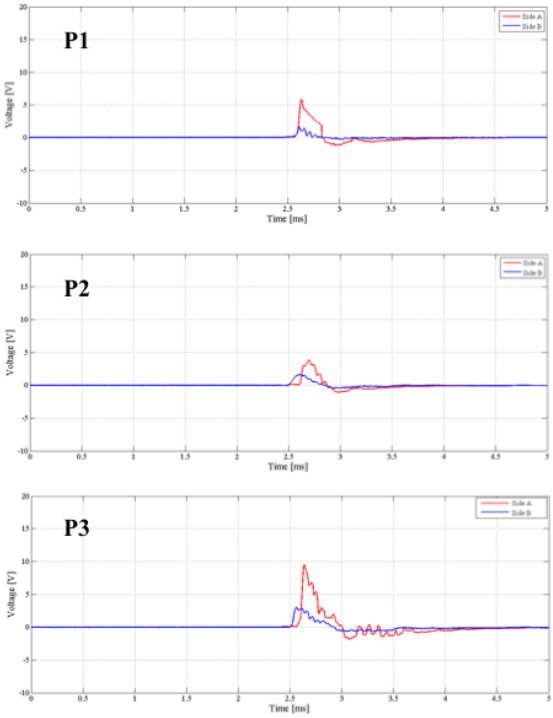

Figure 6.21 Voltage waveforms of three different electrospun PVdF-TrFE samples obtained by impacts on side A (red) and side B (blue).

Therefore, the existence of different electrical phenomena, i.e. piezoelectric, triboelectric and electret effects, requires a deep study of the charge trapped in the electrospun ferroelectrets, as will be discussed in the following sections.

6.2.6 Space charge measurements by means of pulsed electroacoustic (PEA) method

Space charge trapped in electrospun PVdF-TrFE ferroelectrets was evaluated through the pulsed electroacoustic (PEA) technique. The technique, described by Dissado et al. [129], is based on the application of a voltage pulse, superimposed on a much higher continuously applied DC voltage to the sample. This causes an electromechanical stimulus on space charge which generates an acoustic waveform detected by means of a piezoelectric sensor, located under the ground electrode. Waveform profile is proportional to the net space charge located in the insulation bulk. Moreover, the delay time between the electric signal and the voltage pulse application gives the space charge location along the insulation thickness, since the acoustic pulse travels at the known speed of sound in the material [129]. Therefore, time length of the recorded signal corresponds to material thickness. The experimental apparatus has a spatial resolution of about 10-20 μm.

A schematic of the experimental apparatus is reported in Figure 6.22. Test cell was equipped with an 8 mm diameter semi-conductive disc installed on the upper electrode, where the high voltage (HV) is applied. Specimens were tested placing the samples in contact with the HV electrode and with the ground aluminum electrode.

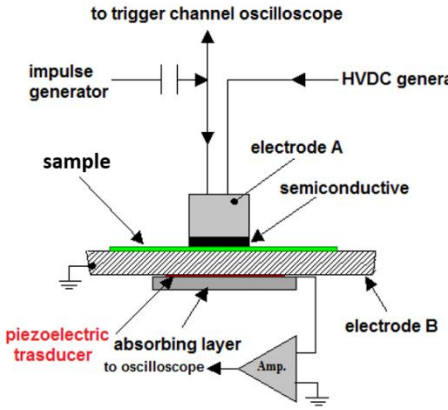

Figure 6.22 Schematic of PEA method experimental setup.

A 8 kV/mm electric field (positive voltage) and a voltage pulse of 300 V and 10 ns duration were applied at room temperature to unpoled film (34 µm thick), poled film (65 µm thick) and electrospun mat (150 µm thick). PEA signals are reported in Figure 6.23, Figure 6.24 and Figure 6.25, respectively. Analyzing unpoled film signal Figure 6.23, as expected, very small amount of space charge was detected before voltage application. At the end of the depolarization phase, a similar amount of charge is still present in the material. This charge is probably surface charge associated to triboelectric effect, since it cannot be injected by the electrodes, due to the low applied electric field, i.e. 8 kV/mm. Considering 2370 m/s as sound speed in PVdF-TrFE, it was possible to detect each voltage peak associated to electrodes, i.e. HV and ground. Anode and cathode are highlighted through vertical bars in the following figures (Figure 6.23B, Figure 6.24B and Figure 6.25B), respectively.

Analyzing poled films (Figure 6.24), polarization associated to dipole alignment experiences polarity inversion when the specimen is reversed (results not reported for the sake of brevity). Moreover, signal detected did not change during voltage transient. It can be hypothesized that the applied

electric field was lower than that associated to material dipoles. It should be observed that this low field was chosen in order to compare film and electrospun materials, since porous electrospun structures have poor dielectric strength being mainly made of air. Considering the aforementioned sound speed, it was possible again to detect each voltage peak associated to electrodes.

Analyzing PEA signals of electrospun samples (Figure 6.25) it was difficult to clearly identify electrode positions, even if sample thickness was known. This behavior is due to the presence of several air-polymer and polymer-polymer interfaces in electrospun specimens. This drawback also affects the choice of the correct speed sound in electrospun PVdF-TrFE. Since fibrous materials can be identified as soundproof structures, PEA method has some limitation for non-wovens. Moreover, the high capacitance of electrospun samples, of the same order of magnitude of the coupling capacitance of pulse generator, causes a distortion of voltage pulse and a consequent decrease of PEA spatial resolution. However, the most important information could be the presence of charge of both polarity inside the material. Indeed, Figure 6.25 shows that during the poling stage (voltage on phase) voltage peak associated to anode and cathode, highlighted through vertical bars in Figure 6.25, increased at the same level (i.e. compare Figure 6.25A with Figure 6.25B). Moreover, negative and positive charge increased close to cathode and anode, respectively, due to charge injection. At the end of the depolarization phase (voltage off phase), it is possible to observe bipolar charge accumulation in the material (compare Figure 6.25A with Figure 6.25F).

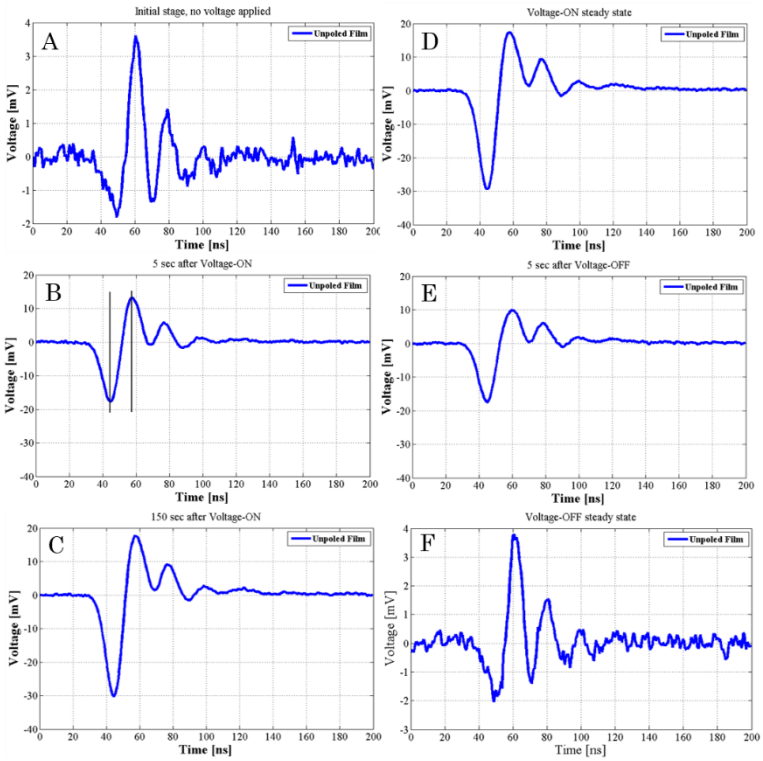

Figure 6.23 PEA signal evolution of unpoled PVdF-TrFE film: initial stage (no voltage applied) (A), 5 s after voltage on (B), 150 s after voltage on (C), voltage on steady stage (D), 5 s after voltage off (E) and voltage off steady state (F).

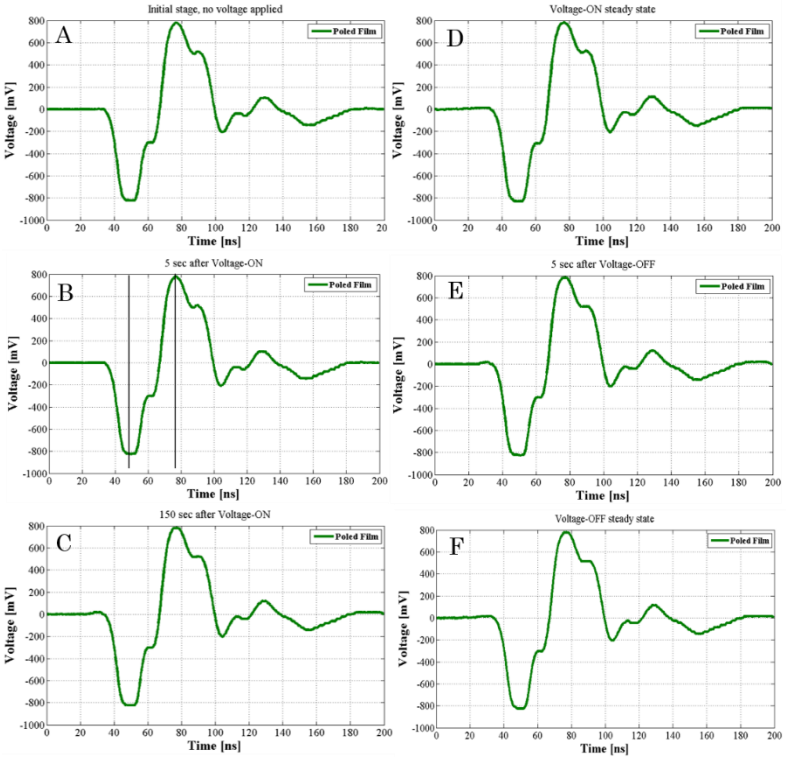

Figure 6.24 PEA signal evolution of poled PVdF-TrFE film: initial stage (no voltage applied) (A), 5 s after voltage on (B), 150 s after voltage on (C), voltage on steady stage (D), 5 s after voltage off (E) and voltage off steady state (F).

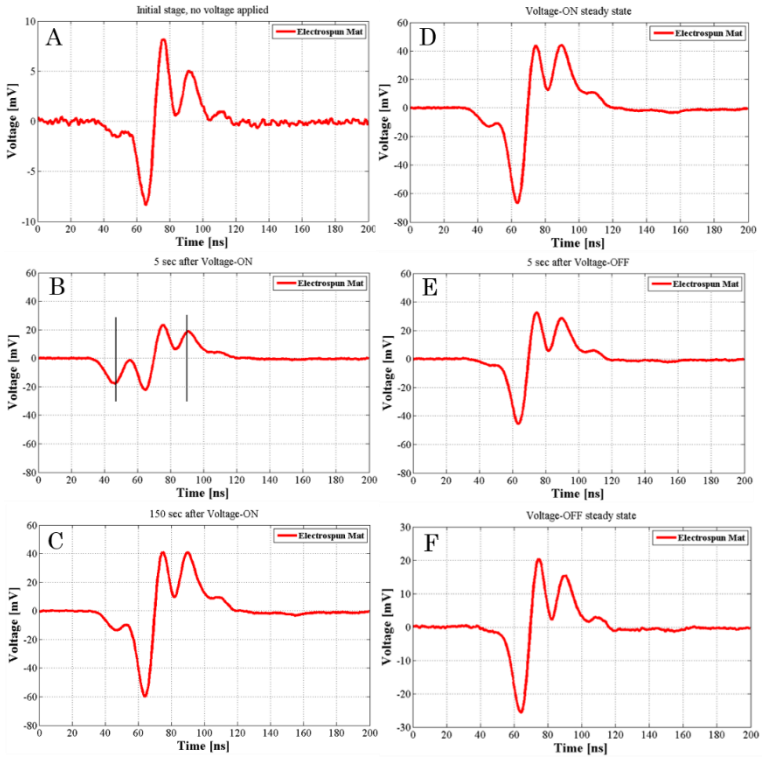

Figure 6.25 PEA signal evolution of electrospun PVdF-TrFE specimen: initial stage (no voltage applied) (A), 5 s after voltage on (B), 150 s after voltage on (C), voltage on steady stage (D), 5 s after voltage off (E) and voltage off steady state (F).

Analyzing further PEA signals of 100 µm electrospun PVdF-TrFE samples, tested on both membrane sides at 4 kV/mm, it is possible to highlight that the specimen contain a larger amount of negative charge than positive. This phenomenon can be observed comparing the PEA signal at the end of the polarization phase, acquired applying positive or negative voltage to the sample and reported in Figure 6.26. It must be noticed that: (i) the ground electrode shows negative charge when positive voltage is applied to the sample; (ii) the low resolution of PEA system results in overlapping of surface charge and/or trapped charge in the bulk close to the electrode with image charge, during polarization phase. Differences in

the peak position along specimen thickness and amplitude between positive (red) and negative (blue) applied voltage confirm that the material is strongly negatively charged. It is worth noting that side B of the material shows a larger amount of negative charge if compared to side A. This can be associated to the fact that side A is the mat side on which the last fibers were spun and this can lead to the presence of a lower content of trapped charge in the material. It can be concluded that fluorinated polymer strongly attracts negative charges.

As a further confirmation, a specimen electrospun using negative polarity voltage (-20 kV) and the same other operating conditions seems to retain even more negative charge (see Figure 6.27). This behavior is probably due to a higher amount of negative charges generated by negative corona discharges at the needle tip and in the surroundings of Taylor cone and trapped in the polymer.

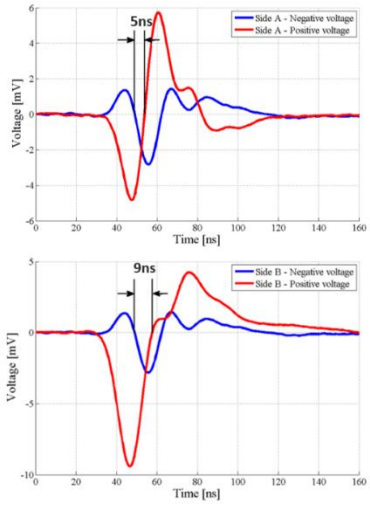

Figure 6.26 PEA signal, at the end of poling stage, of both sides of PVdF-TrFE electrospun using positive voltage.

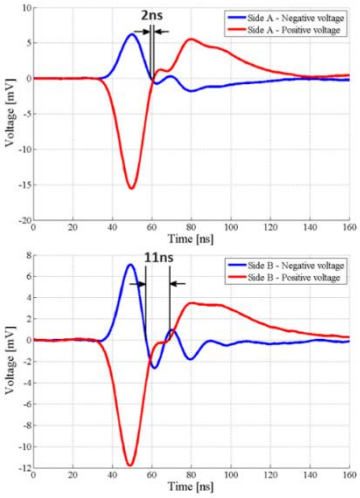

Figure 6.27 PEA signal, at the end of poling stage, of both sides of PVdF-TrFE electrospun using negative voltage.

Different types of specimens were tested in order to overcome the abovementioned PEA method limitations for electrospun materials. In particular, trying to reduce the porosity (air content), electrospun mats were pressed at different pressures, ranging from 5 bar to 20 bar, and the PEA signals were compared to that relevant to a non-pressed membrane. Such specimens were tested at 6 kV/mm using a 100 V pulse with 10 ns duration. The relevant PEA signals are reported in Figure 6.28. It can be noted that detected signal shape is not influenced by pressure. Again, voltage peak associated to HV electrode is not easily detectable, even if mat porosity is smaller. It is worth noting that reducing air content in the mat the amount of negative charge increases, likely due to the increase of specimen capacitance.

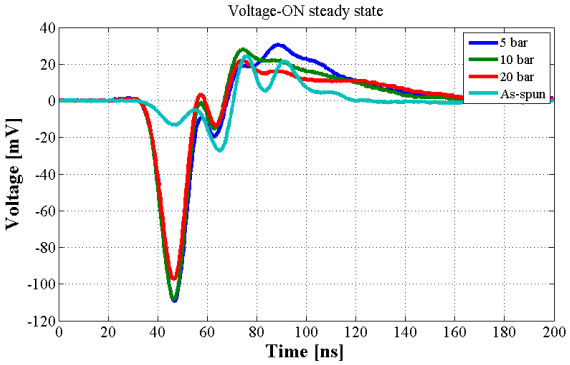

Figure 6.28 PEA signal, at the end of poling stage, of pressed electrospun PVdF-TrFE mats.

Finally, a thicker specimen was investigated in order to match better with the spatial resolution of the used PEA apparatus. For this purpose, five layers of electrospun mats were pressed together at 10 bar obtaining a 275 µm thick specimen. The overall capacitance is smaller: electrical permittivity increases due to porosity reduction, but thickness increase is dominant. In this case, this less porous and thicker specimen allowed the electric field to be increased up to 18 kV/mm. Both positive and negative voltage were applied to the sample (see Figure 6.29). As can be highlighted in Figure 6.29, electric field increase does not seem to have any influence on waveform shape, except on the first peak magnitude. It has to be emphasized that voltage peak associated to HV electrode still is hard to be detected, probably due to soundproof properties of electrospun textiles. Furthermore, trapped charge of both polarities can be observed.

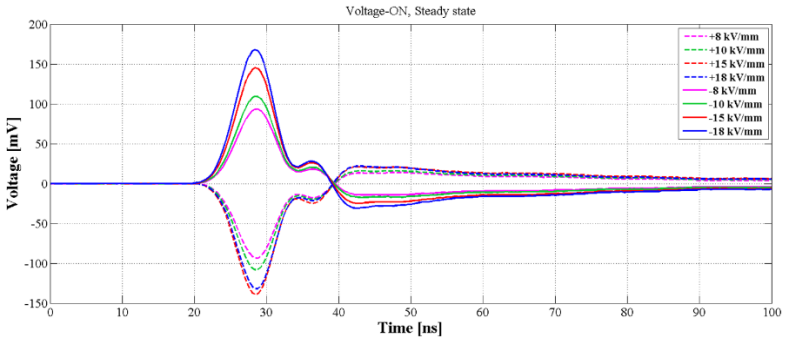

Figure 6.29 PEA signal, at the end of poling stage, of 5 layers of electrospun PVdF-TrFE pressed at 10 bar and tested at different electric fields of both polarities: ±8, ±10, ±15 and ±18 kV/mm.

6.2.7 Impact study through high-speed imaging

A high-speed camera Memrecam NAC GX-3 was used to study the dynamics of mechanical impacts on PVdF-TrFE samples. Impacts were carried out using the drop-weight apparatus described before. In addition to the metallic sphere, test using a metallic cylinder of about 20 g were also carried out. Acquisition rate was kept at 24000 frame per second (fps). Moreover, camera trigger was synchronized with oscilloscope trigger. This study was carried out in order to distinguish the triboelectric effect in the detected signal, since it is related to the relative movement of electrode and sample. Impact time was highlighted through two vertical black bars in the acquired images. Indeed, using the aforementioned fps value it is not possible to detect the exact frame of the impact, but only identify the time interval of the impact.

The typical piezoelectric waveform of film material is shown in Figure 6.30. The piezoelectric response occurs just after the contact time of the sphere. Image of sphere falling before and during the impact on the material is reported in Figure 6.31.

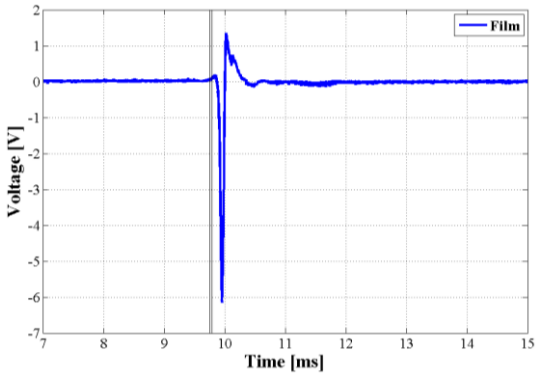

Figure 6.30 Poled PVdF-TrFE film waveform.

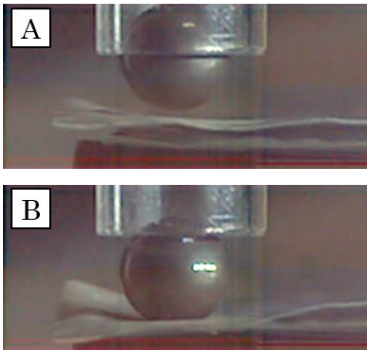

Figure 6.31 Sphere falling before the impact on poled PVdF-TrFE film (A) and sphere impact on the sample (B).

As expected, the unpoled film does not show any piezoelectric behavior, see Figure 6.32. In this case, the measured waveform can be associated only to triboelectric effect caused by relative motions between electrodes and film after the impact.

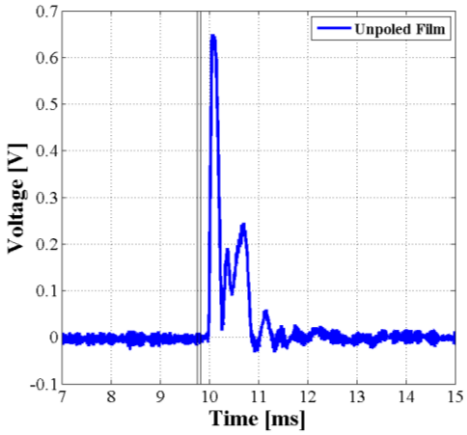

Figure 6.32 Unpoled PVdF-TrFE film waveform.

In case of electrospun sample, the specimen was intentionally kept separated from the upper electrode, in order to highlight the presence of triboelectric phenomenon, as shown in Figure 6.33. Analyzing the waveform detected in this case (see Figure 6.34), it is possible to highlight that the first part of the waveform is in advance with respect to the impact. Therefore, this part of the signal can be ascribed to the triboelectric effect, while the electrode approaches to the sample.

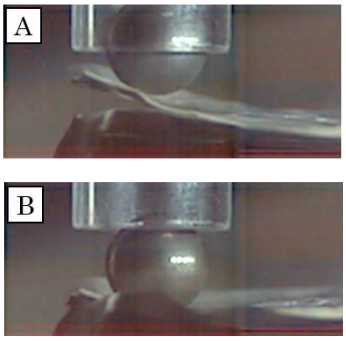

Figure 6.33 Falling sphere in contact with electrode (A) and with electrospun sample (B).

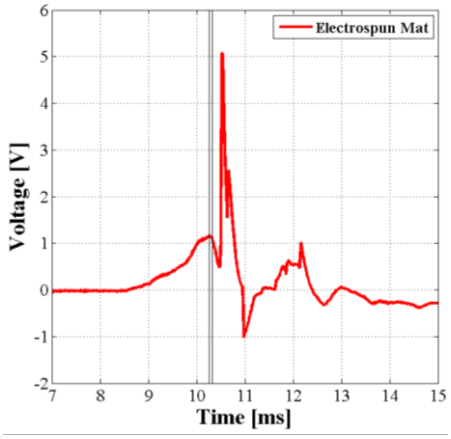

Figure 6.34 Waveform associated to sphere impact on electrospun PVdF-TrFE.

A similar behavior can be observed also using a cylinder as impact tool as can be seen in Figure 6.35 that shows the gap between electrode and electrospun sample, before the impact. The blue line in Figure 6.36, which displays the detected signal, represents the time of Figure 6.35A. The electric signal associated to triboelectric effect is thus comprised between the blue line and the first black line of Figure 6.36. It is evident that the amplitude of triboelectric signal is much lower than the other part of the electric signal. As expected, the amplitude strongly depends on the gap size between electrode and sample. Moreover, waveform detected after the impact on the material is different if compared to film signal (see Figure 6.30). In addition, it is worth noting that waveform time length of electrospun samples is larger than that relevant to film material.

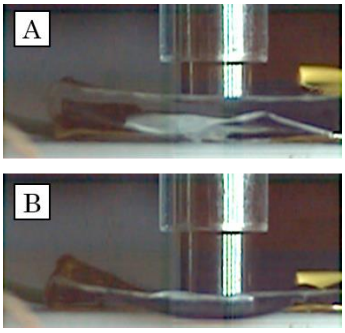

Figure 6.35 Cylinder impact on electrospun PVdF-TrFE.

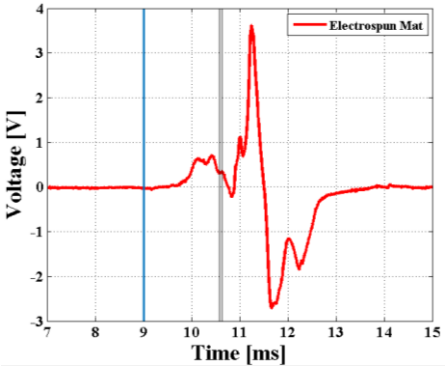

Figure 6.36 Waveform associated to cylinder impact on electrospun PVdF-TrFE.

Triboelectric effect was then intentionally minimized firstly reducing relative material motion between electrodes and electrospun mat, e.g. bonding the sample and the electrodes. Waveform associated to sphere impact on this sample is reported in Figure 6.37. The absence of the triboelectric contribution is clear. Moreover, electrospun sample was metallized on the surface, to avoid any relative motion between electrode and specimen. Again, any triboelectric effect cannot be observed, as can be seen in Figure 6.38. However, a signal of single polarity is detectable, suggesting a dominant contribution of the electret effect on the piezoelectric.

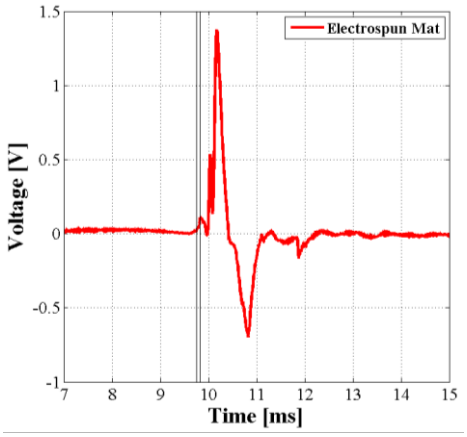

Figure 6.37 Waveform associated to sphere impact on bonded electrospun PVdF-TrFE.

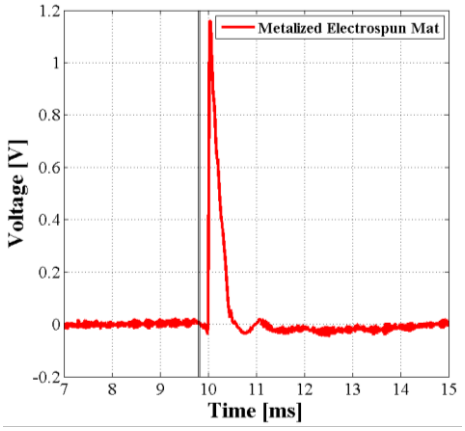

Figure 6.38 Waveform associated to sphere impact on metalized electrospun PVdF-TrFE.

Finally, it is very important to highlight that not only single polarity waveforms or peaks of both polarities were detected, as shown in Figure 6.39. Indeed, it is possible to observe the presence of two peaks that can be associated both to the piezoelectric and to the electret effects.

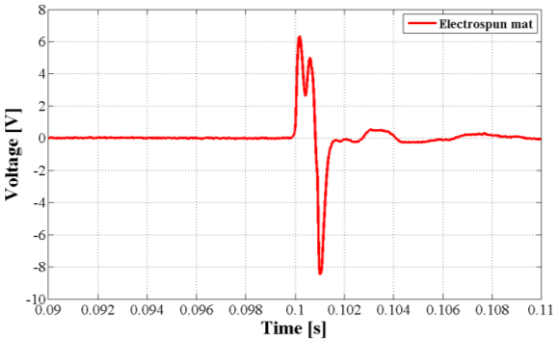

Figure 6.39 Waveform associated to sphere impact on electrospun PVdF-TrFE.

Chapter 7
Discussion about experimental results

7.1 Electrospun separators

Plasma assisted nanoparticle dispersion

The improvement of polymer properties through good nanoparticle dispersion can ensure the realization of high-performance materials, e.g. battery separators, showing enhenced or novel properties. Usually, mechanical or ultrasonic treatments are implemented as conventional methods to disaggregate nanoparticle clusters in fluids. In this work, a novel plasma treatment based on a different physical mechanism, i.e. through the activation of ionic and electrostatic interactions between the polymer and the nanoadditive, has been presented. This method has been compared to the typical mechanical stirring of nanoparticles inside polymeric solution. It was demonstrated that plasma treatment is a valuable means to favor nanoparticle dispersion in polymeric solutions, since electrospun fibers produced from these solutions displayed a better particle dispersion with respect to the ones produced from untreated solution. Indeed, TEM images highlighted remarkable differences in particle distribution inside the fibers and SEM images did not show any morphological modification due to plasma application.

The aforementioned described plasma assisted procedure could represent a promising way to disperse nanofillers in polymer solutions. It is worth noting that this dispersion technique is general. Indeed, besides electrospinning and separators for Lithium-ion batteries, this technique can be applied to realize any kind of solid nanocomposites through different procedures, e.g. solvent casting, sol-gel, melt-blending, and for different application fields.

Plasma assisted electrolyte uptake improvement

The effect of pre-treatment of a PVdF electrospinning solution and post-treatment of PVdF electrospun separators on the electrolyte uptake has been here presented for the first time. The exposure to the plasma source was carried out aiming at increasing the amount of liquid electrolyte absorption of the separator. This feature can lead to higher ionic conductivity of the cell.

Plasma pre-treatment of the PVdF electrospinning solution caused an increase of the solution viscosity and a light crosslinking (or increase of the average molecular weight) of the chains, leading to the improvement of electrospinnability and enabling the production of defect-free nanofibers. Indeed, SEM images highlighted good quality nanofibers without beads, while fibers electrospun from an untreated solution displayed a large number of defects. Moreover, an improvement of mechanical properties has been achieved thanks to a better fiber morphology compared to control PVdF. Electrolyte uptake of pre-treated samples significantly increased compared to control electrospun mats, due to the achievement of a better fiber morphology.

The use of a nanosecond-pulsed DBD for mat post-treatment did not affect thermal properties of the separator, neither fiber morphology. Moreover, the treatment significantly increased the electrolyte uptake, due to a chemical modification induced

on the PVdF surface, improving the polymer electrolyte affinity. Indeed, XPS analysis highlighted the presence of oxygen on the surface, due to O-C=O and -CF2-CH-(OH) groups, inducing an increase of the electrolyte uptake [123], [124].

The post-treatment of PVdF separators electrospun starting from a pre-treated polymeric solution enabled the increase of the electrolyte uptake up to 1200%, about ten times higher than the uptake of commercial Celgard separators [130], [131]. This result highlights a synergistic effect of plasma pre-treatment and plasma post-treatment, leading to a dramatically increase of electrolyte uptake of electrospun separators. It could be possible to achieve a breakthrough in power-intensive applications of these cells thanks to this important feature and very low internal resistance of LIBs with electrospun separators.

Finally, a remarkable improvement in electrospun separator handability was achieved thanks to plasma pre-treatment of polymeric solution. This behavior is very important in order to simplify battery assembly operations and to prevent possible short-circuits.

Nanofilled electrospun separators

PVdF electrospun separators loaded with inorganic nanoparticles of SiO_2 and SnO_2 were successfully produced by electrospinning. The addition of nanoparticles mainly affects PVdF mat mechanical properties. SiO_2 tends to increase the toughness of the separator while SnO_2 tends to increase its stiffness, thus improving PVdF mechanical properties and making it more suitable to resist to battery assembly procedures. This achievement represents a fundamental requirement in order to develop electrospun separators for the market.

Furthermore, it has been demonstrated that even a low amount of nanoparticles significantly affect electrolyte uptake. Indeed, fumed SiO_2 enhances the rate of electrolyte uptake while SnO_2 slightly decreases it with respect to pristine PVdF membrane, probably due to the high polarity of SiO_2. As a matter of fact, all the investigated electrospun membranes display a remarkable higher electrolyte uptake than commercial separator. This property leads to high ionic conductivity and excellent Li^+ ion transport, thus increasing the rate capability of the battery.

It is important to highlight that silicon and tin are active materials that can be used as electrodes in LIBs. For this reason, electrical conductivity of separators filled with oxides of these elements was investigated, in order to study possible reduction of the oxides at the electrode. No evidence of this phenomenon was observed, since electronic conductivity was much lower than 10^{-8} S/m, thus nanofilled separators could be considered good insulating materials. Moreover, the addition of nanoparticles decreases the activation energy for electronic conduction, thus improving the insulating properties of the membranes at high temperatures and providing a safer behavior in case of overheating.

Cross-electrospun separators

The possibility to manufacture electrospun separators having mechanical properties suitable for industrial scale up has been investigated through a novel process. The use of a sustain polymer to increase stress-at-break of PVdF electrospun separators has been studied for the first time. This proof of concept can be further studied in order to achieve the best result in terms of mechanical properties and electrochemical performance, exploring the use of different polymers.

The most important feature of this novel technique is the possibility to avoid safety issue related to the use of toxic or hazardous nanoadditives. It is worth noting that cross-electrospinning is indeed a cost effective technique that does not need the use of expensive additives.

Comparison of electrochemical cycling performance

Electrochemical results of several charge-discharge cycles at 1C using different separators are shown in Figure 7.1. The comparison highlighted that cross-electrospun separators exhibited the lowest specific capacity. This behavior can be related to the presence of Nylon, which could not be the best polymer in terms of electrochemical affinity with the used electrolyte (i.e. LP30). Moreover, plasma pre-treated separators showed an increase of specific capacity if compared to pristine PVdF. This improvement has been achieved thanks to the increased ionic conductivity. However, specific capacity at high C-rate obtained using electrospun separators is slightly lower than that relevant to Whatman separator. Battery assembly improvement and pressing stage optimization represent some of the possible strategies to increase electrochemical performance of electrospun materials.

Future experiments will be also carried out on pre&post-treated electrospun separators, in order to exploit the synergistic effect of plasma pre-treatment and plasma post-treatment observed on electrolyte uptake.

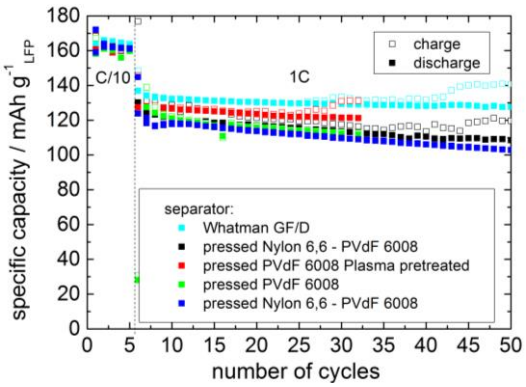

Figure 7.1 Comparison of electrochemical performance of a $LiFePO_4$ electrode in half-cell vs. Li with different separators: Whatman GF/D (azure), pre-treated PVdF 6008 (red), PVdF 6008 (green) and cross-electrospun Ny-PVdF (blue).

Electrochemical performance of electrospun separators showed promising results in terms of specific capacity when compared to commercial separators, e.g. Whatman fiberglass. In particular, the use of nanofilled separators, e.g. tin oxide nanoadditive, slightly decreased specific capacity (see Figure 5.24 and Figure 5.25), but the use of nanofiller is mandatory for an industrial scale up of this technology. Furthermore, good stability of specific capacity at different C-rates and good capacity recovery at low C-rate, i.e. C/10, after discharge capability represent interesting features of nanofilled separators.

7.2 Ferroelectrets

The feasibility to manufacture electrospun piezoelectric materials has been investigated. Most of literature papers claim that the presence of PVdF ß-phase and an electric response to a mechanical stress indicate that PVdF-based electrospun materials are piezoelectrics, as reported before. This study has demonstrated that the behavior of electrospun materials is much more complex, due to the existence of the electret and triboelectric effect. From the analysis of voltage waveforms of

electrospun samples, it is evident that electret effect and triboelectric effect are dominant in terms of waveform shape and electret effect also in terms of voltage amplitude. In general, only reversing a supposed piezoelectric sample and keeping the same voltmetric connection it is possible to detect if the signal is effectively generated by a piezoelectric effect, as highlighted in Figure 7.2A and Figure 7.2C. Most of the waveforms collected from electrospun ferroelectrets did not show any polarity inversion. This suggested the existence of other contribution to the material response.

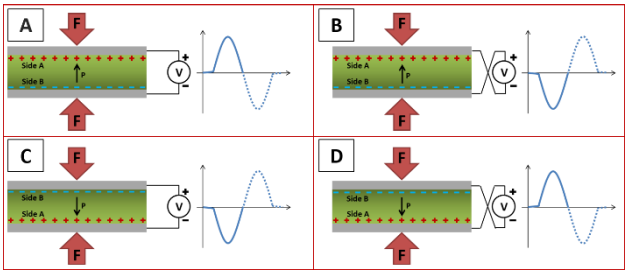

Figure 7.2 Electric signal generated by a piezoelectric material subjected to a compressive force: material side A connected to the voltmeter positive electrode (A), material side A connected to the voltmeter negative electrode (B), material side B connected to the voltmeter positive electrode (C), material side B connected to the voltmeter negative electrode (D).

In particular, PVdF-based electrospun mats attract electrons when they came in contact with electropositive materials, due to the high electronegativity of fluorine atoms in the molecular chain. Indeed, fluoropolymers have the ability to become negatively charged during contact with other materials, both insulating or metals according with triboelectric series. The relative motion of the upper electrode generate a charge flow in the external circuit caused by the variation of the electrostatic charges induced in the electrodes, as outlined in Figure 7.3. This figure describes the relative motion after the first contact between the materials. Indeed, in the original state no electrical potential exists between the top electrode and nanofibers while they are separated and they have not been in contact yet. When

they come in contact, the surfaces of the electrode and PVdF nanofibers are charged with the same surface density. Then, when a pressing force is applied to the top electrode, a voltage bias drives the electrons towards the top electrode flowing through the external circuit, which produces the observed current. Fluoropolymers become always negatively charged on the surface that comes in contact with the electrode (the top electrode in this case). For this reason, no difference in waveform polarity is observed when the specimen is reversed, keeping the same voltmetric connections.

This behavior leads to electrostatic surface charge that strongly affects the electric signal of the material. Indeed, surface roughness and fiber mobility of nanofibrous structures can generate random electric response.

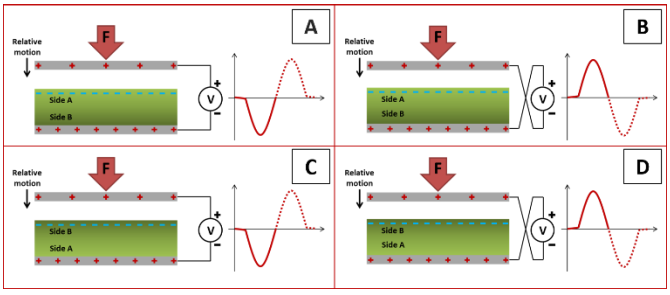

Figure 7.3 Electric signal generated by triboelectric effect when a fluorinated polymer is subjected to a compressive force: material side A connected to the voltmeter positive electrode (A), material side A connected to the voltmeter negative electrode (B), material side B connected to the voltmeter positive electrode (C), material side B connected to the voltmeter negative electrode (D).

Moreover, charge trapped in electrospun mats represent another source of electric response of the material. The mechanism of charge retain in electrospinning is reported in Figure 7.4. In particular, charge injection during polymeric solution electrification and corona poling of the polymeric jet during electrospinning can affect significantly the electric response. Charge injection from the metallic needle to the

polymeric solution is due to the high electric field applied between the needle and the grounded collector. Corona discharges (see Figure 7.5) occurring at the needle tip and in the surroundings of Taylor cone represent another source of charge generation in the polymeric jet. Although charge removal occurs due to solvent evaporation, presence of humidity in the ambient and charge transfer to the collector, electrospun fibers still retain charge [106].

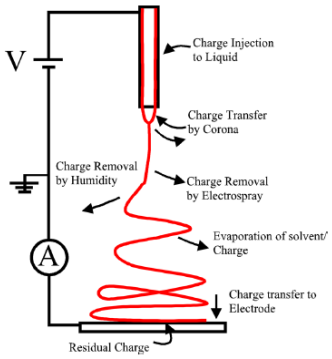

Figure 7.4 Charge generation, injection and retain during electrospinning [106].

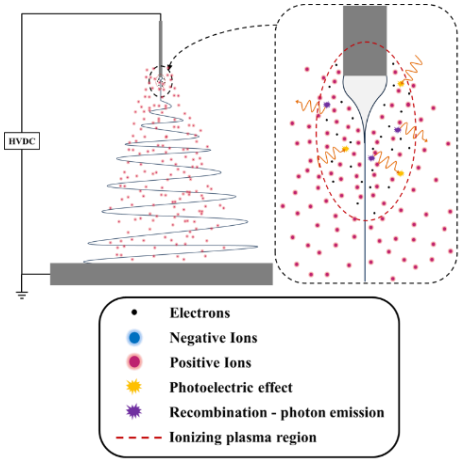

Figure 7.5 Positive corona poling during electrospinning carried out with positive HVDC.

The evidence of charge trapped in electrospun PVdF-TrFE was highlighted through PEA method measurements reported in Section 6.2.6. In particular, charge of both polarity was detected, due to charge injection during electrification and corona discharge phenomena. Moreover, surface charge neutralization did not affect the aforementioned measurement, strengthening space charge existence in electrospun samples that leads to electret behavior.

Figure 7.6 and Figure 7.7 show the typical behavior of an electret having a uniform charge Q_i. The electret is an electrostatic converter based on a capacitive structure composed by the electret and the electrodes. The electret induces charges on electrodes and Q_i has then to be equal to the sum of Q_1 and Q_2. Q_1 is the amount of charges on the electrode and Q_2 the amount of charges on the counter-electrode. A relative movement of the counter-electrode towards the electret induces a change in the capacitor geometry. Indeed, the air gap changes and then the electret influence on the counter-electrode. This leads to a reorganization of charges through the load R, e.g. oscilloscope impedance, resulting in a current

circulation through R and a portion of the mechanical energy, associated with the relative movement, is turned into electric energy [132].

The relationship between voltage and capacitance in an electret is reported in Equation 7.1:

$$V = \frac{Q}{C(t)} + \mathrm{R}\frac{dQ}{dt} \qquad (7.1)$$

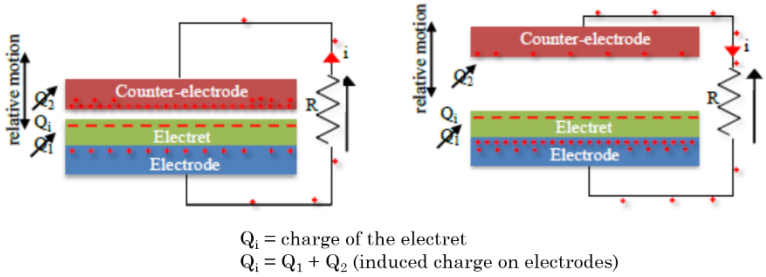

Figure 7.6 Electret-based charge induction scheme [132].

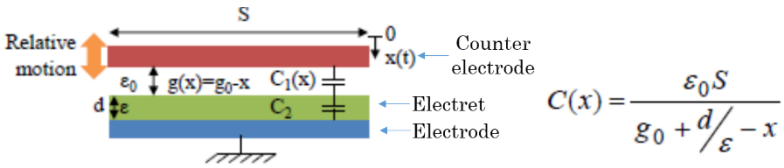

Figure 7.7 Capacitance variation of an electret during counter-electrode motion [132].

This capacitance variation is dramatically enhanced in electrospun porous structures, due to the sponge-like deformation that temporarily decreases the air content in the material during the mechanical stress. The capacitance variation is associated to a change in electrical permittivity, due to a smaller amount of air in the compressed electrospun mat.

Furthermore, fiber mobility of electrospun materials induces several relative movements between the electret and the other electrode during mechanical stress, thus leading to a more complex waveform output of the compressed material, as

previously reported in the experimental section. Both electret and triboelectric phenomena can contribute to this modification. Finally, it is not possible to assume that electrospun materials have uniformly distributed charge, due to the random electrical and fluid dynamics that take place during whipping instability. This leads to another cause of waveform distortion from the conventional electret output.

Finally, from high-speed camera test it was possible to distinguish the triboelectric contribution to the detected signal. Indeed, an electrical signal was detected before the impact and from the high-speed images it was possible to relate it to the electrode approach to the electrospun mat. It is possible to speculate that the waveform detected after impact on electrospun samples can represent the sum of piezoelectric and electret contribution. When electret contribution is dominant on piezoelectric effect, the electric signal detected is then associated to capacitance variation, due to the air gap reduction in the material. On the other hand, it is possible to observe the presence of two peaks in the waveform that can be associated both to the piezoelectric and to the electret effects.

Chapter 8
Conclusions

Elecrospun polymers have been deeply investigated in order to realize innovative components for energy storage, energy harvesting and sensors. Unless this technique has been widely studied in literature for different purposes, many improvements are still needed to increase electrospun material performances.

In particular, separators have been currently accepted as promising candidates for next generation LIBs. However, literature papers have not showed the strong limitation of these materials yet. Indeed, mechanical behavior of electrospun separators have been carefully considered in this work, in order to achieve material stress-at-break able to sustain industrial machinery operations. Without this precaution the use of electrospun separators for LIBs is limited to the research field. Two different techniques have been carried out for this purpose, showing the effectiveness of both cross-electrospun nanofibers and nanofilled electrospun nanofibers. This achievement highlighted the possibility to scale up the electrospinning manufacturing technique. In particular, the use of Nylon 6,6 in cross-electrospun separators increased mechanical properties of PVdF, showing a feasible method to avoid the use of any toxic nanoadditive. On the other hand, nanofilled separators showed good mechanical and chemical properties although silica and

tin oxides are made of conventionally active components for LIB electrodes. Furthermore, nanofilled materials showed better behavior against short-circuit compared with pristine separator. Moreover, no evidence of any electroactive activity was found due to the presence of such additives. Electrochemical performance of electrospun separators was compared with commercial materials, showing promising results. Plasma assisted electrolyte uptake improvement of these separators was also studied and this technique could represent a novel method to further increase LIB electrochemical behavior in terms of ionic conductivity. It is worth noting that the very low internal resistance of LIBs with electrospun separators can lead to a breakthrough in power-intensive applications.

Considering PVdF-based polymers in the polar crystalline phase, a deep study of the electrical signal generated by electrospun materials subjected to mechanical impulses has been carried out. Literature paper analysis has showed that most of reported waveforms generated by electrospun samples were associated to the piezoelectric effect. This is commonly explained thanks to the presence of the crystalline PVdF ß-phase in the material. However, ß-phase must be oriented through material electrical poling in order to obtain a piezoelectric polymer. So far, in literature is claimed that poling during electrospinning is achieved due to the presence of a high electric field between the needle and the grounded electrode. Nevertheless, waveform analysis has highlighted a more complex situation. This is related to the existence of triboelectric effect between metallic electrodes and dielectric PVdF sample. This phenomenon modifies waveform output and can not be well controlled due to its dependency by ambient conditions and surface roughness. Moreover, electrospinning provides charge accumulation in these polymers, due to their fluorine content, that shows deep charge traps. In addition to

that, porous structure of electrospun materials leads to an electret behavior that depends on material capacitance variations related to porosity decrease during mechanical impacts. Currently, it is not possible to find the evidence of piezoelectric effect in the electrical signal detected, or clearly distinguish between pure piezoelectric and electret effect. Nevertheless, the high specific electrical response to mechanical stimuli of electrospun PVdF-based materials can be successfully exploited to realize high performance energy harvesters or impact/health monitoring nanostructured sensors. Dipole polarization of electrospun fibers is currently under investigation by means of piezoresponse force microscopy. Preliminary results have shown that fibers are characterized by a negative surface potential. This can be either due to a total negative charge of the fibers or due to a dipolar structure with the dipole pointing into the surface. It is thus possible that negative trapped charge shields the positive contribution of dipoles. These findings suggest that the electret effect results dominant over the piezoelectric.

References

[1] A. F. Zobaa, *ENERGY STORAGE TECHNOLOGIES AND APPLICATIONS*. Rijeka, Croatia: Intech, 2013.

[2] L. J. H. and J.-M. T. Peter G. Bruce, Stefan A. Freunberger, "Li – O 2 and Li – S batteries with high energy storage," *Nat. Mater.*, vol. 11, no. December 2011, pp. 19–30, 2012.

[3] E. Niell and A. Erturk, *Advances in Energy Harvesting Methods*. Ney York: Springer Science, 2013.

[4] Z. M. S. Ramakrishna, K. Fujihara, W.-E. Teo, T.-C. Lim, *An introduction to Electrospinning and Nanofibers*. World Scientific Publishing Co. Pte. Ltd, 2005.

[5] V. Morozov, T. Morozova, and N. Kallenbach, "Atomic force microscopy of structures produced by electrospraying polymer solutions," *Int. J. Mass Spectrom.*, vol. 178, no. 3, pp. 143–159, 1998.

[6] A. Jaworek, "Micro- and nanoparticle production by electrospraying," *Powder Technol.*, vol. 176, no. 1, pp. 18–35, 2007.

[7] D. H. Reneker, "Method of making coiled and buckled electrospun fiber structures." Google Patents, 2014.

[8] W. Chen, Y. Liu, Y. Ma, J. Liu, and X. Liu, "Improved performance of PVdF-HFP/PI nanofiber membrane for lithium ion battery separator prepared by a bicomponent cross-electrospinning method," *Mater. Lett.*, vol. 133, pp. 67–70, 2014.

[9] A. L. Yarin and E. Zussman, "Upward needleless electrospinning of multiple nanofibers," *Polymer (Guildf).*, vol. 45, no. 9, pp. 2977–2980, 2004.

[10] L. L. Guo, Y. B. Liu, and J. B. Yao, "A Review on Existing Tecgnology of Electrospinning at Large Scale," *Proc. 2010 Int. Conf. Inf. Technol. Sci. Manag. Vols 1-2*, pp. 279–282,

2010.

[11] P. Schümmer and K. H. Tebel, “A new elongational rheometer for polymer solutions,” *J. Nonnewton. Fluid Mech.*, vol. 12, no. 3, pp. 331–347, Jan. 1983.

[12] Y. Christanti and L. M. Walker, “Surface tension driven jet break up of strain-hardening polymer solutions,” *J. Nonnewton. Fluid Mech.*, vol. 100, no. 1–3, pp. 9–26, 2001.

[13] T. Jarusuwannapoom, W. Hongrojjanawiwat, S. Jitjaicham, L. Wannatong, M. Nithitanakul, C. Pattamaprom, P. Koombhongse, R. Rangkupan, and P. Supaphol, “Effect of solvents on electro-spinnability of polystyrene solutions and morphological appearance of resulting electrospun polystyrene fibers,” *Eur. Polym. J.*, vol. 41, no. 3, pp. 409–421, 2005.

[14] L. Wannatong, A. Sirivat, and P. Supaphol, “Effects of solvents on electrospun polymeric fibers: Preliminary study on polystyrene,” *Polym. Int.*, vol. 53, no. 11, pp. 1851–1859, 2004.

[15] H. Fong, I. Chun, and D. H. Reneker, “Beaded nanofibers formed during electrospinning,” *Polymer (Guildf).*, vol. 40, no. 16, pp. 4585–4592, 1999.

[16] C. Mit-uppatham, M. Nithitanakul, and P. Supaphol, “Ultratine electrospun polyamide-6 fibers: Effect of solution conditions on morphology and average fiber diameter RID C-4353-2008,” *Macromol. Chem. Phys.*, vol. 205, no. 17, pp. 2327–2338, 2004.

[17] J. Kameoka, R. Orth, Y. Yang, D. Czaplewski, R. Mathers, G. W. Coates, and H. G. Craighead, “A scanning tip electrospinning source for deposition of oriented nanofibres,” *Nanotechnology*, vol. 14, no. 10, pp. 1124–1129, 2003.

[18] P. K. Baumgarten, “Electrostatic spinning of acrylic microfibers,” *J. Colloid Interface Sci.*, vol. 36, no. 1, pp. 71–79, 1971.

[19] S. Megelskji, J. S.Stephens, D. B. Chase, and J. F.Rabolt, "Micro-and Nanostructured Surface Morphology on Electrospum Polymer Fibers," vol. 35, no. 22, pp. 8456–8466, 2002.

[20] M. M. Demir, I. Yilgor, E. Yilgor, and B. Erman, "Electrospinning of polyurethane fibers," *Polymer (Guildf).*, vol. 43, no. 11, pp. 3303–3309, 2002.

[21] C. J. Buchko, K. M. Kozloff, and D. C. Martin, "Surface characterization of porous, biocompatible protein polymer thin films," *Biomaterials*, vol. 22, no. 11, pp. 1289–1300, 2001.

[22] J. S. Lee, K. H. Choi, H. Do Ghim, S. S. Kim, D. H. Chun, H. Y. Kim, and W. S. Lyoo, "Role of molecular weight of atactic poly(vinyl alcohol) (PVA) in the structure and properties of PVA nanofabric prepared by electrospinning," *J. Appl. Polym. Sci.*, vol. 93, no. 4, pp. 1638–1646, 2004.

[23] K. J. Pawlowski, H. L. Belvin, D. L. Raney, J. Su, J. S. Harrison, and E. J. Siochi, "Electrospinning of a micro-air vehicle wing skin," *Polymer (Guildf).*, vol. 44, no. 4, pp. 1309–1314, 2003.

[24] S. Zhao, X. Wu, L. Wang, and Y. Huang, "Electrostatically generated fibers of ethyl-cyanoethyl cellulose," *Cellulose*, vol. 10, no. 4, pp. 405–409, 2003.

[25] X. Zong, K. Kim, D. Fang, S. Ran, B. S. Hsiao, and B. Chu, "Structure and process relationship of electrospun bioabsorbable nanofiber membranes," *Polymer (Guildf).*, vol. 43, no. 16, pp. 4403–4412, 2002.

[26] S. Zhao, X. Wu, L. Wang, and Y. Huang, "Electrospinning of Ethyl – Cyanoethyl Cellulose / Tetrahydrofuran Solutions," *J. Appl. Polym. Sci.*, vol. 91, no. 1, pp. 242–246, 2003.

[27] J. M. Deitzel, J. Kleinmeyer, D. Harris, and N. . Beck Tan, "The effect of processing variables on the morphology of electrospun nanofibers and textiles," *Polymer (Guildf).*, vol. 42, no. 1, pp. 261–272, 2001.

[28] Z. Ma, M. Kotaki, R. Inai, and S. Ramakrishna, "Potential of nanofiber matrix as tissue-engineering scaffolds.," *Tissue Eng.*, vol. 11, no. 1–2, pp. 101–109, 2005.

[29] C. Burger, B. S. Hsiao, and B. Chu, "Nanofibrous Materials and Their Applications," *Annu. Rev. Mater. Res.*, vol. 36, no. 1, pp. 333–368, 2006.

[30] D. Li and Y. Xia, "Electrospinning of nanofibers: Reinventing the wheel?," *Adv. Mater.*, vol. 16, no. 14, pp. 1151–1170, 2004.

[31] N. Bhardwaj and S. C. Kundu, "Electrospinning: A fascinating fiber fabrication technique," *Biotechnol. Adv.*, vol. 28, no. 3, pp. 325–347, 2010.

[32] Y.-F. Goh, I. Shakir, and R. Hussain, "Electrospun fibers for tissue engineering, drug delivery, and wound dressing," *J. Mater. Sci.*, vol. 48, no. 8, pp. 3027–3054, 2013.

[33] C. Kriegel, A. Arrechi, K. Kit, D. J. McClements, and J. Weiss, "Fabrication, functionalization, and application of electrospun biopolymer nanofibers.," *Crit. Rev. Food Sci. Nutr.*, vol. 48, no. 8, pp. 775–797, 2008.

[34] X. Liu, T. Lin, J. Fang, G. Yao, H. Zhao, M. Dodson, and X. Wang, "In vivo wound healing and antibacterial performances of electrospun nanofibre membranes," *J. Biomed. Mater. Res. - Part A*, vol. 94, no. 2, pp. 499–508, 2010.

[35] A. Greiner and J. H. Wendorff, "Electrospinning: A fascinating method for the preparation of ultrathin fibers," *Angew. Chemie - Int. Ed.*, vol. 46, no. 30, pp. 5670–5703, 2007.

[36] Z. Dong, S. J. Kennedy, and Y. Wu, "Electrospinning materials for energy-related applications and devices," *J. Power Sources*, vol. 196, no. 11, pp. 4886–4904, 2011.

[37] J. Chang, M. Dommer, C. Chang, and L. Lin, "Piezoelectric nanofibers for energy scavenging

applications," *Nano Energy*, vol. 1, no. 3, pp. 356–371, 2012.

[38] W. A. van Schalkwijk and B. Scrosati, *Advances in Lithium-Ion Batteries*. New York: KLUWER ACADEMIC PUBLISHERS, 2002.

[39] M. Winter, J. O. Besenhard, M. E. Spahr, and P. Novák, "Insertion Electrode Materials for Rechargeable Lithium Batteries," *Adv. Mater.*, vol. 10, no. 10, pp. 725–763, 1998.

[40] D. W. Murphy, J. Broadhead, and B. C. H. Steele, Eds., *Materials for Advanced Batteries*. Boston, MA: Springer US, 1980.

[41] F. Orsini, a Du Pasquier, B. Beaudoin, J. . Tarascon, M. Trentin, N. Langenhuizen, E. De Beer, and P. Notten, "In situ Scanning Electron Microscopy (SEM) observation of interfaces within plastic lithium batteries," *J. Power Sources*, vol. 76, no. 1, pp. 19–29, 1998.

[42] W. Xu, J. Wang, F. Ding, X. Chen, E. Nasybulin, Y. Zhang, and J.-G. Zhang, "Lithium metal anodes for rechargeable batteries," *Energy Environ. Sci.*, vol. 7, p. 513, 2014.

[43] T. Osaka and T. Momma, "Lithium metal/polymer battery," *J. Power Sources*, vol. 97–98, no. June 2000, pp. 765–767, 2001.

[44] D. Guyomard and J.-M. Tarascon, "Rocking-chair or lithium-ion rechargeable lithium batteries," *Adv. Mater.*, vol. 6, no. 5, pp. 408–412, 1994.

[45] B. Scrosati and J. Garche, "Lithium batteries: Status, prospects and future," *J. Power Sources*, vol. 195, no. 9, pp. 2419–2430, 2010.

[46] C. Glaize and S. Genies, *Lithium Batteries and Other Electrochemical Storage Systems*. 2013.

[47] R. Marom, S. F. Amalraj, N. Leifer, D. Jacob, and D. Aurbach, "A review of advanced and practical lithium battery materials," *J. Mater. Chem.*, vol. 21, no. 27, p. 9938, 2011.

[48] G. Pistoia, *Lithium-ion Batteries: Advances and Applications*. 2013.

[49] X. Huang, "Separator technologies for lithium-ion batteries," *J. Solid State Electrochem.*, vol. 15, no. 4, pp. 649–662, 2011.

[50] S. S. Zhang, "A review on the separators of liquid electrolyte Li-ion batteries," *J. Power Sources*, vol. 164, no. 1, pp. 351–364, 2007.

[51] C. M. Costa, M. M. Silva, and S. Lanceros-Méndez, "Battery separators based on vinylidene fluoride (VDF) polymers and copolymers for lithium ion battery applications," *RSC Adv.*, vol. 3, no. 29, p. 11404, 2013.

[52] F. Liu, N. A. Hashim, Y. Liu, M. R. M. Abed, and K. Li, "Progress in the production and modification of PVDF membranes," *J. Memb. Sci.*, vol. 375, no. 1–2, pp. 1–27, 2011.

[53] Y. Lee Min, J. W. Kim, N. S. Choi, J. Lee An, W. H. Seol, and J. K. Park, "Novel porous separator based on PVdF and PE non-woven matrix for rechargeable lithium batteries," *J. Power Sources*, vol. 139, no. 1–2, pp. 235–241, 2005.

[54] T. H. Cho, M. Tanaka, H. Onishi, Y. Kondo, T. Nakamura, H. Yamazaki, S. Tanase, and T. Sakai, "Battery performances and thermal stability of polyacrylonitrile nano-fiber-based nonwoven separators for Li-ion battery," *J. Power Sources*, vol. 181, no. 1, pp. 155–160, 2008.

[55] C. Arbizzani, F. Colò, F. De Giorgio, M. Guidotti, M. Mastragostino, F. Alloin, M. Bolloli, Y. Molméret, and J. Y. Sanchez, "A non-conventional fluorinated separator in high-voltage graphite/LiNi 0.4Mn1.6O4 cells," *J. Power Sources*, vol. 246, pp. 299–304, 2014.

[56] Z. Zhong, Q. Cao, B. Jing, X. Wang, X. Li, and H. Deng, "Electrospun PVdF-PVC nanofibrous polymer electrolytes for polymer lithium-ion batteries," *Mater. Sci. Eng. B Solid-State Mater. Adv. Technol.*, vol. 177, no.

1, pp. 86–91, 2012.

[57] Y. E. Miao, G. N. Zhu, H. Hou, Y. Y. Xia, and T. Liu, "Electrospun polyimide nanofiber-based nonwoven separators for lithium-ion batteries," *Journal of Power Sources*, vol. 226. pp. 82–86, 2013.

[58] F. Croce, M. L. Focarete, J. Hassoun, I. Meschini, and B. Scrosati, "A safe, high-rate and high-energy polymer lithium-ion battery based on gelled membranes prepared by electrospinning," *Energy Environ. Sci.*, vol. 4, no. 3, p. 921, 2011.

[59] V. Aravindan, J. Sundaramurthy, P. S. Kumar, N. Shubha, W. C. Ling, S. Ramakrishna, and S. Madhavi, "A novel strategy to construct high performance lithium-ion cells using one dimensional electrospun nanofibers, electrodes and separators.," *Nanoscale*, vol. 5, no. 21, pp. 10636–45, 2013.

[60] S. Ramakrishna, K. Fujihara, W. E. Teo, T. Yong, Z. Ma, and R. Ramaseshan, "Electrospun nanofibers: Solving global issues," *Mater. Today*, vol. 9, no. 3, pp. 40–50, 2006.

[61] V. Thavasi, G. Singh, and S. Ramakrishna, "Electrospun nanofibers in energy and environmental applications," *Energy Environ. Sci.*, vol. 1, no. 2, p. 205, 2008.

[62] G. H. Kim, "Electrospun PCL nanofibers with anisotropic mechanical properties as a biomedical scaffold," *Biomed. Mater.*, vol. 3, 2008.

[63] K. H. Lee, H. A. K. Y. Kim, Y. J. U. N. Ryu, K. W. O. O. Kim, and S. U. N. W. Choi, "Mechanical Behavior of Electrospun Fiber Mats of Poly(vinyl chloride)/Polyurethane Polyblends," *J. Polym. Sci. Part B Polym. Phys.*, vol. 41, pp. 1256–1262, 2003.

[64] X. Huang and J. Hitt, "Lithium ion battery separators: Development and performance characterization of a composite membrane," *J. Memb. Sci.*, vol. 425–426, pp. 163–168, 2013.

[65] K.-U. Jeong, H. D. Chae, C. Il Lim, H. K. Lee, J.-H. Ahn, and C. Nah, "Fabrication and characterization of electrolyte membranes based on organoclay/tripropyleneglycol diacrylate/poly(vinylidene fluoride) electrospun nanofiber composites," *Polym. Int.*, vol. 59, no. 2, pp. 249–255, 2009.

[66] P. Raghavan, X. Zhao, J. K. Kim, J. Manuel, G. S. Chauhan, J. H. Ahn, and C. Nah, "Ionic conductivity and electrochemical properties of nanocomposite polymer electrolytes based on electrospun poly(vinylidene fluoride-co-hexafluoropropylene) with nano-sized ceramic fillers," *Electrochim. Acta*, vol. 54, no. 2, pp. 228–234, 2008.

[67] Y. J. Kim, C. H. Ahn, M. B. Lee, and M. S. Choi, "Characteristics of electrospun PVDF/SiO 2 composite nanofiber membranes as polymer electrolyte," *Mater. Chem. Phys.*, vol. 127, no. 1–2, pp. 137–142, 2011.

[68] M. Zaccaria, C. Gualandi, D. Fabiani, M. L. Focarete, and F. Croce, "Effect of oxide nanoparticles on thermal and mechanical properties of electrospun separators for lithium-ion batteries," *J. Nanomater.*, vol. 2012, 2012.

[69] J. Zhang, L. Yue, Q. Kong, Z. Liu, X. Zhou, C. Zhang, S. Pang, X. Wang, J. Yao, and G. Cui, "A Heat-Resistant Silica Nanoparticle Enhanced Polysulfonamide Nonwoven Separator for High-Performance Lithium Ion Battery," *J. Electrochem. Soc.*, vol. 160, no. 6, pp. A769–A774, 2013.

[70] J. Lee, C. L. Lee, K. Park, and I. D. Kim, "Synthesis of an Al2O3-coated polyimide nanofiber mat and its electrochemical characteristics as a separator for lithium ion batteries," *J. Power Sources*, vol. 248, pp. 1211–1217, 2014.

[71] Y. Liang, L. Ji, B. Guo, Z. Lin, Y. Yao, Y. Li, M. Alcoutlabi, Y. Qiu, and X. Zhang, "Preparation and electrochemical characterization of ionic-conducting lithium lanthanum titanate oxide/polyacrylonitrile submicron composite fiber-based lithium-ion battery separators," *J. Power*

Sources, vol. 196, no. 1, pp. 436–441, 2011.

[72] H.-R. Jung, D.-H. Ju, W.-J. Lee, X. Zhang, and R. Kotek, "Electrospun hydrophilic fumed silica/polyacrylonitrile nanofiber-based composite electrolyte membranes," *Electrochim. Acta*, vol. 54, no. 13, pp. 3630–3637, 2009.

[73] M. Yanilmaz, Y. Lu, M. Dirican, K. Fu, and X. Zhang, "Nanoparticle-on-nanofiber hybrid membrane separators for lithium-ion batteries via combining electrospraying and electrospinning techniques," *J. Memb. Sci.*, vol. 456, pp. 57–65, 2014.

[74] M. Yanilmaz, C. Chen, and X. Zhang, "Fabrication and characterization of SiO2/PVDF composite nanofiber-coated PP nonwoven separators for lithium-ion batteries," *J. Polym. Sci. Part B Polym. Phys.*, vol. 51, no. 23, pp. 1719–1726, 2013.

[75] D. Fabiani, M. Zaccaria, M. L. Focarete, C. Gualandi, V. Colombo, E. Ghedini, M. Gherardi, R. Laurita, and P. Sanibondi, "Plasma assisted nanoparticle dispersion in polymeric solutions for the production of electrospun lithium battery separators," *Proc. IEEE Int. Conf. Solid Dielectr. ICSD*, pp. 718–721, 2013.

[76] V. Colombo, D. Fabiani, M. L. Focarete, M. Gherardi, C. Gualandi, R. Laurita, and M. Zaccaria, "Method for producing, from a polymer matrix in a liquid phase, a solid material containing nano-additives." Google Patents, 2014.

[77] R. A. Wolf, *Atmospheric Pressure Plasma for surface modification (R.A. Wolf)*. Beverly, MA: Scrivener Publishing, 2013.

[78] G. F. Alexander Fridman, *Plasma medicine*, vol. 43, no. 3. John Wiley & Sons, Ltd, 2013.

[79] V. Colombo, D. Fabiani, M. L. Focarete, M. Gherardi, C. Gualandi, R. Laurita, and M. Zaccaria, "Atmospheric Pressure Non-Equilibrium Plasma Treatment to Improve the Electrospinnability of Poly(L -Lactic Acid) Polymeric Solution," *Plasma Process. Polym.*, vol. 11, no. 3, pp. 247–

255, 2014.

[80] Q. Shi, N. Vitchuli, J. Nowak, Z. Lin, B. Guo, M. McCord, M. Bourham, and X. Zhang, "Atmospheric plasma treatment of pre-electrospinning polymer solution: A feasible method to improve electrospinnability," *J. Polym. Sci. Part B Polym. Phys.*, vol. 49, no. 2, pp. 115–122, 2011.

[81] G. T. D. M. G. Broadhurst, R. G.-M. B. Gross, S. Mascarenhas, and J. E. W. G.M. Sessler, J. van Turnhout, *Electrets*. Springer-Verlag, 1987.

[82] M. S. Vijaya, *Piezoelectric Materials and Devices*. Boca Raton: CRC Press Taylor & Francis Group, 2013.

[83] X. Qiu, A. Mellinger, W. Wirges, and R. Gerhard, "Spectroscopic study of dielectric barrier discharges in cellular polypropylene ferroelectrets," *Appl. Phys. Lett.*, vol. 91, no. 13, p. 132905, 2007.

[84] E. Nilsson, A. Lund, C. Jonasson, C. Johansson, and B. Hagström, "Poling and characterization of piezoelectric polymer fibers for use in textile sensors," *Sensors Actuators, A Phys.*, vol. 201, pp. 477–486, 2013.

[85] P. Martins, a. C. Lopes, and S. Lanceros-Mendez, "Electroactive phases of poly(vinylidene fluoride): Determination, processing and applications," *Prog. Polym. Sci.*, vol. 39, no. 4, pp. 683–706, 2014.

[86] Andrew J . Lovinger, "Ferroelectric Polymers," *Science*, vol. 220, no. 4602, pp. 1115–1121, 2014.

[87] J. Gomes, J. Serrado Nunes, V. Sencadas, and S. Lanceros-Mendez, "Influence of the ß-phase content and degree of crystallinity on the piezo- and ferroelectric properties of poly(vinylidene fluoride)," *Smart Mater. Struct.*, vol. 19, no. 6, p. 065010, 2010.

[88] V. Sencadas, R. Gregorio, and S. Lanceros-Mendez, "α to ß Phase Transformation and Microestructural Changes of PVDF Films Induced by Uniaxial Stretch," *J. Macromol. Sci. Part B*, vol. 48, no. 3, pp. 514–525, 2009.

[89] T. Hattori, M. Kanaoka, and H. Ohigashi, “Improved Piezoelectricity in Thick Lamellar Beta-Form Crystals of Poly(Vinylidene Fluoride) Crystallized Under High Pressure,” *J. Appl. Phys.*, vol. 79, no. 4, pp. 2016–2022, 1996.

[90] C. Ribeiro, V. Sencadas, J. L. G. Ribelles, and S. Lanceros-Méndez, “Influence of Processing Conditions on Polymorphism and Nanofiber Morphology of Electroactive Poly(vinylidene fluoride) Electrospun Membranes,” *Soft Mater.*, vol. 8, no. 3, pp. 274–287, 2010.

[91] D. Yang and Y. Chen, “B-Phase Formation of Poly(Vinylidene Fluoride) From the Melt Induced By Quenching,” *J. Mater. Sci. Lett.*, vol. 6, no. 5, pp. 599–603, 1987.

[92] A. Ferreira, P. Costa, H. Carvalho, J. M. Nobrega, V. Sencadas, and S. Lanceros-Mendez, “Extrusion of poly(vinylidene fluoride) filaments: Effect of the processing conditions and conductive inner core on the electroactive phase content and mechanical properties,” *J. Polym. Res.*, vol. 18, no. 6, pp. 1653–1658, 2011.

[93] H.-J. Ye, W.-Z. Shao, and L. Zhen, “Crystallization kinetics and phase transformation of poly(vinylidene fluoride) films incorporated with functionalized baTiO 3 nanoparticles,” *J. Appl. Polym. Sci.*, vol. 129, no. 5, pp. 2940–2949, 2013.

[94] E. Fukada, “History and Recent Progress in Piezoelectric Polymers,” *IEEE Trans. Ultrason. Ferroelectr. Freq. Control*, vol. 47, no. 6, pp. 1277–1290, 2000.

[95] A. J. Lovinger, T. Furukawa, G. T. Davis, and M. G. Broadhurst, “Crystallographic changes characterizing the Curie transition in three ferroelectric copolymers of vinylidene fluoride and trifluoroethylene: 2. Oriented or poled samples,” *Polymer (Guildf).*, vol. 24, no. 10, pp. 1233–1239, Oct. 1983.

[96] F. Guan, J. Wang, L. Zhu, J. Pan, and Q. Wang, “Effects of film processing conditions on electric energy storage for

pulsed power applications," *IEEE Trans. Dielectr. Electr. Insul.*, vol. 18, no. 4, pp. 1293–1300, 2011.

[97] B. Mohammadi, A. A. Yousefi, and S. M. Bellah, "Effect of tensile strain rate and elongation on crystalline structure and piezoelectric properties of PVDF thin films," *Polym. Test.*, vol. 26, no. 1, pp. 42–50, 2007.

[98] J. Pu, X. Yan, Y. Jiang, C. Chang, and L. Lin, "Piezoelectric actuation of direct-write electrospun fibers," *Sensors Actuators, A Phys.*, vol. 164, no. 1–2, pp. 131–136, 2010.

[99] D. Mandal, S. Yoon, and K. J. Kim, "Origin of Piezoelectricity in an Electrospun Poly(vinylidene fluoride-trifluoroethylene) Nanofiber Web-Based Nanogenerator and Nano-Pressure Sensor," *Macromol. Rapid Commun.*, vol. 32, no. 11, pp. 831–837, 2011.

[100] L. Persano, C. Dagdeviren, Y. Su, Y. Zhang, S. Girardo, D. Pisignano, Y. Huang, and J. a Rogers, "High performance piezoelectric devices based on aligned arrays of nanofibers of poly(vinylidenefluoride-co-trifluoroethylene).," *Nat. Commun.*, vol. 4, p. 1633, 2013.

[101] C. Chang, V. H. Tran, J. Wang, Y. K. Fuh, and L. Lin, "Direct-write piezoelectric polymeric nanogenerator with high energy conversion efficiency," *Nano Lett.*, vol. 10, no. 2, pp. 726–731, 2010.

[102] D. Fabiani, M. Zaccaria, J. Belcari, and A. Zucchelli, "Electrospun Nanofibers with Piezoelectric Properties," in *33th IEEE Electrical Insulation Conference*, 2015, pp. 7–10.

[103] H. F. Guo, Z. S. Li, S. W. Dong, W. J. Chen, L. Deng, Y. F. Wang, and D. J. Ying, "Piezoelectric PU/PVDF electrospun scaffolds for wound healing applications," *Colloids Surfaces B Biointerfaces*, vol. 96, pp. 29–36, 2012.

[104] Y. S. Lee, G. Collins, and T. Livingston Arinzeh, "Neurite extension of primary neurons on electrospun piezoelectric scaffolds," *Acta Biomater.*, vol. 7, no. 11, pp. 3877–3886,

2011.

[105] J. Morvan, E. Buyuktanir, J. L. West, and a. Jákli, "Highly piezoelectric biocompatible and soft composite fibers," *Appl. Phys. Lett.*, vol. 100, no. 6, 2012.

[106] G. Collins, J. Federici, Y. Imura, and L. H. Catalani, "Charge generation, charge transport, and residual charge in the electrospinning of polymers: A review of issues and complications," *J. Appl. Phys.*, vol. 111, no. 2012, pp. 1–19, 2012.

[107] B. M. Cho, Y. S. Nam, J. Y. Cheon, and W. H. Park, "Residual charge and filtration efficiency of polycarbonate fibrous membranes prepared by electrospinning," *J. Appl. Polym. Sci.*, vol. 132, no. 1, p. n/a–n/a, 2015.

[108] H. Canbolat, Ed., *Electrostatics*. InTech, 2012.

[109] Z. L. Wang, G. Zhu, Y. Yang, S. Wang, and C. Pan, "Progress in nanogenerators for portable electronics," *Mater. Today*, vol. 15, no. 12, pp. 532–543, 2012.

[110] a. F. Diaz and R. M. Felix-Navarro, "A semi-quantitative tribo-electric series for polymeric materials: The influence of chemical structure and properties," *J. Electrostat.*, vol. 62, no. 4, pp. 277–290, 2004.

[111] H. E. C. John Hans Dessauer, *Xerography and Related Processes*. Focal Press, 1965.

[112] X. Chen, M. Iwamoto, Z. Shi, L. Zhang, and Z. L. Wang, "Self-Powered Trace Memorization by Conjunction of Contact-Electrification and Ferroelectricity," *Adv. Funct. Mater.*, vol. 25, no. 5, pp. 739–747, 2015.

[113] Y. Zheng, L. Cheng, M. Yuan, Z. Wang, L. Zhang, Y. Qin, and T. Jing, "An electrospun nanowire-based triboelectric nanogenerator and its application in a fully self-powered UV detector.," *Nanoscale*, vol. 6, no. 14, pp. 7842–6, 2014.

[114] T. Huang, C. Wang, H. Yu, H. Wang, Q. Zhang, and M. Zhu, "Human walking-driven wearable all-fiber triboelectric nanogenerator containing electrospun

polyvinylidene fluoride piezoelectric nanofibers," *Nano Energy*, vol. 14, pp. 226–235, 2015.

[115] V. Colombo, E. Ghedini, M. Gherardi, R. Laurita, P. Sanibondi, D. Fabiani, M. Zaccaria, M. L. Focarete, and C. Gualandi, "Study of the effect of atmospheric pressure plasma treatment on electrospinnability of poly-L-lactic acid solutions: Voltage waveform effect," in *2013 IEEE International Conference on Solid Dielectrics (ICSD)*, 2013, pp. 358–361.

[116] F. Yang, R. Murugan, S. Wang, and S. Ramakrishna, "Electrospinning of nano/micro scale poly(l-lactic acid) aligned fibers and their potential in neural tissue engineering," *Biomaterials*, vol. 26, no. 15, pp. 2603–2610, 2005.

[117] S. H. Tan, R. Inai, M. Kotaki, and S. Ramakrishna, "Systematic parameter study for ultra-fine fiber fabrication via electrospinning process," *Polymer (Guildf).*, vol. 46, no. 16, pp. 6128–6134, 2005.

[118] Z.-M. Huang, Y. . Zhang, S. Ramakrishna, and C. . Lim, "Electrospinning and mechanical characterization of gelatin nanofibers," *Polymer (Guildf).*, vol. 45, no. 15, pp. 5361–5368, Jul. 2004.

[119] a. K. Haghi, *Electrospinning of Nanofibers in Textiles*. 2012.

[120] Y. J. Ryu, H. Y. Kim, K. H. Lee, H. C. Park, and D. R. Lee, "Transport properties of electrospun nylon 6 nonwoven mats," *Eur. Polym. J.*, vol. 39, no. 9, pp. 1883–1889, 2003.

[121] L. S. Dolci, S. D. Quiroga, M. Gherardi, R. Laurita, A. Liguori, P. Sanibondi, A. Fiorani, L. Calzà, V. Colombo, and M. L. Focarete, "Carboxyl surface functionalization of poly(L -lactic acid) electrospun nanofibers through atmospheric non-thermal plasma affects fibroblast morphology," *Plasma Process. Polym.*, vol. 11, no. 3, pp. 203–213, 2014.

[122] H. Hantsche, *High resolution XPS of organic polymers,*

the scienta ESCA300 database. By G. Beamson and D. Briggs. Chichester: Wiley, 1992.

[123] D. M. Correia, C. Ribeiro, V. Sencadas, G. Botelho, S. A. C. Carabineiro, J. L. G. Ribelles, and S. Lanceros-Méndez, "Influence of oxygen plasma treatment parameters on poly(vinylidene fluoride) electrospun fiber mats wettability," *Prog. Org. Coatings*, vol. 85, pp. 151–158, 2015.

[124] Y. W. Park and N. Inagaki, "Surface modification of poly (vinylidene fluoride) film by remote Ar , H 2 , and O 2 plasmas," *Polymer (Guildf).*, vol. 44, pp. 1569–1575, 2003.

[125] M. Boselli, V. Colombo, M. Gherardi, R. Laurita, A. Liguori, P. Sanibondi, E. Simoncelli, and A. Stancampiano, "Characterization of a Cold Atmospheric Pressure Plasma Jet Device Driven by Nanosecond Voltage Pulses," *IEEE Trans. PLASMA Sci.*, vol. 43, no. 3, pp. 713–725, 2015.

[126] H. S. Nalwa, *Ferroelectric polymers, chemistry, physics, and applications*, vol. XXXIII, no. 2. New York: Marcel Dekker, Inc., 1995.

[127] D. Fabiani, M. Zaccaria, A. Zucchelli, J. Belcari, and O. Bocchi, "Electrospun Nanofibers with Piezoelectric Properties," in *IEEE Electrical Insulation Conference (EIC)*, 2015.

[128] M. Zaccaria, D. Fabiani, A. Zucchelli, J. Belcari, and O. Bocchi, "Electrospun PVdF with Enhanced Piezoelectric Behavior," in *IEEE 11th International Conference on the Properties and Applications of Dielectric Materials (ICPADM)*, 2015, pp. 136–139.

[129] L. a. Dissado, G. C. Montanari, and D. Fabiani, "Fast soliton-like charge pulses in insulating polymers," *J. Appl. Phys.*, vol. 109, no. 6, p. 064104, 2011.

[130] M. Rao, X. Geng, Y. Liao, S. Hu, and W. Li, "Preparation and performance of gel polymer electrolyte based on electrospun polymer membrane and ionic liquid for lithium ion battery," *J. Memb. Sci.*, vol. 399–400, pp. 37–

42, 2012.

[131] H. Wang, T. Wang, S. Yang, and L. Fan, “Preparation of thermal stable porous polyimide membranes by phase inversion process for lithium-ion battery,” *Polym. (United Kingdom)*, vol. 54, no. 23, pp. 6339–6348, 2013.

[132] S. Boisseau, G. Despesse, and B. A. Seddik, “Electrostatic Conversion for Vibration Energy Harvesting, Small-Scale Energy Harvesting,” Intech, 2012, pp. 1–39.

List of published papers

Journal papers:

1. R. Laurita, M. Zaccaria, M. Gherardi, D. Fabiani, M. L. Focarete, V. Colombo, "Plasma processing of electrospun Li-ion battery separators to improve electrolyte uptake", Plasma Processes and Polymers 13, 1, 124-133, 2016.
2. M. Zaccaria, D. Fabiani, G. Cannucciari, C. Gualandi, M. L. Focarete, C. Arbizzani, F. De Giorgio and M. Mastragostino, "Effect of Silica and Tin Oxide Nanoparticles on Properties of Nanofibrous Electrospun Separators", Journal of The Electrochemical Society 162 (6) A915-A920 (2015).
3. V. Colombo, D. Fabiani, M. L. Focarete, M. Gherardi, C. Gualandi, R. Laurita, M. Zaccaria, "Atmospheric pressure non-equilibrium plasma treatment to improve the electrospinnability of poly(L-lactic acid) polymeric solution", Plasma Processes and Polymers 11, 247–255, 2014.
4. M. Zaccaria, C. Gualandi, D. Fabiani, M. L. Focarete and F. Croce, "Effect of Oxide Nanoparticles on Thermal and Mechanical Properties of Electrospun Separators for Lithium-Ion Batteries", Journal of Nanomaterials Volume 2012 (2012), Article ID 216012, 8 pages.

Regular Conference papers:

5. M. Zaccaria, D. Fabiani, A. Zucchelli, J. Belcari and O. Bocchi, "Electrospun PVdF with Enhanced Piezoelectric Behavior", Proceedings of the 11th IEEE International Conference on the Properties and Applications of Dielectric Materials, Sydney, Australia, 19-22 July 2015.
6. D. Fabiani, M. Zaccaria, A. Zucchelli, J. Belcari and O. Bocchi, "Electrospun nanofibers with piezoelectric

properties", Proceedings of the 33rd IEEE Electrical Insulation Conference, Seattle, USA, 07-10 June 2015.
7. M. Zaccaria, D. Fabiani, A. Zucchelli, J. Belcari, "Electrospinning: a versatile technique for energy storage and sensor applications", proceedings of AEIT Annual Conference - From Research to Industry: The Need for a More Effective Technology Transfer (AEIT), Trieste, Italy, 18-19 September 2014.
8. D. Fabiani, M. Zaccaria, M. L. Focarete, C. Gualandi, V. Colombo, E. Ghedini, M. Gherardi, R. Laurita, P. Sanibondi, "Plasma assisted nanoparticle dispersion in polymeric solutions for the production of electrospun lithium battery separators", proceedings of the 11th IEEE International Conference on Solid Dielectrics, Bologna, Italy, 30 June - 4 July 2013.
9. V. Colombo, E. Ghedini, M. Gherardi, R. Laurita, P. Sanibondi, D. Fabiani, M. Zaccaria, M. L. Focarete, C. Gualandi, "Study of the effect of atmospheric pressure plasma treatment on electrospinnability of poly-L-lactic acid solutions: voltage waveform effect", proceedings of the 11th IEEE International Conference on Solid Dielectrics, Bologna, Italy, 30 June - 4 July 2013.

Conference abstracts:

10. C. Arbizzani, G. Cannucciari, F. De Giorgio, D. Fabiani, M. L. Focarete, M. Mastragostino, M. Zaccaria, "Comparison between Poly(vinylidene fluoride) (PVdF) electrospun and conventional separators for Li-ion batteries", proceedings of the 15th IEEE International Symposium on Electrets, Baltimore, USA, 11-13 August, 2014.
11. J. Belcari, D. Fabiani, M. Zaccaria, A. Zucchelli, "Realization of smart composite materials using electrospun Poly vinylidene fluoride (PVdF) nanofibers",

proceedings of the 15th IEEE International Symposium on Electrets, Baltimore, USA, 11-13 August, 2014.
12. L. Calzà, V. Colombo, A. Fiorani, D. Fabiani, M. Focarete, M. Gherardi, C. Gualandi, R. Laurita, A. Liguori, P. Sanibondi, M. Zaccaria, "Plasma-assisted electrospinning: the many facets of a process", proceedings of the 3rd International Conference on Electrospinning, San Francisco, USA, 4-7 August 2014.
13. V. Colombo, D. Fabiani, M. Focarete, C. Gualandi, M. Gherardi, R. Laurita, M. Zaccaria, "Nanoparticle dispersion in PEO polymeric solutions via plasma treatment for the production of electrospun lithium batteries separator", proceedings of the 3rd International Conference on Electrospinning, San Francisco, USA, 4-7 August 2014.
14. M. Zaccaria, G. Cannucciari, D. Fabiani, C. Gualandi, M. L. Focarete, "Study of the effect of silica and tin oxide nanoparticles on electrospun separator properties", proceedings of the 3rd International Conference on Electrospinning, San Francisco, USA, 4-7 August 2014.
15. J. Belcari, A. Celli, D. Fabiani, M. L. Focarete, M. Gazzano, C. Gualandi, G. Pasini, L. Sisti, M. Zaccaria, A. Zucchelli, "Piezoelectric behaviour of Poly(vinylidene fluoride) electrospun mat", proceedings of the 3rd International Conference on Electrospinning, San Francisco, USA, 4-7 August 2014.
16. M. Zaccaria, G. Cannucciari, D. Fabiani, C. Gualandi, M. L. Focarete, "Effect of silica and tin oxide nanoparticles on properties of nanofibrous electrospun separators", proceedings of the 17th International Meeting on Lithium Batteries, Como, Italy, 10-14 June 2014.
17. V. Colombo, D. Fabiani, M.L. Focarete, M. Gherardi, C. Gualandi, R. Laurita, L. Paschini, M. Zaccaria, "Plasma assisted electrolyte uptake improvement for lithium batteries electrospun separators", proceedings of the 6th

International Conference on Polymer Batteries and Fuel Cells, Ulm, Germany, 3 - 7 June 2013.

18. V. Colombo, M. Gherardi, R. Laurita, D. Fabiani, M. Zaccaria, M.L. Focarete, C. Gualandi, "Effect of Plasma Assisted Nanoparticle Dispersion on Thermal and Mechanical Properties of Electrospun Separators for Lithium-ion Batteries", proceedings of the 6th Forum on New Materials, Montecatini Terme, Italy, 15-19 June 2014.
19. V. Colombo, D. Fabiani, M. L. Focarete, E. Ghedini, M. Gherardi, C. Gualandi, R. Laurita, P. Sanibondi, M. Zaccaria, "Effect of atmospheric pressure non-equilibrium plasma treatment on poly-l-lactic acid electrospinnability: investigating the roles of plasma source and voltage waveform", proceedings of IEEE Pulsed Power and Plasma Science Conference 2013, San Francisco, USA, 16-21 June 2013.
20. V. Colombo, D. Fabiani, M.L. Focarete, E. Ghedini, M. Gherardi, C. Gualandi, R. Laurita, P. Sanibondi, M. Zaccaria, "Effect of atmospheric pressure non-equilibrium plasma treatment on poly-L-lactic acid electrospinnability", proceedings of International Symposium on Plasma Chemistry 21, Cairns, Australia, 4-9 August 2013.
21. M. Alessandri, L. Calzà, V. Colombo, L. S. Dolci, A. Fiorani, D. Fabiani, M.L. Focarete, E. Ghedini, M. Gherardi, C. Gualandi, R. Laurita, A. Liguori, S. D. Quiroga, P. Sanibondi, M. Zaccaria, "Plasma-assisted electrospinning: the many facets of a process", proceedings of International Symposium on Plasma Chemistry 21, Cairns, Australia, 4-9 August 2013.
22. V. Colombo, D. Fabiani, M.L. Focarete, E. Ghedini, M. Gherardi, C. Gualandi, R. Laurita, P. Sanibondi, M. Zaccaria, "Study of the effect of atmospheric pressure plasma treatment on electrospinnability of poly-L-lactic

acid solutions: voltage waveform effect", proceedings of International Symposium on Plasma Chemistry 21, Cairns, Australia, 4-9 August 2013.
23. V. Colombo, D. Fabiani, M.L. Focarete, E. Ghedini, M. Gherardi, C. Gualandi, R. Laurita, P. Sanibondi, M. Zaccaria, "Effect of atmospheric pressure non-equilibrium plasma treatment on poly-L-lactic acid electrospinnability", proceedings of Nanotechitaly 2012, Venice, Italy, 21-23 November 2012.

Acknowledgments

"Una vita senza ricerca
non è degna di essere vissuta"
Apologia, 38A

Così come inizia questa tesi, così si conclude: il motto conosci te stesso credo che ben rappresenti l'idea di come in fondo bisogni scoprire i propri limiti, più che oltrepassare quelli della materia che stiamo studiando. Questo viaggio quindi credo sia stato più che altro una ricerca di me stesso, attraverso la conoscenza delle persone che ho incontrato lungo la strada.

Se posso dire di aver imparato a lavorare lo devo sicuramente a Romolo, che oltre ad essere un grande amico è stato capace di mostrarmi cosa significhi dedicarsi con passione e dedizione ad un'idea. E forse ancora più importante il metodo: le cose o si fanno bene o non si fanno. E non sono stati certo i mille insuccessi a fermarlo…Con lui si sta sempre sulle montagne russe dell'euforia! Il dottorato e la ricerca portano però talmente tanti insuccessi che poi rischi davvero di non essere più in grado di apprezzare le scoperte o le piccole soddisfazioni che ottieni. Gli auguro di non perdere mai la forza con cui affronta ogni giorno quel laboratorio. Se chi di dovere capisse quanto è bravo…

Qualcuno poi è stato più fortunato di altri: una volta si facevano le notti con la Focarete, a me invece sono toccate quelle con Andrea e Juri…Non credevo di poter sopravvivere a mesi di folli progetti al lazzaretto fino all'1 di notte. Ma si sa, Andrea ti trasmette una passione impareggiabile e crede davvero in quello che fa; Juri con quella determinazione potrebbe conquistare il mondo. Forse il mondo non lo avremo rivoluzionato, ma abbiamo cementato delle amicizie a cui tengo tantissimo.

Vorrei anche ringraziare Davide per avermi dato l'opportunità di crescere. Non sapevo fare nulla, ma nonostante tutto dal primo giorno ha creduto in me e mi ha voluto responsabilizzare. Non mi ha mai fatto mancare niente, mi ha lasciato sempre libero e mi ha spedito dall'altra parte del mondo confidando che non facessi disastri :)

Come non ricordare Luca, che mi ha aperto gli occhi su tante cose...e con cui ho parlato di donne 365 giorni l'anno ascoltando musica mistica, e Carlos (ancora piango pensando al giorno in cui ci siamo salutati). Quella coppia sarebbe dovuta essere il punto di riferimento di questo laboratorio…Ma le teste capaci ovviamente passano e l'Università non le coltiva. A proposito di ufficio, Paolo e Fabrizio sono stati dei grandi compagni di sventura :) Grazie per quello che mi avete insegnato; vi auguro di trovare un mondo migliore! D'altronde non si può morire né di olio né di burocrazia. Forse è proprio il mondo migliore che sta aspettando Fabio per il piccolo Ciani :) Nell'attesa grazie di cuore dell'aiuto, tu sai sempre, sempre tutto!!

Credo sia doveroso tenere per ultimo Oliviero. Senza di lui non sarei mai arrivato a scoprire e scrivere tutto questo. E' veramente un ragazzo con una testa fuori dal comune, con intuizioni geniali. Ringrazio davvero di aver avuto il piacere di confrontarmi ogni giorno con lui e ovviamente di condividere la nostra amicizia. Se si facesse ricerca in team si farebbero passi da gigante: senza il confronto di opinioni non si scopre nulla.